A Search For The $Z \rightarrow b\overline{b}$ Process at The D-Zero Experiment

Amber Helen Jenkins

Imperial College London

A thesis submitted for the degree of
Doctor of Philosophy
of the University of London
and the Diploma of Imperial College

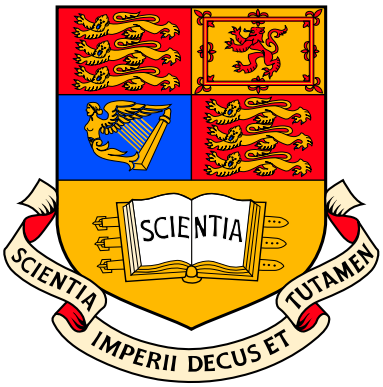

"Research is to see what everybody else has seen and to think what nobody else has thought."

Albert von Szent-Győrgyi

A Search For The $Z \rightarrow b\overline{b}$ Process at The D-Zero Experiment

Amber Jenkins
Imperial College London

November 2006

ABSTRACT

In 2001, the DØ experiment entered a new era. Run II of the Tevatron at the Fermi National Accelerator Laboratory began, and the collider became the highest energy particle accelerator in the world. Accordingly, the DØ detector had already undergone a series of upgrades in order to fully exploit the physics now within reach. These included improvements to the tracking, calorimetry, muon detection and triggering capabilities.

In the Standard Model, the Higgs boson is the last piece of the puzzle that remains to be discovered. The Higgs mechanism and consequently the Higgs boson is thought to be the fundamental ingredient by which particles acquire mass, and its existence (or lack of existence) is one of the most pressing issues in particle physics today. As such, one of the main goals of the Run II physics programme at DØ is to search for it. Armed with new accelerator capabilites, DØ will be able to impose tighter constraints on the mass of the Higgs, and perhaps even detect this elusive particle.

If the Higgs does exist, it will be extremely difficult to find. One of the main challenges at a hadron-hadron collider is to reduce the large QCD background that masks the relatively tiny Higgs signal. Experimental evidence indicates that the Higgs mass is relatively low, in which case it will decay predominantly to a $b\overline{b}$ quark-antiquark pair. The daughter products that must be used to reconstruct the parent Higgs are therefore likely to be heavy flavour b-quark jets whose energies must be known as accurately as possible.

In the first part of this thesis consideration is given to these jets, in particular to the jet energy resolution and dijet mass resolution that they could offer. One way of investigating the necessary tools for such a Higgs search is to study a very similar decay to that of a low-mass Higgs particle: a Z boson decaying to a b quark and an anti-b-quark. This signal, not previously observed at the Tevatron, offers an ideal testbed in which to explore suitable triggering and analysis techniques. It also offers us the opportunity to further our understanding of b-quark jets in a hadronic environment, an element crucial to much of the physics at DØ.

To this end, the first search has been performed at DØ for the $Z \rightarrow b\overline{b}$ decay, using the initial 300 pb^{-1} of data from Run II. Triggers have been specifically designed and implemented for this purpose. Here we present evidence for $Z \rightarrow b\overline{b}$ decays. An excess of 1260 $\pm$ 130 (stat.) $\pm$ 260 (syst.) events is observed, which is in good agreement with Monte Carlo predictions and amounts to a $Z \rightarrow b\overline{b}$ signal of 4.3 standard deviations.

Acknowledgements

"Home is not where you live but where they understand you."

Christian Morgenstern

When I first set out on this venture, I stumbled upon a promising little book called "How to get a PhD" [1]. I eagerly thumbed the pages, hoping to discover its pearls of wisdom. Yet despite being a valuable little tome, it never quite prepared me for what was to come. You see, a Ph.D. is an adventure. You get lost. You find your way. You narrowly avoid pitfalls. You climb mountains, and reach false summits. You get sunburned, you get homesick, you have the time of your life. You lose yourself, you find yourself. And when you reach the end you realise you've come quite a long way. But you couldn't have predicted where you'd end up.

As I move on I take away many fond memories, and the thing I am most grateful for is the wonderful collection of people I met along the way. First and foremost I want to thank my supervisor, Gavin Davies, for all his help and support. Gav, you've been wonderful and the sort of mentor a student could only wish for. Many of us feel genuinely lucky to be able to work with you. You have taught me many things. Thank you.

A huge thanks must also go to my colleague Per Jonsson, for being such a pleasure to work with. In the midst of the collaboration hubbub your calm, humble and friendly manner proved to be a blessing on many occasions, and your guidance invaluable. I simply couldn't have asked for a nicer colleague. Good luck in your future quests, with Michelle and the girls by your side.

I would like to thank Anna Goussiou for her supervision and friendship during the initial stages of my Ph.D. And a big thank you to John Hassard and Trevor

Bacon who very kindly took on the job of reading this thesis. I'm grateful to the High Energy Physics Group at Imperial for offering me the fantastic opportunity to do particle physics research, and to the motley crew (Dave Colling, Barry, Rod, Matt Ryan, to name but a few) for making my college time memorable. Michele, Chris, Tim, Phil, Stexo and Liddy: the office just won't be the same without you! And to the élite band of 2001 PhDers – Guy, Jamie, Lisa, Chris and Matt – I really enjoyed sharing the journey with you.

I must thank the British taxpayer who, through PPARC, funded my Ph.D. I've relished every moment: jet-setting to conferences, sharing my work and meeting people from all over the globe. Thanks go to CERN and RAL for wonderful summer schools; I will never forget how we crammed our brains with particle physics while soaking up the atmosphere of Armenian mountains and idyllic Oxfordshire countryside.

Fermilab, where I spent most of my Ph.D., is a weird and wacky place that I will always remember fondly. I thank my friends and collaborators at DØ for opening my eyes to a whole new world. They are some of the most talented, kind and motivated individuals I shall probably ever meet.

Many friends popped up along the way. The UK posse, who created a little corner of England in the heart of the prairie, will not be forgotten and teatime will never be the same again! Tamsin, Em (cookie monster), Anant, MartinII, Dustin, Aidan, Helen (tea lady), DØSi, Paul (pun master), Matt, James, Ben, Nicola, Gavin, Liddy (cake baker extraordinaire), Simon, Stexie and, of course, da boyz Chris, Tim and Phil: we shared so many great times - too many to mention here - but the epic Yellowstone trip, Presidential Towers parties, UK house antics and neverending spam exchanges will, I feel, stand the test of time.

My band of foreign friends showed me that friendship knows no barriers. I will remember Sarosh for his sumptuous Indian feasts, Edi for his famous caipirinhas and Ricardo R. for his love of life and unforgettable smile. Then there were the Fins and their crazy ways, Anne-Catherine (complete with cheeky smile), the ever-lovely Steve Muanza and the Brasileras and Miruna who brightened up ANY party. And, lest I forget, a wise philosopher by the name of Anatoly who possessed an endless supply of Russian jokes (and coffee). Thank you to Abid and Carsten for always

brightening up the trailer, to Satish for some of the most crazy dancing I have ever seen! and to Alex for the peace that permeated 7 Sauk Circle. And to Chivas for being the nicest bartender ever.

During these times my homegrown pals were not forgotten. My wonderful friends – John, Sandie, Dave, Liz, Yerffie, Mattie, Lisa and Lesley – are like family to me and I am touched by their love, kindness and support. Of course, I cannot go without mentioning my flatmate Sebastien - a Fermilab souvenir that I managed to smuggle back to London! Sebby, thank you for being such a warm, lovely, inspiring (not to mention crazy) friend. There's always more to life when you're around. And to Calum, who never stopped believing in me and who I admire so much, I say thank you for sharing this with me. I know our friendship will see us through many more journeys in the future.

I want to say an extra special thank you to my brother Dagan, who is very dear to me. You've always managed to make me laugh, and to make me proud. Despite it being a "slow and bloody process - tears, sweat and a generous helping of apathy", I'm glad we got through it together. I thank my Mum, whose presence I feel every day of my life, for the love she gave me. And to my Dad I send all my love. Thank you for caring. And thank you for all the support and love you've given me over the years.

Finally I want to thank Philip, who has been there for me since the day we met across a crowded trailer. Without me realising it, you have become the light of my life. Thank you to the butterfly that flapped its wings and led us here. I hope that these words will gather dust on our bookshelf for many years to come.

Contents

List of Figures

List of Tables

Preface

"Nature has a great simplicity and therefore a great beauty."

Richard Feynman

This thesis describes work performed as a member of the DØ collaboration from December 2001 to September 2005. The main focus of the work lies in the search for the $Z \rightarrow b\overline{b}$ decay. $Z \rightarrow b\overline{b}$ is an important signature at a hadron-hadron collider: not only does it serve as a benchmark for the decay of a light Higgs boson (into a $b\overline{b}$ quark-antiquark pair), but it is also crucial for calibrating the b-jet energy scale, which has a significant impact on much of the physics done at DØ.

Initially, I carried out studies to investigate the b-jet energy and dijet mass resolutions attainable in both the $Z \rightarrow b\overline{b}$ and $ZH \rightarrow e^+e^-b\overline{b}$ channels, as part of the Jet Energy Scale group. This constituted the first in-depth study of factors affecting the b-jet resolution in Run II at DØ. During this period I was responsible for conducting closure tests of DØ's jet energy scale, which is an algorithm that corrects the jet energies measured in the calorimeter for various detector effects that lead to energy losses. Closure tests are important for certifying the energy scale prior to its release to the collaboration. In essence, they act as cross-checks to see that all jet energy corrections do indeed lead to closure - in other words, recover the energy that was mismeasured in the first place.

In preparation for the search for $Z \rightarrow b\overline{b}$, I then embarked upon trigger studies within the Higgs Trigger group. As part of this, I designed a tailor-made set of

triggers that specifically select $Z \rightarrow b\overline{b}$ events using, for the first time, impact parameter b-tagging at Level 3, thus effectively commissioning these triggers. This proposal was presented to the DØ trigger board experts, who approved the triggers for online operation shortly afterwards. These triggers have been running online successfully since July 2004 and are benefitting from the luminosity improvements delivered by the Tevatron.

Using data collected with these new triggers and also with pre-existing ones, I performed a search for $Z \rightarrow b\overline{b}$ events using the first 300 pb^{-1}. This thesis presents the first signs of this process at DØ. This result represents a significant contribution to the Higgs physics programme at DØ and paves the way for future collaborators to study and harness the potential of $Z \rightarrow b\overline{b}$ at DØ.

The thesis is structured as follows:

- Chapter 1 contains a brief review of the Standard Model, with particular emphasis on those areas relevant to Higgs physics;
- Chapter 2 provides a description of the Fermilab accelerator and the DØ detector;
- Chapter 3 focuses on the study of b-jet energy resolution and dijet mass resolution in the channel central to this thesis, $Z \rightarrow b\overline{b}$, as well as the benchmark Higgs decay $ZH \rightarrow e^+e^-b\overline{b}$;
- Chapter 4 follows the development of a number of triggers designed to select candidate $Z \rightarrow b\overline{b}$ events. The need for such triggers and the philosophy behind them is outlined. A detailed account of the studies performed – including optimisation of the signal efficiency and background rejection – is provided;
- Chapter 5 presents a search for $Z \rightarrow b\overline{b}$ using Run II data at DØ. This includes the selection of the candidate events and the approaches adopted in order to obtain an accurate measurement of the background. Evidence for the $Z \rightarrow b\overline{b}$

decay at DØ is revealed for the first time, and future avenues for the analysis are discussed;

- Chapter 6 provides a summary and outlook.

Chapter 1

In Theory

"Physics is like sex: sure, it may give some practical results, but that's not why we do it."

Richard Feynman

1.1 Overview

In this chapter a brief introduction to the Standard Model of particle physics is presented, with particular emphasis on the electroweak sector of the model which is most relevant to this thesis. The Higgs mechanism is discussed, as are the current limits on the mass of the Higgs boson. Finally, we discuss the motivation behind a search for $Z \to b\overline{b}$ decays at a $p\overline{p}$ collider.

1.2 The Standard Model

The Standard Model (SM) is currently our best description of the fundamental particles and their interactions. A highly successful relativistic quantum field theory, the SM has been shown to agree very accurately with experimental observations[1] (an excellent review can be found in [2]). In our current picture, fundamental particles

[1] One exception is the recent discovery of neutrino oscillations [3] [4]; however, this can be incorporated into minimal extensions to the SM.

are made up of three ingredients: leptons, quarks and force carriers, as illustrated in Figure 1.1. Electromagnetism, described by Quantum Electrodynamics (QED), is combined with the weak force to form the electroweak sector of the SM. The strong nuclear force is incorporated into the SM by a field theory known as Quantum Chromodynamics (QCD).

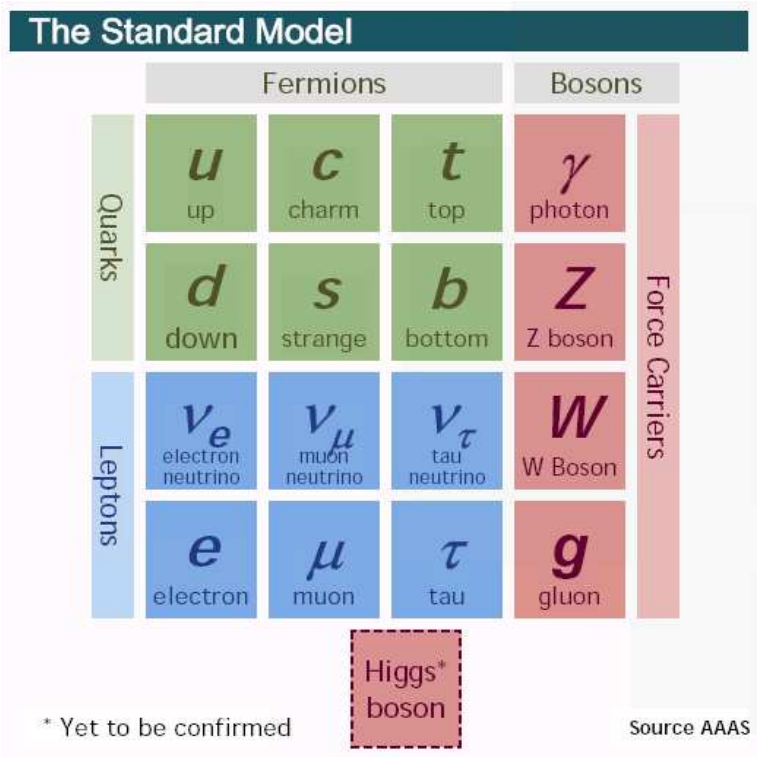

Figure 1.1: The Standard Model, which is a highly successful description of the subatomic world.

Despite being one of the most precisely tested theories to date, the SM does not offer a complete description of the world around us. Fundamental questions remain unanswered. One of the least experimentally verified aspects of the framework is the Higgs sector, which is thought to be necessary for unifying electromagnetism with the weak force. As we shall see, the resulting Higgs field also plays a crucial role in enabling other particles to acquire mass.

1.2.1 Symmetry in Nature

Our understanding of the subatomic physical world rests upon the basic - yet powerful - idea of symmetry. We believe that interactions are dictated by symmetry principles and, thanks to Noether's theorem, that symmetry is intrinsically linked to conservation laws. Moreover, we believe that the conserved physical quantities (such as electric charge, colour, etc.) are conserved in local regions of space, and not just globally.

In classical mechanics, for example, translational symmetry leads to conservation of linear momentum while rotational symmetry results in angular momentum conservation. Similarly, in field theory, the requirement that the SM Lagrangian – i.e., the description of the field in terms of the spacetime coordinates and their derivatives – conserves its properties under certain symmetry operations also imposes tight constraints on the physics it describes. From this central tenet we arrive at a systematic and comprehensive theory of elementary particle dynamics.

1.2.2 Gauge Invariance

Global Changes

The intimate connection beteween symmetries and conservation laws is best described within the framework of Lagrangian field theory [4] [5], in which the Lagrangian term[2], $\mathcal{L}$, describes how a field Ψ, say, varies as a function of the spacetime coordinates and their derivatives. It is convenient to start from the Lagrangian for a free Dirac field (that is, free of sources or interactions), $\Psi = \Psi(x)$:

$$\mathcal{L}_{Dirac} = \overline{\Psi}(i\gamma^{\mu}\partial_{\mu} - m)\Psi. \tag{1.1}$$

Here $\overline{\Psi}$ is the conjugate field defined as $\Psi^{\dagger}\gamma^{0}$, and γ^{μ} represent the 4×4 gamma-matrices.

[2]Technically $\mathcal{L}$ is a Lagrangian density with the Lagrangian given by $L = \int \mathcal{L} d^3x$.

Now, equation 1.1 is invariant under the following transformations:

$$\Psi \rightarrow \Psi' = e^{i\theta}\Psi$$
$$\overline{\Psi} \rightarrow \overline{\Psi}' = e^{-i\theta}\overline{\Psi} \tag{1.2}$$

where θ is any real number. Effectively these transformations multiply Ψ by a unitary 1×1 matrix $U = e^{i\theta}$ such that

$$\Psi \rightarrow U\Psi, \tag{1.3}$$

where $U^{\dagger}U = 1$. Because the transformation is the same at all spacetime points, it is said to be a 'global' gauge transformation (or global phase transformation). The group of all such matrices is known as $U(1)$ and is Abelian, that is, its members commute. The invariance of the Lagrangian under such transformations corresponds to a conserved current - in this case electric charge.

Local Changes

Next, let us consider what happens if the phase factor θ varies between different spacetime points, i.e. $\theta = \theta(x)$:

$$\Psi \rightarrow \Psi' = e^{i\theta(x)}\Psi. \tag{1.4}$$

Under such a 'local' gauge transformation the Lagrangian is no longer invariant, because an extra term is acquired from the action of the partial derivative on $\theta(x)$:

$$\mathcal{L}_{Dirac} \rightarrow \mathcal{L}'_{Dirac} = \mathcal{L}_{Dirac} - \overline{\Psi}\gamma^{\mu}\partial_{\mu}\theta(x)\Psi. \tag{1.5}$$

By now demanding that the whole Lagrangian is invariant under local gauge transformations, we find that the derivative needs to be modified so as to cancel the additional term. ∂_{μ} is replaced by the so-called covariant derviative D_{μ}, which obeys the following transformation:

$$D_\mu \Psi \rightarrow D'_\mu \Psi' = e^{i\theta(x)} D_\mu \Psi. \tag{1.6}$$

This necessitates the introduction of a new real gauge field $A_\mu = A_\mu(x)$ such that

$$D_\mu \equiv \partial_\mu + ieA_\mu. \tag{1.7}$$

Under local gauge transformations A_μ transforms according to the rule

$$A_\mu \rightarrow A'_\mu = A_\mu - \frac{1}{e}\partial_\mu \theta(x). \tag{1.8}$$

By replacing ∂_μ with the new covariant derivative D_μ, the resulting Lagrangian,

$$\mathcal{L}^{GI}_{Dirac} = \overline{\Psi}(i\gamma^\mu \partial_\mu - m)\Psi - e\overline{\Psi}\gamma^\mu \Psi A_\mu, \tag{1.9}$$

becomes invariant under local gauge transformations. (Here the superscript GI indicates gauge invariance.)

The new gauge field A_μ represents a physical photon field that couples to Dirac particles. However, in the desire for a complete Lagrangian one must include both a kinetic energy term and a mass term for the photon field and, as usual, both of these ingredients must be locally gauge invariant. The antisymmetric field tensor $F_{\mu\nu}$, where

$$F_{\mu\nu} = \partial_\mu A_\nu - \partial_\nu A_\mu, \tag{1.10}$$

can be used to construct the following gauge invariant kinetic term:

$$\mathcal{L}^{KE}_{\gamma} = -\frac{1}{4} F_{\mu\nu} F^{\mu\nu} \tag{1.11}$$

which reproduces Maxwell's equations (the superscript KE stands for kinetic energy). The photon field's mass term, which is of the following form:

$$-\frac{1}{2} m_\gamma^2 A_\mu A^\mu \tag{1.12}$$

can only be locally gauge invariant if the photon is devoid of mass (that is, if $m_\gamma = 0$). Fortunately, this prediction is in agreement with all physical observations.

Thus by introducing the massless vector field A_μ to restore local gauge invariance, the complete QED Lagrangian becomes:

$$\begin{aligned}
\mathcal{L}_{QED} &= \mathcal{L}^{GI}_{Dirac} + \mathcal{L}^{KE}_{\gamma} \\
&= \overline{\Psi}(i\gamma^\mu D_\mu - m)\Psi - \frac{1}{4}F_{\mu\nu}F^{\mu\nu} \\
&= \overline{\Psi}(i\gamma^\mu \partial_\mu - m)\Psi + e\overline{\Psi}\gamma^\mu \Psi A_\mu - \frac{1}{4}F_{\mu\nu}F^{\mu\nu}. \qquad (1.13)
\end{aligned}$$

This provides a quantum mechanical description of how Dirac fields (electrons and positrons) interact with Maxwell fields (photons).

The concept of local gauge invariance can also be applied to other symmetry groups. By extension to the $SU(2)$ and $SU(3)$ groups (2×2 and 3×3 matrices respectively), theorists have been able to elucidate the mechanisms underlying the weak and strong nuclear forces, respectively. We now know that three distinct gauge fields (W^+, W^-, Z^0) mediate the weak force, while eight gauge fields (gluons) are involved in colour (QCD) interactions. As opposed to QED, where photon-photon interactions do not occur, the weak and strong force mediators can undergo self-interactions; this is as a result of the non-commutative nature of their symmetry groups.

Ultimately, what arises is a fully gauge invariant theory based on the group $SU(3) \otimes SU(2) \otimes U(1)$: this is commonly known as the Standard Model. However, no mention has yet been made of mass, and before that one needs to become more familiar with the concept of electroweak unification.

1.3 Electroweak Unification

The electroweak sector of the SM describes the interaction of the photon and the W and Z bosons with the quarks and leptons. In 1961, long before the discovery

of the W and Z mediators, Sheldon Glashow made the first step towards unifying electromagnetism and the weak force [6]. He considered a local gauge transformation group $SU(2) \otimes U(1)$ under which the lepton Lagrangian was invariant.

As seen in Section 1.2.2, the $U(1)$ group generates one massless gauge boson. Imposing $SU(2)$ symmetry gives rise to three massless gauge fields. But the underlying $SU(2) \otimes U(1)$ group structure does not directly provide the physical photon or vector boson fields found in nature, and some clever tricks have to be performed to reach this goal.

First, the $U(1)$ field must be thought of in terms of hypercharge[3], Y, rather than electric charge. The resulting $U(1)_Y$ field generates a gauge boson field B_μ (equivalent to A_μ in Section 1.2.2). Second, let us consider the physical consequences of applying $SU(2)$ symmetry. The $SU(2)$ group acts on the isospin of particles and has led to the classification of quarks and leptons (fermions) into doublet and singlet fields of weak isospin, as shown in Table 1.1.

$$\begin{pmatrix} \nu_e \\ e^- \end{pmatrix}_L, \quad \begin{pmatrix} \nu_\mu \\ \mu^- \end{pmatrix}_L, \quad \begin{pmatrix} \nu_\tau \\ \tau^- \end{pmatrix}_L; \quad e_R, \quad \mu_R, \quad \tau_R;$$

$$\begin{pmatrix} u \\ d \end{pmatrix}_L, \quad \begin{pmatrix} c \\ s \end{pmatrix}_L, \quad \begin{pmatrix} t \\ b \end{pmatrix}_L; \quad u_R, \quad d_R, \quad c_R, \quad s_R, \quad t_R, \quad b_R.$$

Table 1.1: The leptons (top line) and quarks (bottom line), grouped into multiplets of weak isospin.

This fermionic structure is determined by the observation of parity violation in the weak interactions; the singlets have zero weak isospin and are right-handed while the doublets possess non-zero isospin and are left-handed. Since only the doublet left-handed fields vary under $SU(2)$ transformations, the group is referred to as $SU(2)_L$. It is worth noting that the structure described in Table 1.1 contains no

[3](Weak) hypercharge is related to electric charge via the 'weak isospin' of a particle. Weak isospin is the property with which fermions can be grouped into multiplets that behave the same way under the weak interaction.

right-handed neutrinos. However, extensions to the Standard Model that incorporate neutrino oscillations and a non-zero neutrino mass are capable of generating right-handed helicity neutrinos.

With these ingredients in hand, the electroweak model gathers both $U(1)_Y$ and $SU(2)_L$ into the same Lagrangian. Following the procedure outlined in Section 1.2.2 for QED – that is, imposing local gauge invariance and constructing a covariant derivative – QED and the weak interaction emerge as manifestations of the same underlying force. The theory generates four vector bosons corresponding to four respective gauge fields: the photon γ that carries electromagnetic charge, the W^+ and W^- bosons that mediate charged-current weak interactions (i.e. transform a member of a fermionic doublet into its partner) and the Z^0 particle, which is responsible for neutral-current weak processes.

As with $U(1)$, the $SU(2)_L \otimes U(1)_Y$ gauge bosons also need to be massless in order for the Lagrangian to remain invariant. But while the photon is massless, it is experimentally known that the W and Z bosons certainly are not. How can their masses be generated? The solution lies in finding a way to break the symmetry of the theory whilst preserving local gauge invariance.

1.4 The Higgs Mechanism

In 1967, Steven Weinberg and Abdus Salam proposed a hypothesis known as 'spontaneous symmetry breaking' [7] that was capable of solving this conundrum. The process successfully imparts mass to the $W^\pm$ and Z^0 bosons while leaving the photon massless, but there is a price to pay: the introduction of at least one scalar field – the Higgs field. The quantum of this field is known as the 'Higgs boson', or H^0 [8] [9] [10]. In 1971, Gerald t'Hooft proved that this theory was renormalisable [11]. Twelve years later, the $W^\pm$ and Z^0 particles were discovered at CERN and the model was finally placed on a firm footing.

The Higgs mechanism postulates the existence of a scalar field that possesses a non-zero vacuum expectation value. Within the SM, this scalar field can be described by a doublet of complex fields ϕ^+ and ϕ^0 of electrical charge $Q = (+1, 0)$ and hypercharge $Y = +1$:

$$\Phi(x) = \begin{pmatrix} \Phi^+ \\ \Phi^\circ \end{pmatrix} \equiv \frac{1}{\sqrt{2}} \begin{pmatrix} \phi_1 + i\phi_2 \\ \phi_3 + i\phi_4 \end{pmatrix}, \tag{1.14}$$

where ϕ_i are scalar fields. Symmetry breaking occurs when a self-interaction (or potential) term for the Φ field, $V(\Phi)$, is added to the Lagrangian describing the electroweak interactions:

$$V(\Phi) = \mu^2 \Phi^\dagger \Phi + \lambda (\Phi^\dagger \Phi)^2. \tag{1.15}$$

where $\Phi^\dagger$ is the Hermitian conjugate of Φ, given by $(\Phi^{+*}\Phi^{\circ *})$. If μ^2 is positive, the minimum of $V(\Phi)$ is at $\Phi(x) = 0$, or more accurately, the vacuum expectation of the field $\Phi(x)$ is 0. In this case, the first term on the right-hand side of equation 1.15 simply describes a massive scalar field. The more intriguing scenario arises when μ^2 is negative. As illustrated in Figure 1.2, the potential acquires a local (unstable) maximum at $\Phi(x) = 0$ along with a set of global minima which we choose to represent using the following vacuum expectation value, ϕ_{vac}, of $\Phi(x)$:

$$\phi_{vac} \equiv \sqrt{\frac{1}{2}} \begin{pmatrix} 0 \\ v \end{pmatrix}. \tag{1.16}$$

Here v is the vacuum expectation value defined by $v = \sqrt{-\mu^2/\lambda}$. We are free to choose the value of the physical vacuum, and by choosing it to have a value other than zero the gauge symmetry is said to be "spontaneously broken". While the Lagrangian remains invariant, the ground state does not; this is the essence of the Higgs mechanism.

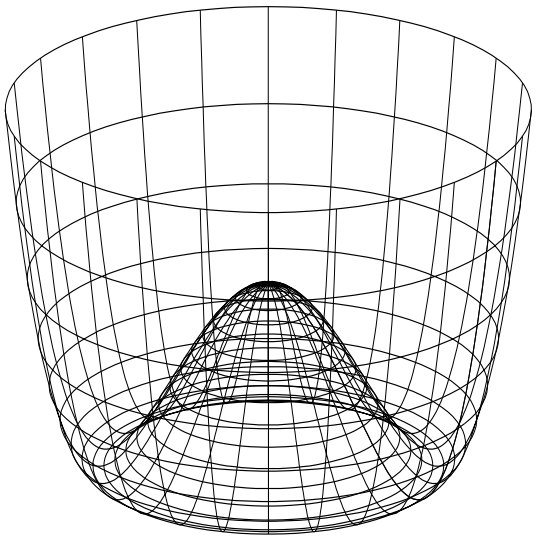

Figure 1.2: Graphical representation of the Higgs potential $V(\phi)$ for the case in which μ^2 is negative.

Near the ground state the symmetry is broken and the scalar field can be written as

$$\phi_{vac} = \begin{pmatrix} 0 \\ v + h(x) \end{pmatrix}, \tag{1.17}$$

where h(x) is the physical Higgs field. Three of the four lost degrees of freedom are used to generate masses for the $W^{\pm}$ and Z^0 bosons:

$$M_W = \frac{1}{2} v g; \quad M_Z = \frac{1}{2} v \sqrt{g^2 + g'^2} = \frac{M_W}{\cos\theta_W} \tag{1.18}$$

where θ_W is the Weinberg angle, and g and g' are related by the expression $g \sin\theta_W = g' \cos\theta_W = e$, where e is the magnitude of the electron charge (in Coulomb). The fourth degree of freedom gives rise to a massive neutral Higgs boson, whose mass is given by:

$$M_H = \sqrt{2v^2\lambda}. \tag{1.19}$$

In a similar way, mass terms for the fermions can be generated in a gauge invariant way by starting from the same scalar doublet.

To summarise, then, a method of giving mass to the gauge fields has been established in principle. Despite the attractiveness of this approach, however, the chapter is far from closed. First, an extra scalar particle has been acquired - the Higgs boson - which has not yet been discovered. Second, the Higgs mechanism generates fermion masses but does not predict their values; instead these parameters have to be fed into the model by hand, which is rather unsatisfactory. Third, the mass of the Higgs itself is not predicted, although current evidence favours a relatively light Higgs that could be within discovery reach [12].

1.5 Pinning Down The Higgs

The mass of the Higgs boson is the only free parameter in the Higgs sector of the SM; once it is known, all other variables such as branching fractions, width, production cross-sections and couplings can be derived. Constraints can be placed upon the Higgs mass from theory, indirect experimental evidence and direct searches.

1.5.1 Constraints From Theory

Theoretical consideration of longitudinally polarised WW scattering imposes an upper limit of about 1 TeV/c^2 on the Higgs mass. The constraints can be made tighter by studying the value of λ, the quartic coupling of the Higgs potential that appears in equation 1.15 [13]. λ must be greater than zero, otherwise the Higgs potential loses its minimum and the vacuum is no longer stable. An upper limit on the Higgs mass is derived by considering the running value of the coupling λ, and the way in which Higgs boson loops modify this coupling. $\lambda(\Lambda)$ must be less than infinity, where Λ is the energy scale at which new physics could enter. Such arguments lead to allowed and forbidden regions of Higgs mass space, as shown in Figure 1.3.

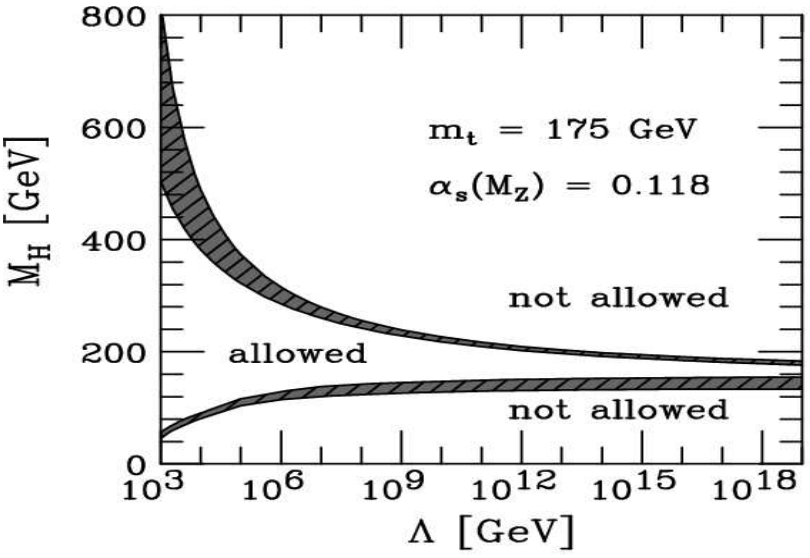

Figure 1.3: Theoretical bounds on the mass of the Higgs boson as a function of Λ, the energy scale at which new physics (beyond the Standard Model) could arise [13].

1.5.2 Indirect Experimental Limits

One way to place a limit on the Higgs mass is to measure various electroweak parameters which are affected by higher order loop corrections involving the Higgs. Figure 1.9, for example, illustrates how Higgs processes enter into the $Z \rightarrow b\overline{b}$ decay. The W mass also undergoes corrections due to both the Higgs mass and the top quark mass; in fact, M_H depends logarithmically on M_W and M_{top}. Thus by accurately measuring the masses of the W boson and top quark one can constrain the Higgs mass, as illustrated in Figure 1.4.

Other electroweak observables exhibit similar dependencies on the Higgs mass and can be combined to form a global fit that constrains the allowed mass range. Figure 1.5 shows the $\Delta\chi^2$ curve derived from high-Q^2 precision electroweak measurements [14], performed at LEP, the SLC and the Tevatron, as a function of Higgs mass (assuming the SM to be correct). The preferred value for the Higgs mass, corresponding to the minimum of the parabola, is at 89 GeV/c^2, with an experimental uncertainty of +42 and -30 GeV/c^2. Such indirect measurements imply that M_H is less than 260 GeV/c^2 at the 95% confidence level. This provides a valuable guide to

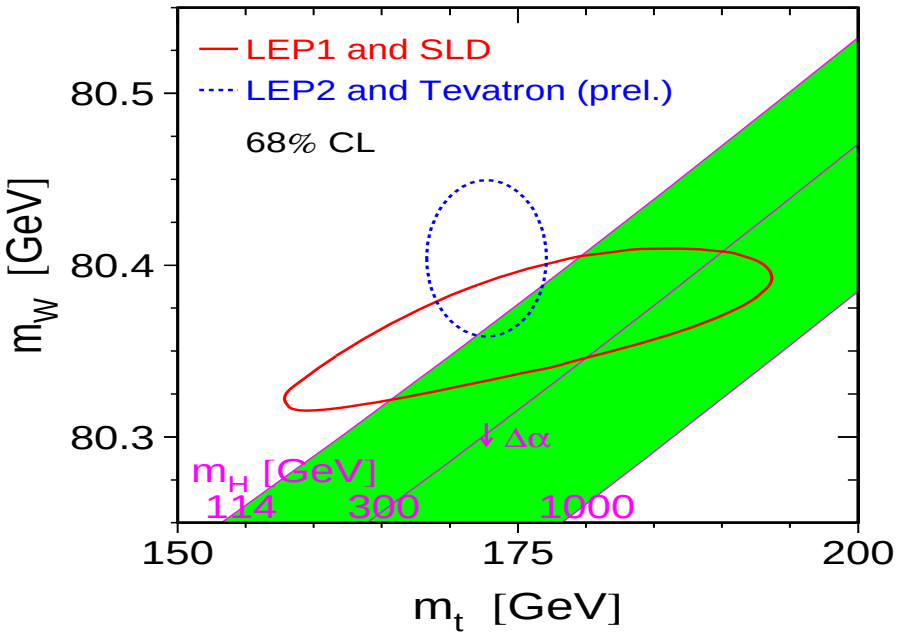

Figure 1.4: Contour plot showing the experimental constraints on the Higgs mass from electroweak measurements [14].

the mass range in which experimentalists should look for the Higgs. The Tevatron has a better chance of finding the Higgs than the LEP or SLC as a result of its higher centre of mass energy, attainable because a hadron-hadron collider does not suffer from the synchrotron radiation losses that occur at an e^+e^- collider.

1.5.3 Direct Searches For The Higgs

Direct searches for the Higgs must exploit the Higgs production mechanisms and decay channels that are most suitable to the collider under study. Searches have been performed at both LEP and the Tevatron. At the LEP experiments the primary production process for the Higgs is $e^+e^- \rightarrow HZ$, with the H decaying to $b\bar{b}$ and all possible decays of the Z boson. Using data taken at centre of mass energies between 189 and 209 GeV, LEP was able to rule out the existence of a Higgs boson lighter than 114.4 GeV/c^2 at the 95% confidence level [12]. This excluded region is

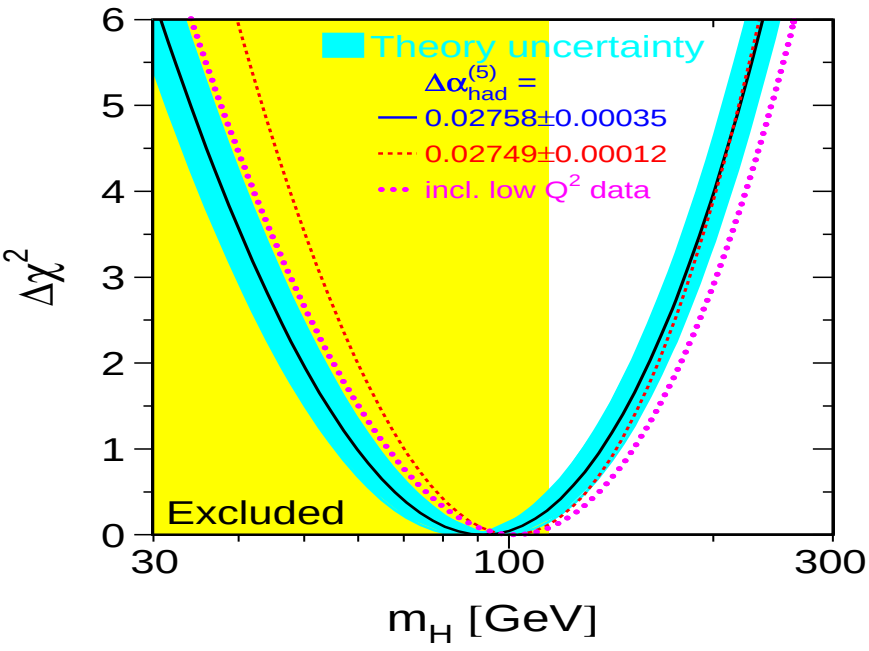

Figure 1.5: Constraints imposed on the Higgs mass from global likelihood fits of electroweak observables [14].

represented by the shaded (yellow) portion in Figure 1.5.

At the Tevatron's $p\overline{p}$ collider, the situation is made more complicated by the hadronic environment. Figures 1.6 and 1.7 show the various mechanisms by which the Standard Model Higgs is produced and decays, respectively [15]. The production process with the largest cross-section is gluon-gluon fusion as seen from Figure 1.6). However, in the low mass region ($m_H < 135$ GeV/c^2), where the Higgs decays primarily to a $b\overline{b}$ pair (Figure 1.7), this channel is overwhelmed with background from generic QCD processes. The more promising modes at the Tevatron are the production of the Higgs boson in association with either a W or Z boson - processes that are a factor of three lower in cross-section. Here, the leptonic decay products of the W/Z provide handles against the more copious SM background. For a heavier SM Higgs ($M_H >$135 GeV/c^2) the dominant decay mode is $H \rightarrow WW^*$; in this case one can take advantage of the higher gluon-gluon fusion production cross-section.

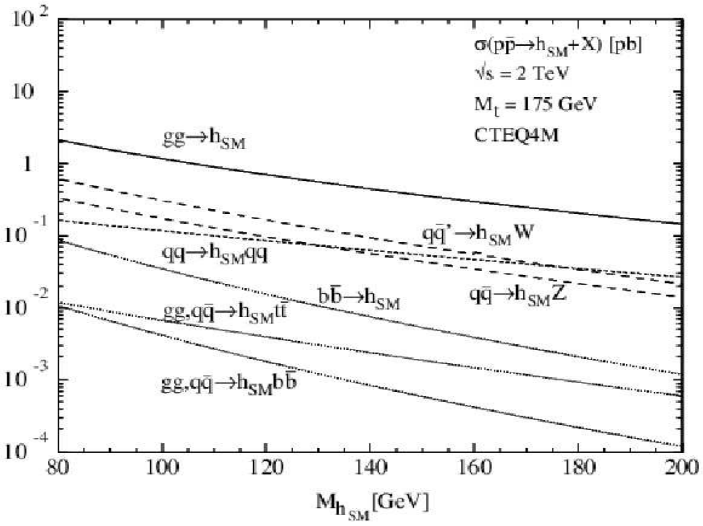

Figure 1.6: Higgs production cross-section at the Tevatron.

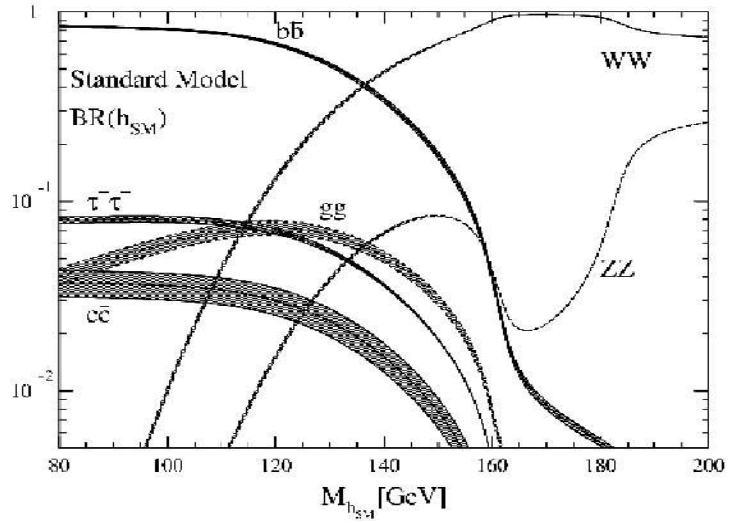

Figure 1.7: Standard Model Higgs decay modes as a function of Higgs mass.

The CDF and DØ experiments at the Tevatron have both performed searches for the Higgs at a centre of mass energy of 1.96 TeV. As yet no indication of the Higgs has been found, but by combining the power of different search methods, a single upper limit on Higgs boson production can be set. Tantalising hints at LEP of a Higgs at a mass of about 115 GeV/c^2 [12] have encouraged Tevatron researchers that the Higgs may be within reach using the luminosity that will be delivered by the end of Run II.

Detailed studies have been undertaken to evaluate the Higgs sensitivity that can be expected from the current run of the Tevatron [16]. These results, summarised in Figure 1.8, indicate that our searches will become very interesting at 2 fb^{-1}. At the present time, DØ has performed Higgs searches in all channels using data corresponding to an integrated luminosity of 0.35 fb^{-1}. We can project up from this luminosity, applying anticipated improvements to the analyses, to conclude that DØ will need about 2 fb^{-1} of data to explore beyond the Higgs mass limit set by LEP, in agreement with the predicted Higgs sensitivity reach. Given the current Tevatron performance, this luminosity could be expected within the next year or so.

1.6 Why Search For $Z \to b\overline{b}$?

The decay of a Z boson into a b quark and a $\overline{b}$ quark does not represent a radically new piece of physics. Millions of $Z \to b\overline{b}$ events have already been observed at LEP and at the SLC, where the Z resonance was studied in great depth [17], and the underlying physics process is well understood. Figure 1.9 shows the Feynman diagrams for the leading order $Z \to b\overline{b}$ process as well as contributions from higher order effects. It remains, however, an essential physics tool at a hadron-hadron collider and the study, observation and measurement of $Z \to b\overline{b}$ is an important part of the Run II physics programme at DØ.

The major impetus behind the search is that $Z \to b\overline{b}$ serves as an important benchmark for Higgs physics: it is the closest observable process to the decay of a

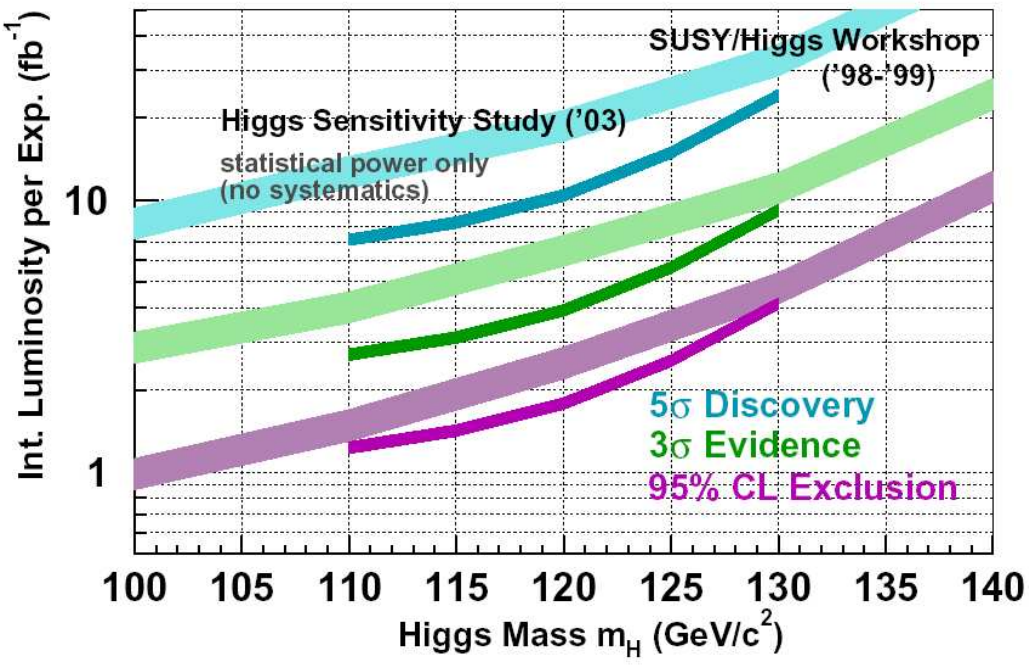

Figure 1.8: Predicted Higgs sensitivity reach of the Tevatron collider in Run II. Integrated luminosity per experiment (DØ and CDF) is plotted as a function of Higgs mass, for 95% confidence level exclusion (purple, bottom contour), 3σ evidence (green, middle contour) and 5σ discovery (blue, top contour), for a mass range of 90–200 GeV/c^2. The narrow curves come from the updated sensitivity analysis (2003) [16]; the thicker curves show the results of the previous sensitivity study (2000) [15].

light Higgs to $b\bar{b}$. If the Higgs is to be discovered in this way, it is crucial to measure the b-jet energy resolution and $b\bar{b}$ mass resolution with high precision. The knowledge of jet energy resolution, dijet mass resolution, b-tagging and useful kinematic handles gleaned from studying $Z \to b\bar{b}$ can be used to refine Higgs searches at a hadron-hadron collider, and will be highly relevant for the LHC era. Our main challenge is to sufficiently reduce backgrounds such that $b\bar{b}$ events from the Z can be observed. To this end, careful analysis techniques are critical and only the most effective triggers must be employed.

$Z \to b\bar{b}$ is also a particularly important tool in the calibration of the b-jet energy scale, which affects many analyses of the high-p_T physics at the Tevatron. The current uncertainty on the jet energy scale - of the order of 3% - dominates the uncertainty on the mass of the top quark. An improved measurement of the b-jet

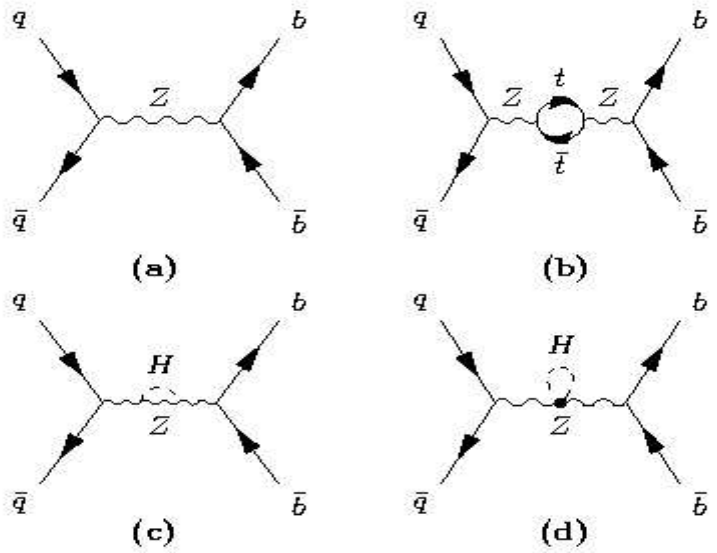

Figure 1.9: Feynman diagrams representing the $Z \to b\bar{b}$ decay. (a) Leading order $Z \to b\bar{b}$ process; (b) top quark loop correction to $Z \to b\bar{b}$; (c), (d) Higgs loop corrections to $Z \to b\bar{b}$.

energy scale can further constrain its mass, and thus help to pinpoint the mass of the Higgs if it exists. In addition, $Z \to b\bar{b}$ can be used to improve the understanding of jet energy resolution more generally.

This thesis describes the first search for $Z \to b\bar{b}$ at DØ in Run II of the Tevatron collider.

Chapter 2

The DØ Detector

"The machine does not isolate man from the great problems of nature but plunges him more deeply into them."

Antoine de Saint-Exupéry

2.1 Overview

In this chapter there follows a brief overview of the apparatus used, including a discussion of the proton-antiproton acceleration and collision processes at the Tevatron collider. Details of DØ's main detector subsystems are given, including the tracking system, calorimeter, muon detectors and trigger framework, with emphasis on the components that are most relevant to this thesis.

2.2 A Brief History

The DØ detector is a multi-purpose particle physics detector designed to study proton-antiproton collisions at the Tevatron collider, situated at Fermi National Accelerator Laboratory (Fermilab) in Illinois, U.S.A. Initially the intention was to build only one experiment – the Collider Detector at Fermilab (CDF) – to study the wealth of physics that would be accessible at the Tevatron. However, it was soon

realised that a second experiment was necessary to provide verification and cross-checking of the physics results. Hence the DØ experiment was born. Conceived in 1983, DØ's original detector was based around an excellent uranium/liquid-argon sampling calorimeter and a muon detector with extensive geometrical coverage [18]. During Run I of the Tevatron, which lasted from 1992–1996, the detector probed collisions at a centre-of-mass energy of 1.8 TeV. This highly successful period of data-taking contributed to major strides in our understanding of particle physics today. Most noteworthy was the discovery of the top quark in 1995 [19] in collaboration with CDF, but many other significant advances were made, for example, in our understanding of jet production, precision measurements of the W boson and greatly-improved limits on the production of new phenomena. With such successes under its belt, Run I drew to a close and the Tevatron shut down in order to undergo significant accelerator upgrades [20]. The goal was to extend the physics reach of the machine by a) boosting the centre-of-mass energy to 1.96 TeV and b) enlarging the data sample collected (by increasing the instantaneous and hence the integrated luminosities that could be delivered). By 2001, the new and improved accelerator was ready and Run II of the Tevatron began.

In preparation for Run II, the DØ Collaboration embarked upon an ambitious programme of detector upgrades [21] [22] in order to cope with the new accelerator and to extend DØ's overall physics capability. Most notably, a new and improved tracking system was added to complement the already excellent calorimetry and muon detection inherited from Run I. Furthermore, the electronics and trigger systems were completely revamped in order to handle the shorter bunch spacing. The various subcomponents of the Run II detector are visited in Sections 2.4.2 to 2.4.5, after a brief tour of the Tevatron machine.

2.3 The Tevatron

Fermilab is home to the Tevatron [20], the highest-energy particle accelerator that is currently operating in the world. An aerial view of the accelerator complex is shown in Figure 2.1, and a schematic of the accelerator complex is shown in Figure 2.2.

Figure 2.1: Aerial photograph of the Fermi National Accelerator Laboratory (Fermilab) in Batavia, Illinois, U.S.A. The Tevatron accelerator is located deep underground, inside the larger of the two rings shown. Courtesy of [23].

2.3.1 Proton And Antiproton Production

The first stage involves proton production. Protons are obtained by stripping electrons from negatively-charged hydrogen ions. Firstly, bunches of hydrogen ions are accelerated to an energy of 750 keV by the Cockroft-Walton accelerator indicated in Figure 2.2. A linear accelerator boosts the ions' energy to 400 MeV and the ions are then focused onto a thin graphite sheet, a process which strips them of their electrons to leave just bare protons. The Booster, a small synchrotron accelerator, then accelerates these protons to 8 GeV, at which point they are ready to be inserted into the Main Injector.

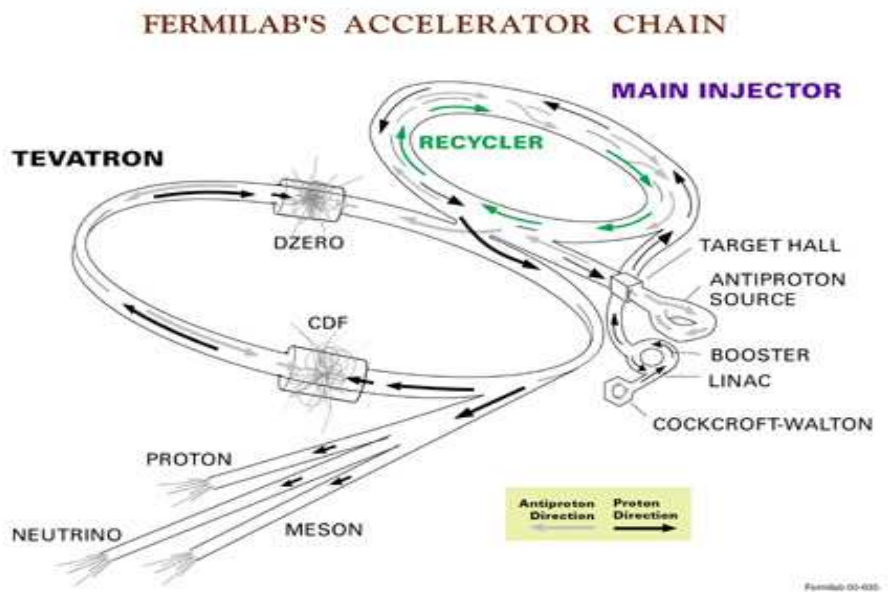

Figure 2.2: Schematic of the Tevatron accelerator complex at Fermilab. After acceleration, the proton and antiproton beams are collided at two points around the ring: the DØ and CDF experiments.

The Main Injector is a three-kilometre-circumference synchrotron located in a separate beam tunnel adjacent to the Tevatron (as illustrated in Figure 2.2), which accelerates protons and antiprotons up to 150 GeV prior to injection into the Tevatron ring. Bunches of protons from the Main Injector are also extracted to produce antiproton bunches: a 120 GeV proton beam is fired at a nickel target to yield antiprotons, and those with an energy close to 8 GeV are then collected with the aid of a lithium lens.

The antiproton yield is low – typically 10^5 collisions are required to collect one antiproton – and they emerge with a relatively broad distribution of energies and a wide range of angles. The main challenge lies in producing sufficiently dense bunches of antiprotons; the solution is to 'cool' the antiproton beam in one of two ways. 'Stochastic cooling' works by measuring the position of each antiproton bunch as it passes through a region of the Accumulator Ring (the magnetic storage ring located next to the antiproton source that feeds the Tevatron). Using this information, the antiprotons are given an appropriate 'kick' to correct their spread in momentum.

The second approach that has recently been implemented is known as 'electron cooling' [24]. Each bunch of antiprotons is mixed with a bunch of electrons travelling at the same average speed. The electrons collide with the antiprotons, causing slower antiprotons to speed up and faster ones to slow down; in the process the electrons heat up while the antiprotons are cooled. These cool antiprotons are then passed into the Recycler Ring for storage. Following storage, the Recycler, which is located in the same tunnel as the Main Injector, feeds antiprotons to the Main Injector where they are subsequently accelerated to an energy of 150 GeV.

2.3.2 Proton-antiproton Collisions

The next link in the chain is the Tevatron itself. Six kilometres in circumference, the Tevatron is housed in a tunnel nearly ten metres below ground. It accelerates bunches of protons and antiprotons to 980 GeV, in two counter-propagating beams circulating within the same beam pipe. The protons and antiprotons are brought to a focus for collision at two points around the ring: the DØ and CDF experiments.

The Tevatron operating parameters are presented in Table 2.1, for both the Run I and Run II eras. Peak values of the instantaneous luminosity are around 0.5×10^{32} cm^{-2}s^{-1} for the data explored in this thesis. Run IIb, the second half of Run II lasting from 2006 to 2009, will offer significantly higher instantaneous luminosities. As such, the number of interactions per bunch crossing will increase.

2.3.3 Current Status of The Accelerator

Despite a slow start to Run II with lower than expected luminosity, the performance of the Tevatron now exceeds the design prediction for both peak luminosity and weekly integrated luminosity. Figures 2.3 and 2.4 show how these luminosities have increased since the beginning of Run II. To date the Tevatron has delivered a total integrated luminosity of 1.55 fb^{-1} and Figure 2.5 plots the luminosity that is expected by the end of Run II.

	Run I	**Run II**
Running period (*expected*)	1993–1995	2001–*2009*
Energy $p\bar{p}$ (GeV)	900	980
Proton bunches	6	36
Antiproton bunches	6	36
Protons/bunch	2.3 x 10^{11}	2.7 x 10^{11}
Antiprotons/bunch	5.5 x 10^{10}	4.2 x 10^{10}
Bunch spacing (ns)	3500	396
Peak luminosity ($cm^{-2}s^{-1}$)	0.16 x 10^{32}	1.0 x 10^{32}
Integrated luminosity (pb^{-1}/week)	3.2	20.0

Table 2.1: Tevatron operating parameters for Run I and Run II. For the current status of the Tevatron see [25].

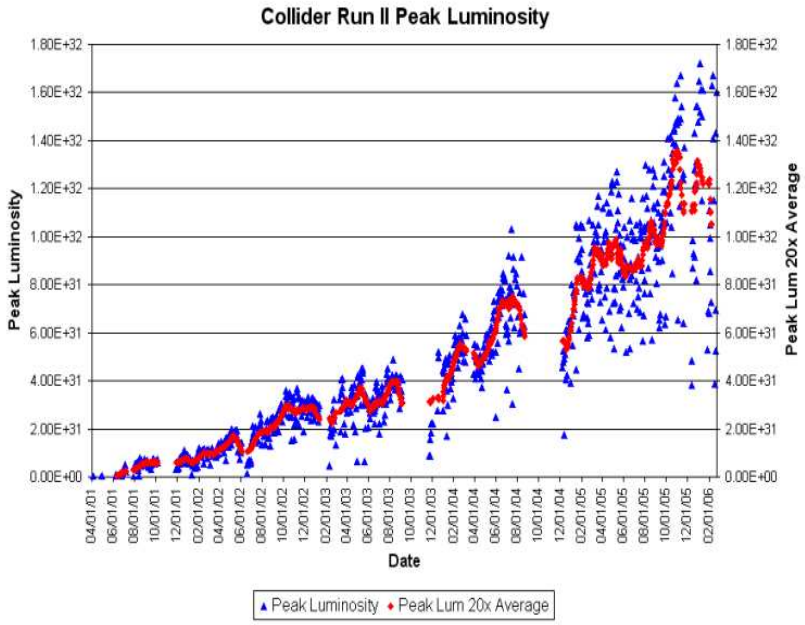

Figure 2.3: Peak luminosity delivered by the Tevatron during Run II [26].

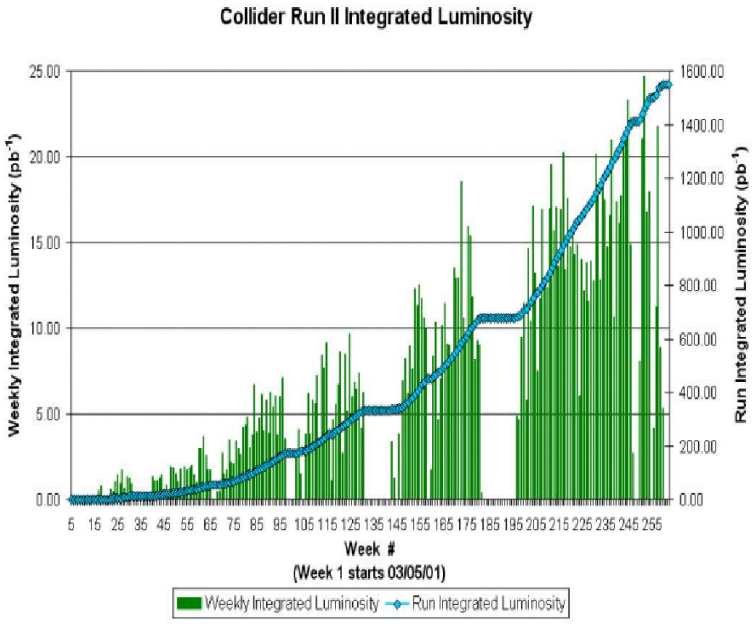

Figure 2.4: Integrated luminosity delivered by the Tevatron during Run II [27].

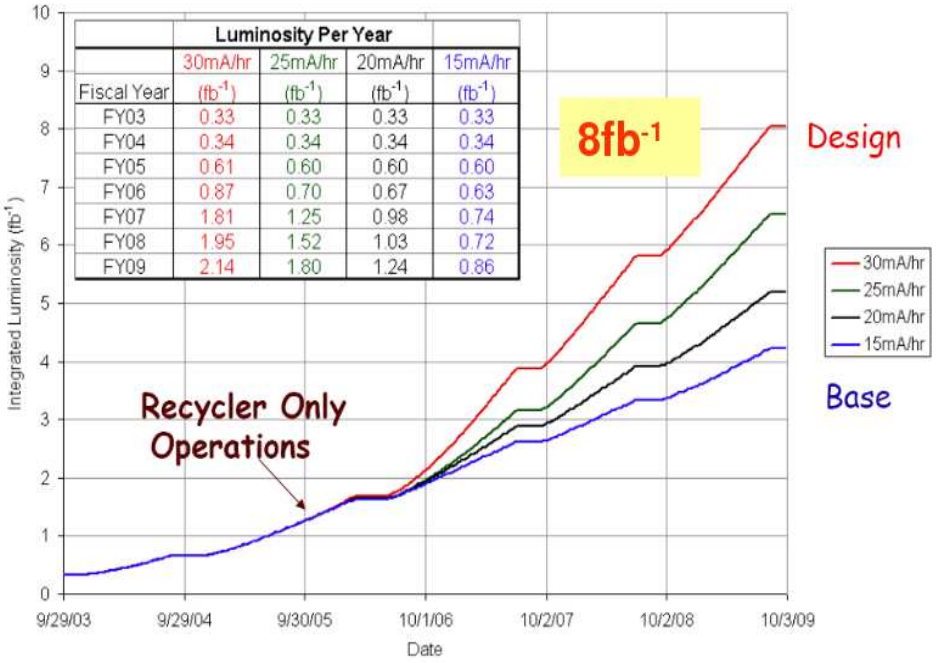

Figure 2.5: The integrated luminosity that is expected by the end of Run II of the Tevatron [28].

The key factor limiting the integrated luminosity that can be delivered is the antiproton production rate. A series of projects [29] are underway to improve this by:

- increasing the number of protons on the antiproton production target;
- increasing the antiproton collection efficiency;
- streamlining and improving antiproton transfers from the Accumulator to the Tevatron.

Provided these improvements continue to progress well, we expect to accumulate a total luminosity of 8 fb^{-1} by the end of Run II in 2009.

2.4 The DØ Detector

The DØ detector [21] [22] has a similar layout to many other modern large scale collider physics detectors. Since the Tevatron beams possess the same energy, the detector was designed to be as symmetric as possible with respect to its centre. It consists of a variety of different subdetectors positioned around the proton-antiproton collision point. As shown in Figure 2.6, they are, from the interaction point outwards:

- a vertex detector: the Silicon Microstrip Tracker (SMT);
- a central tracker: the Central Fibre Tracker (CFT);
- a solenoidal magnet to provide the central magnetic field used for tracking and identification of charged particles;
- a calorimeter consisting of three cryostats;
- a three-layer muon detector with a toroidal magnet.

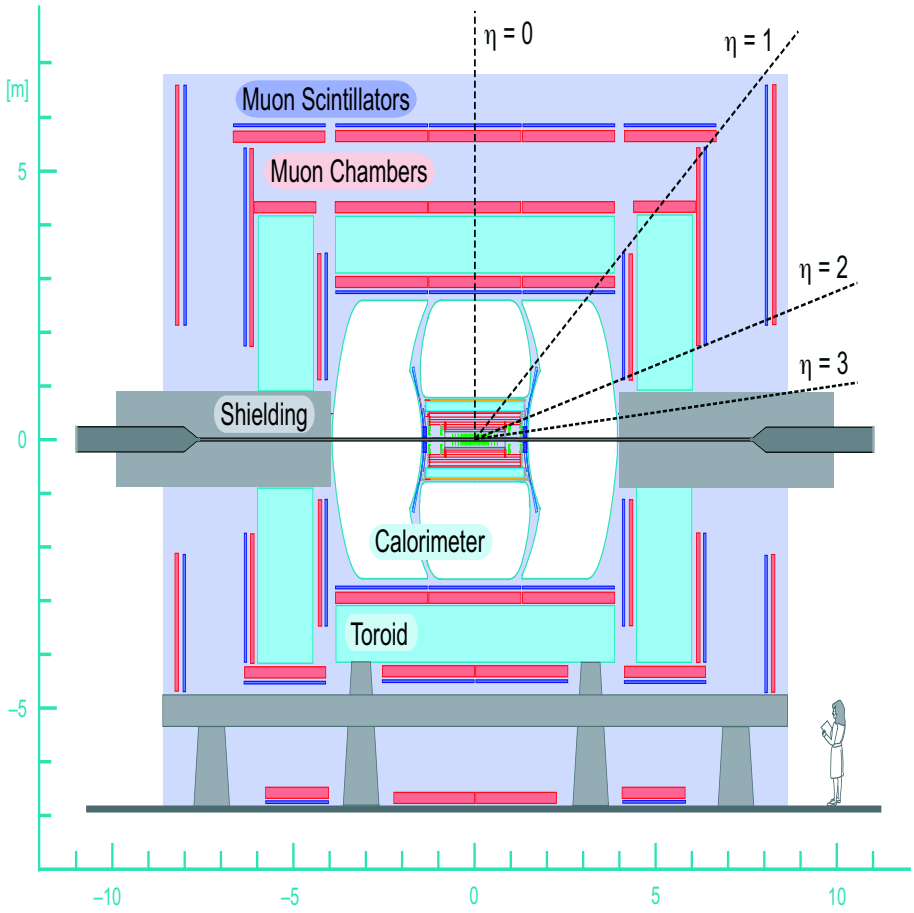

Figure 2.6: Side view of the DØ Run II detector. From the interaction point outward one can see the Silicon Microstrip Tracker (SMT) and Central Fibre Tracker (CFT) tracking components with their solenoid magnet, surrounded by the calorimeter in its three cryostats and the muon system with its toroidal magnet.

2.4.1 Coordinate System

The coordinate system used at DØ (and therefore the system adopted throughout this thesis unless otherwise specified) has its origin at the centre of the detector, i.e. the nominal proton-antiproton interaction point. The z-axis points along the proton beam, the x-axis points horizontally outward from the centre of the Tevatron ring, while the y-axis points upward. The common spherical coordinate system (r, θ, ϕ) - where r is the perpendicular distance from the z-axis, θ is the azimuthal angle and ϕ is the polar angle (by definition, $\theta = 0$ is along the proton beam direction and $\phi = 0$ is at the positive x-axis) - is replaced by (r, ϕ, η), where η is the pseudorapidity,

defined as:

$$\eta = \text{-ln}(\tan\frac{\theta}{2}). \tag{2.1}$$

The pseudorapidity approximates the true rapidity of a particle. The term "forward" is used to describe regions at large $|\eta|$.

Since some particles escape down the beam pipe and the initial momenta of the interacting partons are not known, momentum, energy and missing energy are often measured in the direction perpendicular to the beam axis - i.e. transverse momentum (p_T), transverse energy (E_T) and missing transverse energy ($\not\!\!E_T$).

In addition, it is often convenient to parametrise the distance between objects in $\eta - \phi$ space in terms of a 'cone' distance, dR, defined as:

$$dR = \sqrt{(\Delta\phi)^2 + (\Delta\eta)^2}. \tag{2.2}$$

2.4.2 Tracking

DØ's tracking system consists of two major components: an inner silicon tracker and an outer scintillating fibre tracker, both located within a 2 Tesla field supplied by a superconducting solenoid, as shown in Figures 2.7 and 2.8. On the outer face of the solenoid is a central preshower scintillator, while forward preshowers are located on the inner face of the forward calorimeters. Taken as a whole, this upgraded tracking system is designed to provide tracking out to large pseudorapidities ($|\eta| < 3$), as well as to identify vertices with high resolution, particularly displaced vertices originating from b-quarks - a crucial element to many aspects of physics at DØ. In addition, the tracking system is capable of measuring the momenta of charged particles, identifying electrons and offering e/π separation.

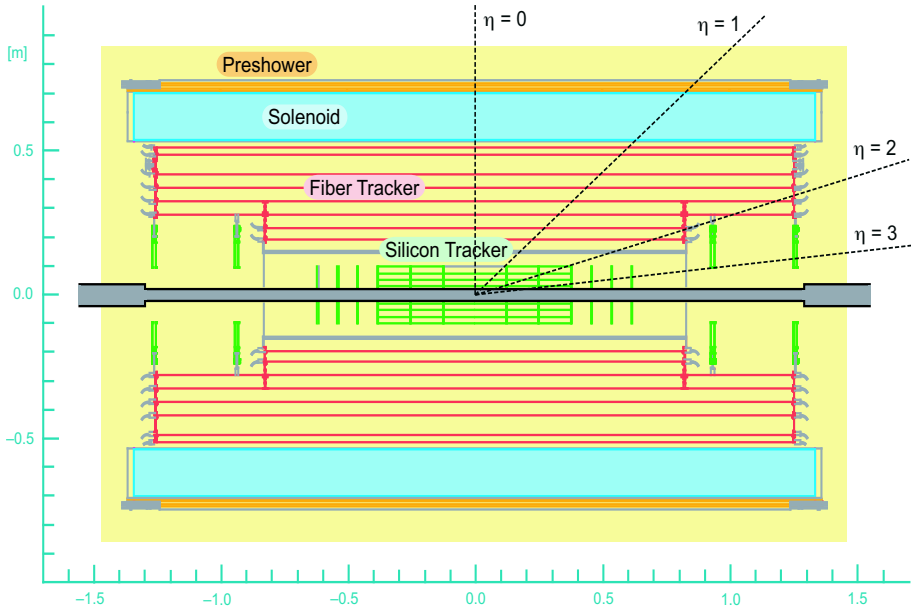

Figure 2.7: Two-dimensional map of DØ's tracking system in η-ϕ space. From the nominal interaction point outwards one finds the Silicon Microstrip Tracker surrounded by the Central Fibre Tracker, a 2 Tesla solenoid magnet and finally the preshower detectors. The tracking components offer a large pseudorapidity coverage out to $\eta < |3|$.

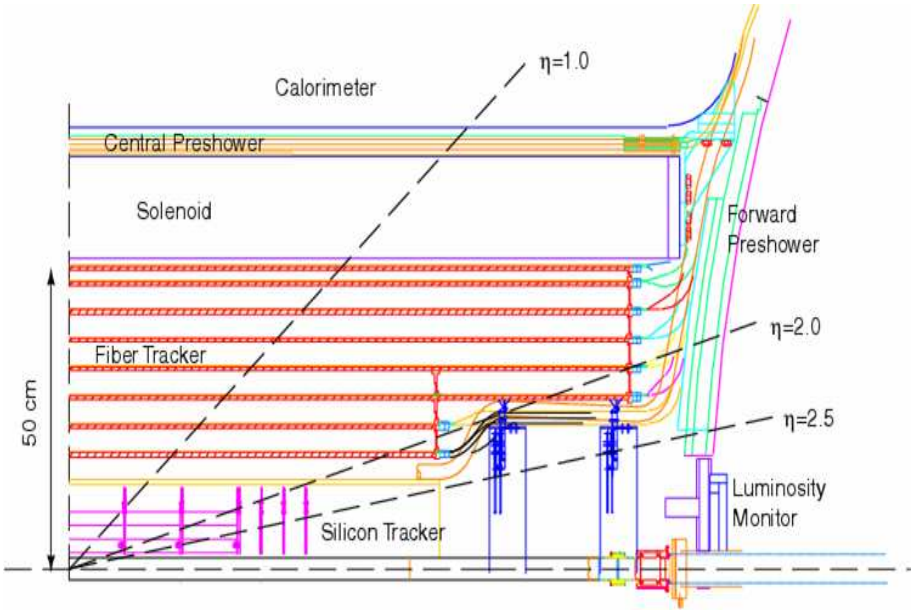

Figure 2.8: Side view of a quadrant of the tracking system in relation to the preshower detectors and calorimeter.

The Silicon Microstrip Tracker

Figure 2.9 shows the DØ Silicon Microstrip Tracker (SMT) [30] [31]. The design of the silicon tracker is dictated mainly by the accelerator environment. The length of

the interaction region (∼25 cm) sets the length scale of the device, and the silicon must be radiation tolerant. The SMT is comprised of three parts: central barrels, F-disks and H-disks. The barrels - six cylindrical components in the central region - are located three on either side of the interaction point. Each barrel has four silicon readout layers. The silicon modules installed in the barrels are known as "ladders". Layers 1 and 2 have twelve ladders each, while layers 3 and 4 have 24 ladders each, giving 432 ladders in total.

In addition to the barrels, the SMT contains disk-shaped detectors of two types: twelve F-disks that are positioned between and outside the barrel components and, at larger z, four H-disks that provide tracking at high $|\eta|$. Overall the SMT has an outer radius of 16 cm (26 cm incorporating the H-disks).

The F-disks are each made from twelve double-sided wedge-shaped detectors. Six of the F-disks are located between the barrels, while the other six form two triplets of disks near the ends of the outermost barrels, as shown in Figure 2.9. Mounted on each H-disk are 24 full wedges, each consisting of two back-to-back single-sided "half" wedges. The H-disks are placed just over one metre away from the interaction point.

Each ladder or wedge contains readout modules known as strips, most with a pitch of 50 μm. In total there are 912 strips read out by almost 800,000 channels. Signal/noise performance in the SMT varies with detector type from 12:1 to 18:1.

The Central Fibre Tracker

The tracking volume between the silicon and preshower detectors is filled by a scintillating fibre tracker. The Central Fibre Tracker (CFT) is designed to provide track reconstruction and momentum measurement for charged particles out to $|\eta| < 2.0$. It also sends tracking information to the trigger, within the range $|\eta| < 1.6$.

The CFT [32] consists of 76,800 scintillating fibres mounted on eight concentric cylinders. Each cylinder contains two layers, one for axial readout and the other at

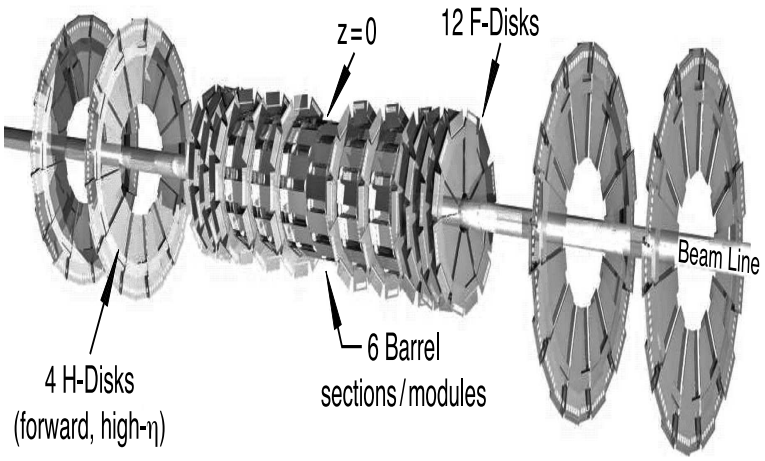

Figure 2.9: Three-dimensional view of the SMT. The six central barrels surround the proton-antiproton interaction region (a 1 metre region of z space). Beyond this, the twelve F-Disks and four H-Disks can be seen.

a 3° stereo angle, in order to allow for additional reconstruction of the z-coordinate. The stereo layers alternate between having negative and positive stereo angles. Fibres are positioned with an accuracy of 25 μm in r-ϕ, and a hit in the CFT detector is measured with an accuracy of 100 μm in r-ϕ and an efficiency of around 98%.

Light production in the fibres consists of a multistep process. Every scintillating fibre has at its centre a polystyrene core of radius 835 μm. The polystyrene is doped with an organic fluorescent dye, paraterphenyl. Excitations within the polystyrene are rapidly tranferred to the paraterphenyl which fluoresces, emitting light at 340 nm. In order to extract the light from the detector, a second dopant, 3-hydroxyflavone, is added to absorb the 340 nm radiation and re-emit it at a wavelength of 530 nm which is transmitted through the polystyrene well. The polystyrene core is embedded within a thin inner acrylic layer and outer fluoroacrylate layer, so as to provide superior mechanical strength in comparison to a single-clad fibre.

The photons are detected by visible light photon counters (VLPCs) that are connected to the scintillating fibres via 7-11 m long waveguides and housed in a cryostat underneath the detector. These connecting waveguides are chemically and structurally similar to the scintillating fibres but contain no dopants. The VLPCs

[21] are essentially low-temperature solid-state photomultiplier tubes. They can detect single photons rapidly, offer a large gain (approximately 50,000 electrons per converted photon) and possess a high quantum efficiency (>75%).

Solenoid Magnet

The measurement of charged particle momenta is determined from the curvature of the particle's track in a magnetic field. At DØ, the field for this purpose is provided by a superconducting solenoid of length 2.73 m and diameter 1.42 m. Factors that constrain the magnet's design included the space available inside the calorimeter, the tracking volume, momentum resolution, ability to operate at both polarities and field uniformity. The result of such considerations was a two-layer superconducting coil that produces a field of magnitude 2 Tesla in the proton or antiproton direction, corresponding to a stored energy of 5.6 MJ. In order to provide a uniform field, the ends of the solenoid coil have higher current density. Within the tracking volume the field is designed to be uniform to an accuracy of 0.5%.

Tracking Performance

Working together, the SMT and CFT detectors locate the primary interaction vertex with a resolution (in the impact parameter, or distance of closest approach) of about 35 μm along the beamline. They are capable of tagging b-quark jets with an impact parameter resolution less than 15 μm in $r-\phi$ for particles with $p_T > 10$ GeV/c at $|\eta| = 0$. The combined design resolution in p_T is $0.0015 p_T$, where p_T is in GeV/c [21], and the high resolution of the vertex position allows good measurement of lepton p_T, jet E_T and $\not\!\!E_T$.

Preshower Detectors

The preshower (PS) detectors, positioned between the solenoid and calorimeter, act as a thin scintillator calorimeter layer. They contribute to electron identification and offer additional background rejection, both during the online triggering of events and

offline. Furthermore, the preshowers help to match tracks to calorimeter showers and compensate for energy losses in the central region due to the presence of the tracking system. Energy deposited in the PS is included in the measurement of the energy of electromagnetic (EM) objects[1] that have already initiated an electromagnetic cascade inside the solenoid magnet.

There are two sets of preshower components: the central preshower detector (CPS) and the forward preshower detector (FPS). The CPS is located in the 5 cm gap between the solenoid and the central calorimeter, and covers the region $|\eta| < 1.2$. The two FPS detectors (north and south) are mounted on the inner surfaces of the end calorimeters and cover the pseudorapidity range $1.4 < |\eta| < 2.5$.

Both the CPS and FPS are made from scintillator strips that are triangular in cross-section. Embedded at the centre of each such strip is a wavelength-shifting fibre that collects and carries the light to the end of the detector. At the readout end, fibres are grouped into bundles of sixteen and connected to clear light-guide fibres. The scintillator technology exploited in these strips is almost identical to that used in the CFT, therefore they are also read out with VLPCs.

The CPS consists of three concentric cylindrical layers of scintillator strips: the inner layer is axial, while the outer two layers are stereo and separated by an angle of $\pm 23°$. Between the solenoid and CPS is a lead plate approximately $1X_0$ thick. The solenoid itself is $0.9X_0$ thick and has uniform radiation length in z.

Each FPS detector consists of two double layers of scintillator strips arranged at an angle of $\pm 23°$. A $2X_0$-thick lead-stainless-steel absorber separates the two layers. The purpose of the inner layer is to detect minimum ionising particles - all charged particles register a minimum ionising hit there. The outer region of the FPS, $1.5 < |\eta| < 1.65$, lies in the shadow of the solenoidal magnet coil which provides up to $3X_0$ of material in front of the FPS. This amount of material readily induces showers that can be detected in the outer scintillator layer.

[1] EM objects refer collectively to electrons, positrons or photons, unless otherwise stated.

2.4.3 Calorimetry

One of the major strengths of DØ's Run I detector was its uranium/liquid argon sampling calorimeter. For Run II, therefore, the basic design has been left unmodified. However, the readout electronics have been replaced in order to cope with the higher bunch crossing rates.

A complete view of the calorimeter is shown in Figure 2.10. It is a hermetic sampling calorimeter divided into three cryostats: one central barrel and two end caps covering the region $|\eta| < 4$. Figure 2.11 reveals a cross-section of the calorimeter in the $y - z$ plane.

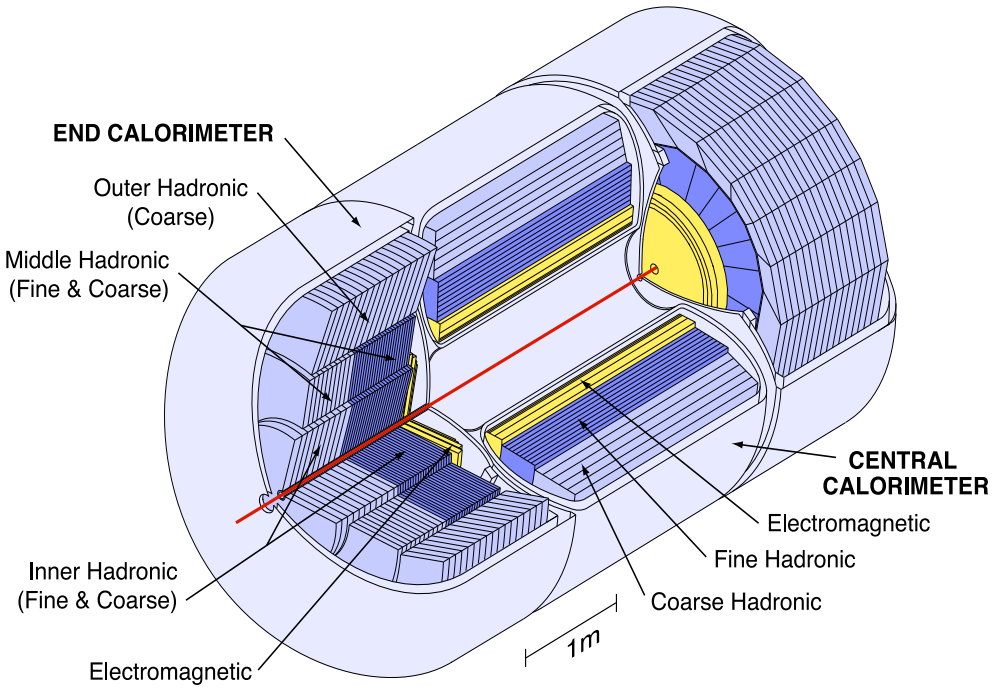

Figure 2.10: Three-dimensional view of the DØ calorimeter.

A basic calorimeter cell consists of metal absorber plates and resistive pads, between which is an intermediate gap filled with liquid argon. The gap remains constant from cell to cell, however, the absorber material employed to induce electromagnetic and hadronic showering varies depending on the cell location within the calorimeter. Several such 'unit' cells are then grouped together to form a read-

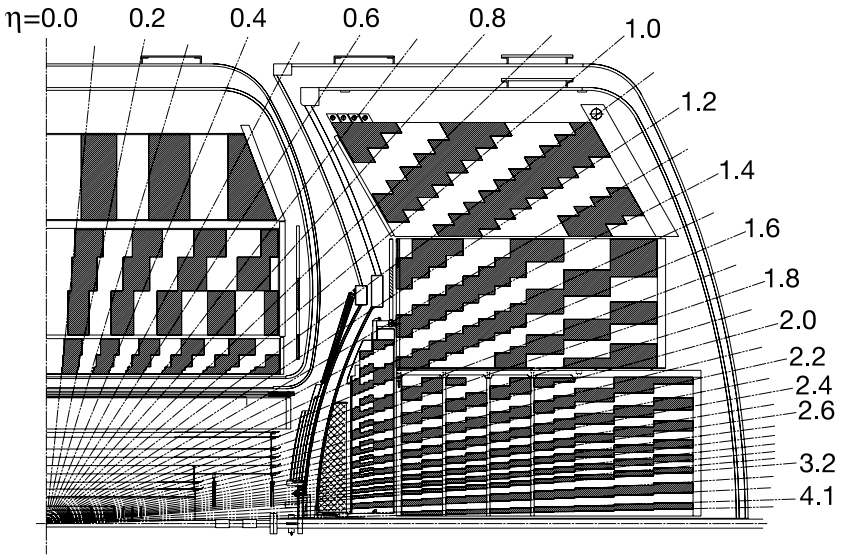

Figure 2.11: Side view of a quadrant of the calorimeter, in the y-z plane. The central barrel and end cap of the calorimeter can be seen in separate cryostats. The labels designate projected values of η.

out module; the number of unit cells per module depends upon the position in the calorimeter (and therefore the precision required). The choice of absorber material is especially important in the inner region of the calorimeter, where photons, electrons and hadrons interact. Depleted uranium is used primarily in the central part of the detector, while stainless steel and copper are installed in the forward regions. Once showering has occurred, the secondary particles within the shower ionise liquid argon atoms located in the gaps between the absorbers. By applying a potential, the ions drift toward the resistive pads and induce a charge which can be detected. Since the liquid argon must be maintained at a temperature of about 80 K, the two end calorimeters and central calorimeter are each enclosed in their own cryostat.

The central calorimeter covers the region $|\eta| \approx 1$ and is divided into three sections corresponding to concentric shells around the beampipe. These are (from innermost to outermost): the electromagnetic (EM), fine hadronic (FH) and coarse hadronic (CH) regions. Each section is further subdivided into layers, which are subsequently broken down into calorimeter cells approximately 0.1×0.1 in $\Delta\eta \times \Delta\phi$. The EM

region consists of four layers and covers approximately twenty radiation lengths, sufficient to contain most electromagnetic showers. The use of uranium here means that the central calorimeter is almost compensating, i.e. responds equally to electromagnetic and hadronic showers; the ratio of the electromagnetic and hadronic response ranges from 1.11 at 10 GeV to 1.04 at 150 GeV [18]. The third layer of the EM section is more finely divided into 0.05×0.05 cells as this is where the EM showers deposit most of their energy.

Surrounding the electromagnetic calorimeter are the hadronic components, which are split into regions with fine and coarse cell depths. Fine segmentation is not as crucial here since hadronic showers are larger than electromagnetic ones. The fine hadronic calorimeter possesses three layers and measures most of the energy deposited by jets of particles created by hadronising partons. The coarse calorimeter has one layer and was designed to measure any energy that has not been absorbed by previous layers. After about 150 electromagnetic radiation lengths, or 8–10 hadronic interaction lengths, the DØ calorimeter is not expected to suffer from significant punch-through.

Intercryostat Detector

The intercryostat detector (ICD) is located in the small gap ($0.7 < |\eta| < 1.4$) between the central and forward calorimeters, as shown in Figure 2.11. In this region there is a significant amount of uninstrumented material such as the cryostat walls, support structures and cabling. The purpose of the ICD is to compensate for the energy lost in this region and provide as accurate an energy measurement as possible, particularly with regard to missing transverse energy. It consists of an array of 384 scintillating tiles of dimensions 0.1×0.1 in $\Delta\eta \times \Delta\phi$ space mounted onto the face of the end cryostats. Scintillation light is collected by wavelength-shifting fibres and carried to phototubes outside the solenoid.

Energy Resolution

The energy resolution provided by the calorimeter has been measured using test beam data [18] and found to be:

$$\begin{aligned} \sigma_E/E &= 15.7\%/\sqrt{E} + 0.3\% \quad (EM) \\ \sigma_E/E &= 41.0\%/\sqrt{E} + 3.2\% \quad (\pi^{\pm}) \end{aligned} \tag{2.3}$$

where the energy E is in GeV.

2.4.4 Detecting Muons

The Run II muon system [33] also builds on the strength of its Run I foundations. The upgraded system offers more extensive geometrical coverage in addition to superior muon triggering, efficient out to $|\eta| < 2.0$. It consists of both a central detector, the Wide Angle Muon System (WAMUS), extending out to $|\eta| < 1.0$ and a forward detector, known as the Forward Muon System (FAMUS), covering $1.0 < |\eta| < 2.0$. A toroidal magnet provides a field of 1.9 Tesla that bends the muon trajectory in the r-z plane and drift tubes are then used to identify the muons. In addition, scintillator counters are also used by the trigger in order to reject sources of background such as cosmic rays.

Wide Angle Muon System

The WAMUS consists of three layers of proportional drift tubes (PDTs), one of which is positioned inside the toroidal magnet (the A layer) and the other two (B and C layers) outside (see Figure 2.6). Each PDT consists of a chamber made from extruded aluminium of rectangular cross-section, split into 24 cells. Each cell is $\approx$ 10.1 cm across with a gold-plated tungsten anode wire running through the centre. The gas filling each chamber is a mixture of argon (84%), methane (8%) and CF_4 (8%), and provides a drift velocity of 10 cm/μs with a maximum drift time

of 500 ns. The spatial uncertainty on each hit due to diffusion is approximately 0.4 mm.

Since the PDT's drift time is longer than the Tevatron's Run II bunch spacing, two extra layers of scintillation counters are used for triggering: one located between the calorimeter and the PDT-A layer and the other found outside the PDT-C layer. There is, however, no coverage in the bottom A-layer as this area is occupied by the calorimeter support structure instead. The scintillation counters offer a time resolution of 1.6 ns.

Forward Muon System

The FAMUS is made up of three layers of drift tubes with A, B and C layers arranged with respect to the toroid as in the WAMUS. Instead of PDTs, the FAMUS employs mini drift tubes (MDTs) which are more radiation hard and therefore better suited to the more highly-irradiated forward region. Each MDT is composed of eight square cells, $\approx$ 1 cm across, made from extruded aluminium combs. The cells have anode wires running through their centre and stainless steel foil on the internal walls as their cathode. In the FAMUS the MDTs contain a 90%-10% CF_4-CH_4 gas mixture which is radiation hard and offers a quick response, with a maximum drift time of 60 ns. Three layers of scintillation counters complete the FAMUS. Although the drift time in the MDTs is considerably shorter than the bunch spacing, the scintillators prove useful for background rejection.

Performance of The Muon Detector

Muon momenta are measured by the muon system to an accuracy of approximately $\Delta p/p = 20(40)\%$ for muons of momentum 10(50) GeV/c. The spatial resolution for a hit registered in either the PDTs or MDTs is about 1 mm.

2.4.5 Triggering

With the increased luminosity and higher interaction rate delivered by the upgraded Tevatron, DØ needed to significantly enhance its ability to select interesting physics events to be recorded. The new trigger system [21] [34] consists of three tiers, with each successive level examining fewer events but in greater detail:

- **Level 1 (L1)** comprises a collection of hardware elements that reduce the event rate from about 1.7 MHz to 2 kHz. This L1 decision must be made 4.2 μs after the beam-beam crossing.

- **Level 2 (L2)** is a combination of hardware and microprocessors associated with different subdetectors. Information from Level 2 is used to form simple "physics objects" and to reduce the rate to about 1 kHz. There is a time window of 100 μs in which to do this.

- **Level 3 (L3)** is purely software-based. Level 3 uses full detector readout and performs partial event reconstruction on a farm of microprocessors within $\sim$100 ms. The output rate is reduced to about 50 Hz and events are recorded for offline reconstruction.

The link between Levels 1, 2 and 3 is illustrated in Figure 2.12. In addition, there is a Level 0 trigger that consists of luminosity monitors mounted symmetrically around the beam pipe, on the inside of the end calorimeters. Its purpose is to trigger on inelastic $p\overline{p}$ collisions.

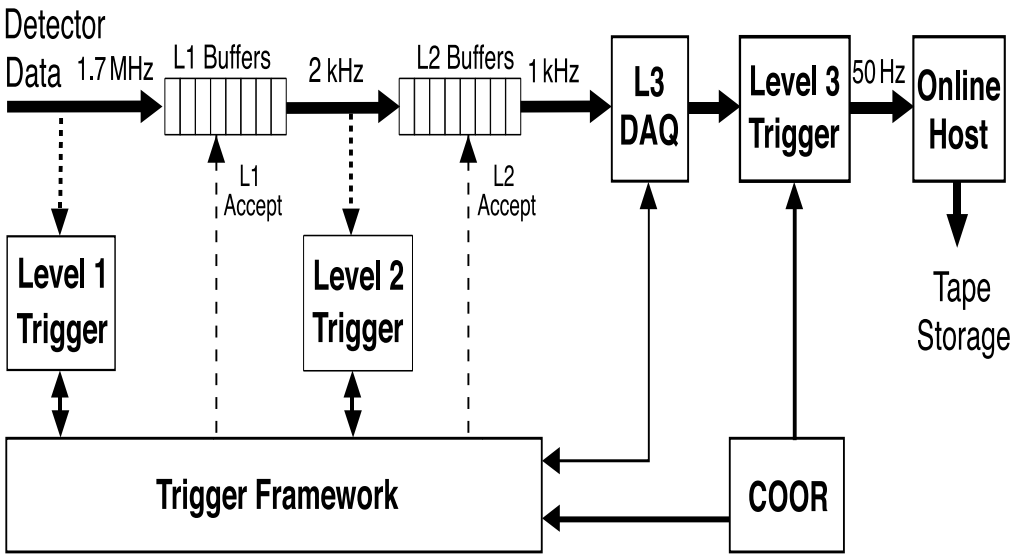

Figure 2.12: Overview of the DØ trigger and data acquisition (DAQ) systems [21]. Overall coordination and control of DØ triggering is controlled by a package known as 'COOR' that runs on the online host machine.

	Accept Rate	**Latency**
Collisions	7.6 MHz	
Level 1	2 kHz	4.2 μs
Level 2	1 kHz	$\sim$100 μs
Level 3	50 Hz	$\sim$100 ms

Table 2.2: Trigger rates for Run II.

Table 2.2 summarises the design specifications for the trigger in Run II at design luminosity. The times for Level 2 and Level 3 trigger decisions vary depending on the event. When all three trigger levels are combined together, the resulting trigger menu contains a wide variety of triggers. While the emphasis lies in triggering on generic lepton and jet final states, trigger "terms" (that is, sets of trigger conditions) also exist for specific physics signatures.

Level 1 And Level 2

The first two levels of the trigger system reduce the event rate such that a full readout of the detector can be performed at L3. In order to achieve this, L1 and

L2 are tightly coupled together through a "trigger framework" that coordinates the trigger decisions and distributes trigger information to the various subdetectors. The trigger framework handles information from the L1 subsystems as well as the L2 trigger system. It forms global L1 and L2 decisions that are sent out to all detector components to coordinate event transfer to L3.

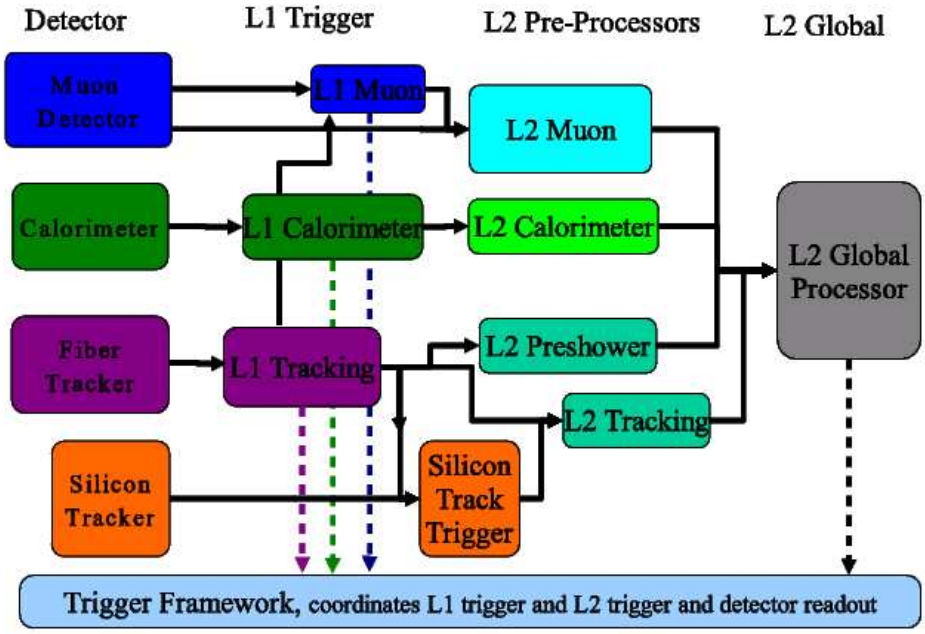

Figure 2.13: Block diagram of the DØ L1 and L2 trigger systems. Horizontal arrows represent the net flow of physics information through the detector. Vertical arrows symbolise the flow of data to the trigger framework, which then makes global L1 and L2 trigger decisions ready to pass to L3.

Figure 2.13 illustrates the L1 and L2 trigger configuration. At L1 individual subdetectors are largely independent, except for the ability to match muons to tracks. At L2, quantities related to each specific part of the detector are reconstructed in distinct preprocessors[2]. The L2 global processor (L2Global) then reads these objects from the preprocessors and combines them to form physics objects such as electrons, jets and muons. In addition, it computes event-wide variables such as

[2]One such preprocessor is the recently commissioned Level 2 silicon track trigger (L2STT), which can trigger on tracks displaced from the primary vertex and is therefore useful for identifying b-tagged events.

the total transverse energy E_T and event correlations such as ϕ separation between objects.

The L1 and L2 trigger systems allow for up to 128 individual triggers to be programmed. Every event that satisfies successive L1 and L2 conditions is fully digitised and sent to the L3 processing farm. Each individual trigger may itself contain several different conditions; all conditions must be fulfilled for the event to pass the trigger. Such a flexible configuration enables trigger menus to be tailored according to the physics needs of the collaboration and to suit the evolving instantaneous luminosities provided by the Tevatron.

L1 can also perform prescaling of triggers that are too copious to pass on without rate reduction. As the luminosity increases, the L1 rate rises and the rejection achieved at L2 and L3 must therefore increase. The precise L1/L2/L3 accept rates vary depending upon the instantaneous luminosity and prescale set.

Level 3

The entire detector is read out for events that pass both L1 and L2. This includes a readout of all individual detector elements as well as the L1 and L2 trigger systems. Each event is reconstructed at L3 using algorithms that are similar to those used in the offline event reconstruction. At L3 the flexibility of the trigger system is expanded further; 256 individual trigger bits are available, each coupled to one of the L1/L2 triggers. Every L3 bit can be programmed to filter on combinations of simple physics objects as well as on global event variables and correlations. L3 also offers the capability of selecting b-tagged jets based on tracking and silicon detector information (see Section 4.2.2 for a more detailed discussion). Ultimately, the final output rate of Level 3 is determined by the size of the L3 processing farm, the speed of the DØ event reconstruction code and the cost of tape.

2.5 Current Detector Performance

Figure 2.14 displays the integrated luminosity collected by DØ so far. Also shown on this plot is the luminosity included in the data sample used within this thesis: approximately 450 pb^{-1} recorded from June 2002 to August 2004. Since the start of Run II, a total of 1.4 fb^{-1} have been delivered by the Tevatron, of which DØ has recorded 1.2 fb^{-1}. Figure 2.15 shows the efficiency with which DØ takes data. The detector has been running at 87% efficiency (a weekly average) for much of Run II.

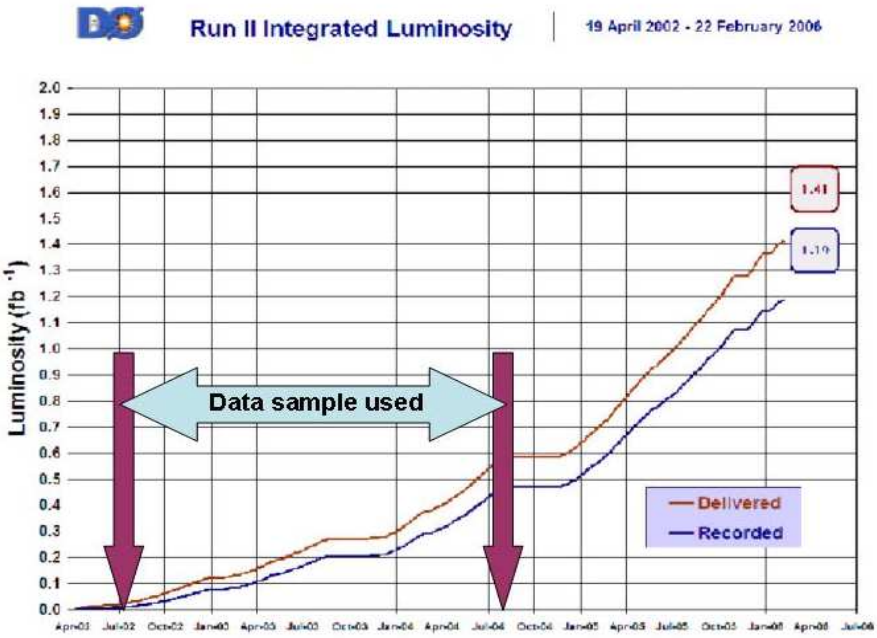

Figure 2.14: Integrated luminosity collected by the DØ experiment up to 22 February 2006, when the latest accelerator shutdown began [35].

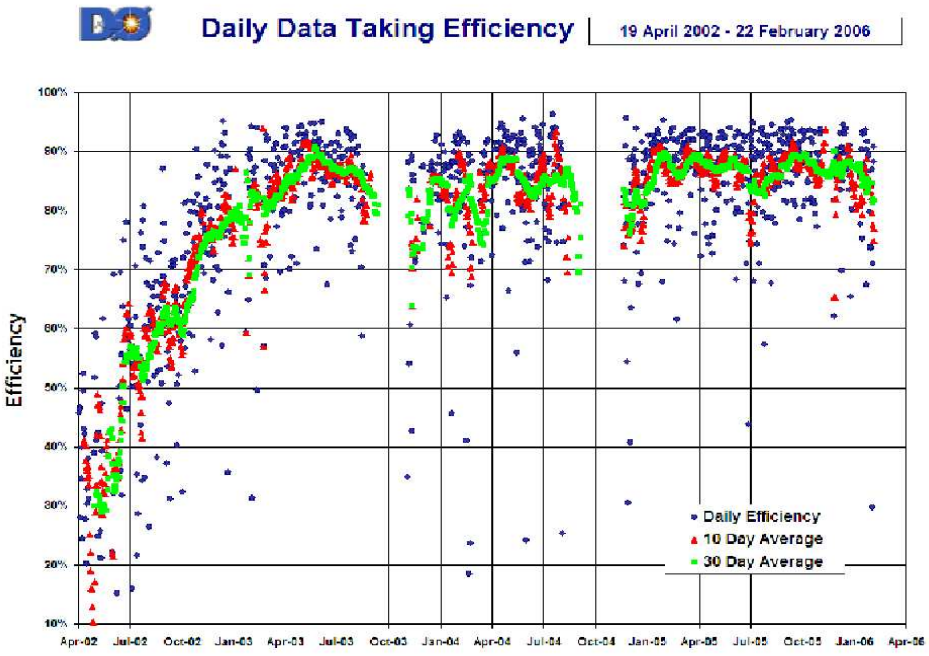

Figure 2.15: DØ's daily data-taking efficiency up to 22 February 2006, when the latest accelerator shutdown began [36].

Chapter 3

Resolving Power

"How can I know what I think till I see what I say?"

E. M. Forster

3.1 Overview

As discussed in Chapter 1, a low mass Higgs decays predominantly into a $b\overline{b}$ quark-antiquark pair. Reconstructing the original Higgs boson with confidence requires accurate knowledge of the daughter b-quark energies to be derived from the relatively 'messy' b-quark jets recorded in the detector that are hard to isolate. The Higgs signal will be swamped by a large continuum of QCD background events and so to extract a signal with as small a dataset as possible, the di-b-jet mass resolution must be as precise as possible. In this chapter, two Higgs (or Higgs-like) decay channels - $ZH \rightarrow e^+e^-b\overline{b}$ and $Z \rightarrow b\overline{b}$ - are used to study the b-jet energy resolution and di-b-jet mass resolution that could be achieved at DØ, with the ultimate aim of accurately identifying potential Higgs boson candidates.

3.2 Jet Formation

During proton-antiproton hard scattering, a parton (quark or gluon) from the proton interacts with a parton from the antiproton. At interaction, the two partons

behave as free particles due to asymptotic freedom. As the partons move away from the interaction point in opposite directions, confinement starts to occur and the QCD force between them grows rapidly, opposing their increasing separation. Consequently, the partons' kinetic energy is converted into potential energy; the potential energy increases until it is sufficient to create a new pair of partons, which also try to move apart. This process, known as fragmentation, continues until all energy exchanged at the original hard scattering is converted into new parton pairs. Each initial outgoing parton is surrounded by a cloud of other partons, forming a "parton jet".

Next, hadronisation occurs: the partons produced during fragmentation recombine to form colourless hadrons. This results in two streams of particles. Each 'stream' is composed of particles moving almost unidirectionally and with little relative transverse momentum with respect to the stream. This is a "particle jet", and may also consist of photons and leptons.

Finally, particle jets enter the calorimeter and undergo electromagnetic and hadronic interactions with the detector. Such processes continue until all the initial energy (mass and kinetic) of the particle jets is deposited in the calorimeter. These energies are the ones actually measured, and from these a "calorimeter jet" is reconstructed using a jet algorithm. The aim of such algorithms is to combine clusters of 'particles' (i.e. calorimeter cells or hadrons at the experimental level) into jets, such that the kinematic properties of the jets (e.g. momenta) can be linked to the properties of the partons involved in the hard scattering event. Effectively the jet algorithm allows us to "see" the partons (or at least their fingerprints) in the hadronic final state.

Table 3.1 summarises the various physical stages of jet formation.

Hard scattering	$\Longrightarrow$	Outgoing partons
Fragmentation	$\Longrightarrow$	Parton jet
Hadronisation	$\Longrightarrow$	Particle jet
Interaction with the detector	$\Longrightarrow$	Calorimeter jet

Table 3.1: The successive stages of jet formation, from the hard scattering event to energy deposition in the calorimeter.

3.2.1 Gluon Radiation

The quarks inside the parent proton or antiproton may radiate gluons before and after the hard scattering event. When radiation occurs before the hard interaction takes place, this is known as initial state radiation (ISR). In final state radiation (FSR), the outgoing partons radiate gluons after the hard scattering. Here, only the effect of FSR is studied.

Gluon radiation from b quarks can be represented by the following process:

$$b \rightarrow b' + g, \tag{3.1}$$

where b is the parton before gluon radiation, b' is the parton after radiation and g is the gluon emitted. The radiated gluon can be hard or soft. If it is hard, then b' and g are emitted in very different directions. They appear at the jet level as two distinct jets. However, if the gluon is soft, b' and g are almost unidirectional and in the resulting b-jet the gluon and quark jets may overlap.

3.3 Data Samples

In these investigations two Monte Carlo (MC) samples were studied:

- $\boldsymbol{Z \rightarrow b\overline{b}}$

  10,000 $Z \rightarrow b\overline{b}$ events were generated using `PYTHIA` [37] (version 6.202), with both initial and final state radiation. Signal events were overlaid with an average of 0.5 minimum bias events. They were then passed through the DØ `GEANT`

detector simulation [38], which models the calorimeter response and resolution. A 'plate detector' geometry[1] was employed within the GEANT simulation; this provides the most faithful representation of electromagnetic showers in the detector. The digitised data were then passed through version p10 of the DØ Run II reconstruction package [39].

- $\boldsymbol{ZH \rightarrow e^+e^-b\overline{b}}$

  10,000 $ZH \rightarrow e^+e^-b\overline{b}$ events were generated using PYTHIA as above, selecting a Higgs mass of 115 GeV/c^2. The Higgs decays to a $b\overline{b}$ pair while the Z decays leptonically. As above, an average of 0.5 minimum bias events were overlaid, a plate geometry and version p10 of the Run II reconstruction software were used.

For both channels, the $b\overline{b}$ events were allowed to decay generically and were not forced to undergo semileptonic decays.

3.4 Analysis Algorithm

An offline analysis tool (ROOT [40], version 3.03_09) was used to develop an algorithm in order to determine the jet energy and mass resolutions in the two samples.

3.4.1 Event Selection

For each event, b and $\overline{b}$ quarks were identified. In events without hard FSR, this simply involved the b and $\overline{b}$ quarks coming from the parent Higgs or Z. If hard FSR occurred, we identified not only the b-quarks from the parent boson, but also the daughter b' quark and radiated gluon originating from the b that had undergone FSR. Jet formation algorithms were implemented at the parton, particle and calorimeter levels, which allowed the effects of hadronisation, gluon radiation and energy measurement in the calorimeter to be studied in detail. Two alternative jet algorithms were explored:

[1] In such a geometry each scintillator plate is individually coupled to a photomultiplier tube.

- **Cone Algorithm**: Historically, hadron-hadron experiments have adopted the cone algorithm [41] for reconstructing jets detected inside their calorimeters. The basic idea is to define a jet as a set of particles that can be contained in a cone in $\eta - \phi$ space. The chosen cone size, R, typically ranges from 0.4 to 0.7; in this study cones of radii 0.5 and 0.7 are investigated. Firstly the most energetic particles in the event - so-called "seeds" - are identified; at DØ, all seeds are required to exceed an energy threshold of 1 GeV. Next, cones centred about these seeds are formed and seeds are iteratively clustered into the cone until there is a collection of 'stable' seeds that contain most of the energy in their cones and whose axes coincide with the jet direction. These stable cones define the jet content of an event.

  This strategy does not prevent the final stable cones from overlapping; a single particle may belong to more than one cone. In order to remedy this a 'split-merge' procedure is incorporated into the algorithm, which specifies how to split or merge overlapping cones.

- **k_T Algorithm**: An alternative approach is offered by the k_T algorithm [42] [43]. This method successively merges pairs of 'particles' in order of increasing relative transverse momentum to form k_T jets. By analogy with the cone radius R, there is a size parameter, D, that controls the termination of merging and characterises the size of the resulting jets; here, jets with D values of 0.4 and 1.0 have been studied. Since the k_T algorithm fundamentally merges nearby particles, there is a close correspondence between jets reconstructed in the calorimeter and those reconstructed from individual hadrons, photons and leptons. Moreover, every particle in an event is assigned to a unique jet.

For both jet algorithms considered, calorimeter jets were isolated from electrons in order to obtain true hadronic clusters. In addition, standard DØ quality cuts were imposed upon the calorimeter jets to select 'good' quality jets and reject fake ones:

- $0.1 < EMF < 0.85$. EMF is the fraction of energy in the jet coming from the electromagnetic calorimeter.

- $CHF < 0.4$. CHF is the fraction of jet energy in the coarse hadronic part of the calorimeter.

- $HotF < 10$. Hot cells are single cells in the calorimeter that contain a large amount of unattributed energy. $HotF$ is defined as the ratio of the transverse energy in the hottest cell to that in the second hottest cell (within the jet).

- $n90 > 1$. $n90$ is the number of calorimeter cells containing 90% of the jet energy; if $n90$ is 1 then the jet is likely to consist of a single hot cell.

- $|\eta_{jet}| < 2.5$. This cut on the pseudorapidity selects central jets whose energies are well measured.

In most of the studies described here, no jet p_T cut was applied and no constraints were imposed upon the number of jets in each event. Even without an explicit jet p_T cut, however, there is an implicit DØ jet reconstruction threshold that rejects all jets with $E_T < 8$ GeV (before any jet energy corrections have been applied). In Sections 3.7.3 and 3.7.4 respectively, the jet p_T cut and jet multiplicity were varied and their effect on mass resolution was measured. The event selection involved no cuts at the particle-jet level and no cuts on the primary vertex.

3.4.2 Spatial Matching

b-jets were identified at the particle and calorimeter levels by spatially matching the jets to b-partons in $\eta - \phi$ space. As mentioned in Section 2.4.1, the distance between objects in $\eta - \phi$ space is given by the 'cone' distance $dR = \sqrt{(\Delta\phi)^2 + (\Delta\eta)^2}$ and spatial matching conditions can be imposed by placing cuts on dR. In this analysis, three stages of matching were performed:

(i) **Calorimeter-Particle**

- For every 'good' calorimeter jet (i.e. one that passes the quality cuts listed in Section 3.4.1), the closest particle jet within a cone radius (dR) of 0.2 was found.

(ii) **Calorimeter-Parton**

- For every b and $\overline{b}$ parton, the closest good calorimeter jet within a radius of 0.2 was selected;
- For every b and $\overline{b}$ parton that underwent hard FSR (i.e. omitted a gluon with a p_T of at least 1.9 GeV/c, to form a b' and $\overline{b'}$ parton), the closest good calorimeter jet within a radius of 0.2 was selected.

(iii) **Particle-Parton**

- For every b and $\overline{b}$ parton, the closest particle jet within a distance of 0.2 was identified;
- In the case of hard FSR, for every b' and $\overline{b'}$ parton the closest particle jet within a distance of 0.2 was identified.

In practice, one cannot distinguish between a jet whose parent b quark underwent soft gluon radiation and one whose parent b underwent no radiation. This is because a soft gluon has insufficient energy to significantly change the direction of the parent parton. Hence matching to b or $\overline{b}$ can include no radiation or soft radiation, while matching to b' or $\overline{b'}$ incorporates emission of hard gluons as well (hard gluons are defined in the MC as those with a p_T greater than 2 GeV). Hence the explicit use of the term 'hard FSR'.

At each level of matching, checks were made to prevent double counting of a matched jet within an event.

3.4.3 Computing The *b*-jet Energy Resolution

The fractional b-jet resolution was calculated at three different stages, both including and excluding the effects of hard FSR: calorimeter-parton, calorimeter-particle and particle-parton (defined below). For each measure of resolution tight spatial matching was required, as described in Section 3.4.2.

(i) **Calorimeter-Particle Resolution** - calculated w.r.t the particle jet ('pjet' indicates particle jet):

- Excluding hard FSR:

$$\frac{p_T^{\text{cjet matched to } b} - p_T^{\text{pjet matched to } b}}{p_T^{\text{pjet matched to } b}}; \tag{3.2}$$

- Including hard FSR:

$$\frac{p_T^{\text{cjet matched to } b'} - p_T^{\text{pjet matched to } b'}}{p_T^{\text{pjet matched to } b'}}. \tag{3.3}$$

(ii) **Calorimeter-Parton Resolution** - calculated w.r.t the b parton before hard FSR ('cjet' designates a calorimeter jet):

- Excluding hard FSR:

$$\frac{p_T^{\text{cjet matched to } b} - p_T^{b}}{p_T^{b}}; \tag{3.4}$$

- Including hard FSR:

$$\frac{p_T^{\text{cjet matched to } b'} - p_T^{b}}{p_T^{b}}. \tag{3.5}$$

($p_T^{\text{cjet matched to } b'}$ is used in the numerators of equations 3.3 and 3.5 because this reflects the physical quantity measured in real data.)

(iii) **Particle-Parton Resolution** - calculated w.r.t the b parton before hard FSR:

- Excluding hard FSR:

$$\frac{p_T^{\text{pjet matched to } b} - p_T^{b}}{p_T^{b}}; \tag{3.6}$$

- Including hard FSR:

$$\frac{p_T^{\text{pjet matched to } b'} - p_T^b}{p_T^b}. \tag{3.7}$$

The fractional b-jet resolution is given by the width of each p_T resolution distribution described by equations 3.2 to 3.7. In most cases this width was obtained by performing a Gaussian fit and taking the fitted σ. Each p_T resolution distribution was plotted for five parton and five calorimeter jet p_T bins, allowing the fractional jet resolution to be measured as a function of either parton or jet p_T. It is useful to calculate the resolution relative to both the jet energy scale (that is recorded in the detector) and the parton energy scale (the ideal limit of our measurements).

3.4.4 Evaluating The $b\overline{b}$ Mass Resolution

The Higgs and Z-boson invariant masses were reconstructed at three levels (parton, particle and calorimeter) using b-partons and b-jets identified via spatial matching as described in Section 3.4.2. In order to calculate each invariant mass, all three levels of spatial matching with $dR < 0.2$ were required. Masses were reconstructed without hard FSR (using matching to b, $\overline{b}$) and with hard FSR (using matching to b', $\overline{b'}$).

(i) **Diparton Mass**

- Reconstructed using the b and $\overline{b}$ partons from the parent Higgs or Z;
- When hard FSR occurred, b' and $\overline{b'}$ partons were used.

(ii) **Particle Dijet Mass**

- Reconstructed using the particle jets that originated from the b and $\overline{b}$ partons;
- When hard FSR occurred, b'-particle-level jets were used.

(iii) **Calorimeter Dijet Mass**

- Reconstructed using the calorimeter jets that originated from the b and $\overline{b}$ partons;

- When hard FSR occurred, b'-calorimeter-level jets were used.

Fractional mass resolutions were calculated using the $\frac{\text{RMS}}{\text{Mean}}$ from each distribution (see Section 3.7.1 for further details).

3.4.5 The Jet Energy Scale

Following a beam-beam collision, the total energy of all the particles that enter the detector is greater than the energy of the resulting jets measured in the calorimeter. This mismeasurement is due to detector effects such as calorimeter noise and a non-uniform response to the energy deposited. In addition, it is possible that some of the shower falls outside the jet cone and hence energy is 'lost'.

In order to correct the calorimeter jet energies back to the particle level, a jet energy scale (JES) correction [44] is applied[2]. This correction is also used to correct the missing energy measured within the calorimeter and the energy of simulated jets in MC events.

For a generic jet, the particle level or 'true' jet energy ($E_{\text{jet}}^{\text{particle}}$) can be obtained from the measured calorimeter jet energy ($E_{\text{jet}}^{\text{measured}}$) using the following relation:

$$E_{\text{jet}}^{\text{particle}} = \frac{E_{\text{jet}}^{\text{measured}} - E_0}{R_{\text{jet}} \cdot S} = C_{\text{JES}} \cdot E_{\text{jet}}^{\text{measured}}. \tag{3.8}$$

Here:

- E_0 is the offset energy, which represents energy not associated with the hard scattering. The offset arises from detector noise (electronic and uranium), pile-up energy from previous bunch crossings and any extra energy that comes

[2]Currently no correction is available for k_T jets.

from additional $p\overline{p}$ interactions or the underlying physics event. The size of the offset energy ranges from 2 to 6 GeV for the central part of the detector, depending on the number of multiple interactions within the event. The error on this correction is about 10

- R_{jet} describes the calorimeter response to the hadronic jet. It depends on the energy, pseudorapidity and size of the jets. The response correction is, at about 30 ± 2% (for a 0.7 cone jet of energy 50 GeV), the largest of the jet energy scale corrections.

- S is a term that accounts for out-of-cone showering effects due to the detector; it represents the fraction of particle jet energy that is deposited inside the jet algorithm cone. Some particles produced inside (outside) the cone deposit a fraction of their energy outside (inside) the cone as the shower develops in the calorimeter. Moreover, particles originally emitted inside (outside) the cone can be bent outside (inside) by the magnetic field. For an 0.5 cone jet of (corrected) energy 50 GeV, the showering correction is approximately 1.01 ± 0.01.

- C_{JES} is the overall multiplicative correction factor (greater than unity) that incorporates the various jet energy corrections. It is applied to all calorimeter level jets and is parametrised in terms of jet energy and $|\eta|$.

Most of the corrections are derived using the conservation of transverse momentum in data, and separate corrections for data and MC are formulated. They are incorporated into a DØ jet correction software package known as jetcorr [45].

For a central, 0.5 cone jet of energy 50 GeV, the average correction factor to its energy is 1.3 ± 0.03. The main contribution to the total uncertainty comes from our imprecise knowledge of the response, especially at low and high jet transverse energies. In addition, showering-related uncertainties are larger at high energy, again

due to limited statistics. Improvements in all of these areas are expected in the next round of measurement of the jet energy scale.

b-jets have different characteristics from generic jets - they undergo harder fragmentation and semileptonic decays. As such, an additional contribution is needed to correct the energy of the b-jets back to that of the parent b-quark. The jetcorr package is therefore made up of two components:

- **Basic Correction**: corrects for response, offset and out-of-cone showering. This is applied to all jets.
- **Muon Correction**: compensates for the semileptonic decay of b-jets (into muons) by correcting for the muon momentum and adjusting for the unobserved neutrino. The muon correction is only applied to b-jets when there is an identified muon within the jet. The algorithm corrects the jet energy for both the energy of the muon and the energy of the neutrino (which depends on the muon energy and the muon's transverse momentum relative to the jet axis).

In this study jet energy corrections were applied to all calorimeter cone jets using version 2.2 of jetcorr.

3.5 b-partons And b-jets

Figure 3.1 displays energy, p_T and pseudorapidity distributions for b-partons and b-jets, from both the Higgs and Z decays. Hard FSR is excluded; all jets are 0.5 cone calorimeter-level and energy-scale corrected. Table 3.2 summarises the mean energy and p_T values obtained.

Average Energy (GeV)	**Higgs**	$\boldsymbol{Z}$
b-partons	83.5	69.6
b-jets	78.1	58.7
Average $\boldsymbol{p_T}$ (GeV/c)	**Higgs**	$\boldsymbol{Z}$
b-partons	58.4	35.1
b-jets	57.4	31.8

Table 3.2: Comparison of mean energy and p_T of b-partons and b-jets from Higgs and Z decay. All b-jet quantities shown are energy-scale corrected.

There is significantly more energy in the $ZH \rightarrow e^+e^-b\overline{b}$ system than in $Z \rightarrow b\overline{b}$. As can be seen from Table 3.2, the b-partons from the Higgs have on average 14 GeV more energy than those coming from the Z, thanks to the higher Higgs mass as compared to the Z mass.

The topologies of the two decays are also rather different. Jets and partons are more centrally distributed in $ZH \rightarrow e^+e^-b\overline{b}$ than in $Z \rightarrow b\overline{b}$, as can be seen from the pseudorapidity distributions shown in Figure 3.1. The cut-off at an $|\eta|$ value of 2.5 corresponds to the cut imposed upon all calorimeter jets as described in Section 3.4.1.

Since there is more energy in the $ZH \rightarrow e^+e^-b\overline{b}$ system and the partons and jets from the Higgs are more central, the b-quarks are produced with significantly higher p_T in $ZH \rightarrow e^+e^-b\overline{b}$ than in $Z \rightarrow b\overline{b}$ (as demonstrated in Table 3.2). b-quarks from the Higgs boson have a transverse momentum that is on average 23 GeV/c higher than those originating from the Z. Figure 3.1 also reveals a cut-off in the b-jet p_T spectrum at 8 GeV/c, which corresponds to the jet reconstruction threshold.

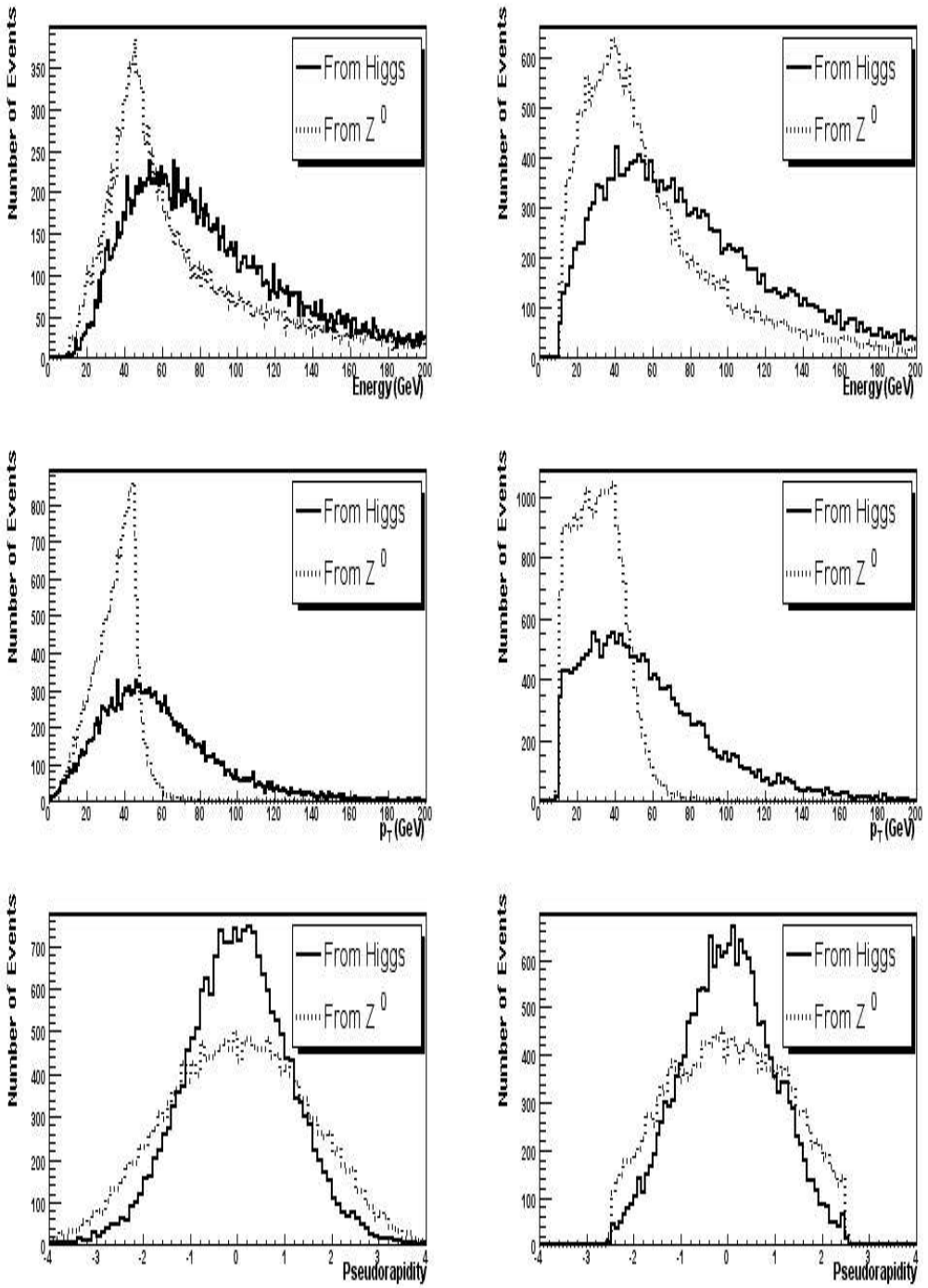

Figure 3.1: Comparison of Higgs and Z b-parton and b-jet spectra. Left: b-parton distributions. Right: b-jet distributions. The variables plotted are energy (top), transverse energy (middle) and pseudorapidity (bottom). All jets are 0.5 cone, calorimeter-level and jet energy corrected.

3.6 b-jet Energy Resolution

3.6.1 At The Three Levels

Figure 3.2 compares the b-jet resolution obtained at the calorimeter-parton, calorimeter-particle and particle-parton levels, as a function of both jet p_T and parton p_T. These results are for 0.5 cone jets in $ZH \rightarrow e^+e^-b\overline{b}$; no jet p_T cuts or jet multiplicity constraints were imposed. Full jet energy scale corrections were applied at the calorimeter level and the effects of hard gluon radiation were excluded by requiring spatial matching to b-partons before hard FSR. Each resolution was taken to be the width of a Gaussian fitted to the fractional p_T resolution distribution (as described in Section 3.4.3). The errors bars shown in Figure 3.2 come from the Gaussian fits.

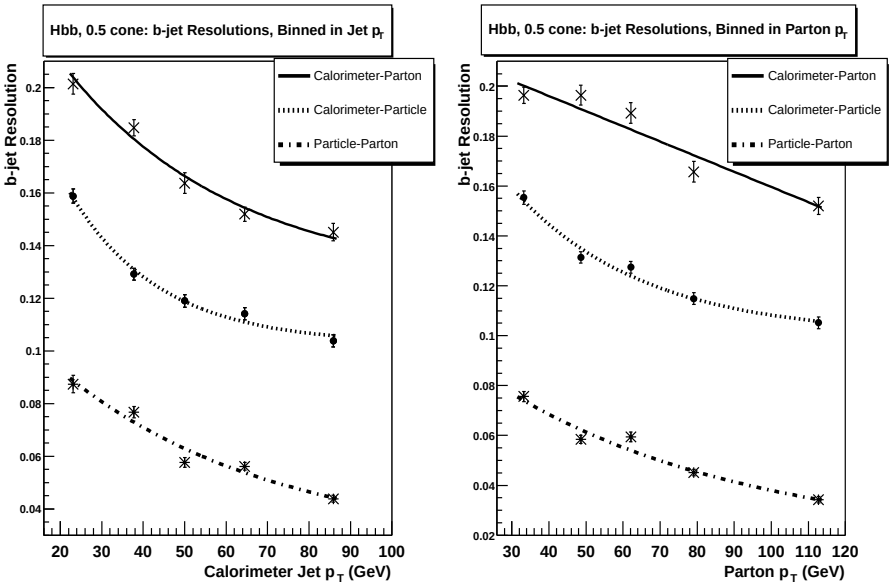

Figure 3.2: b-jet resolution as a function of p_T for $ZH \rightarrow e^+e^-b\overline{b}$, without hard FSR. The lines shown are there to guide the eye, however they are fits to the data obtained using a fit form given by equation 3.9. The fit is performed for all three lines on each graph even though equation 3.9 contains noise terms that don't apply to the particle-parton case. Resolution is binned in calorimeter jet p_T before hard FSR (left) and b parton p_T before hard FSR (right). All calorimeter jets are fully corrected.

Table 3.3 provides the jet energy resolution at each level of resolution at a p_T of 50 GeV/c; the errors on these resolutions have been measured to be $\pm 0.1\%$. The

particle-parton resolution (bottom line of Table 3.3) is determined by the physical processes of fragmentation and hadronisation. Calorimeter-particle resolution (middle line) is related to detector effects. Finally, the calorimeter-parton effect (top line) is a combination of the previous two effects. Ideally the three resolutions given in Table 3.3 should add in quadrature; in practice, however, they don't. This could be attributed to imperfect measurements in the jet energy scale, imperfect MC modelling (of, for example, the jet formation processes) or correlations between the three levels of resolution.

Level of Resolution	***b*-jet Resolution (%)**	
	Binned in Jet p_T	**Binned in Parton p_T**
Calorimeter-Parton	16.8	19.0
Calorimeter-Particle	12.0	13.5
Particle-Parton	6.3	6.2

Table 3.3: Fractional b-jet resolution at 50 GeV/c obtained at the calorimeter-parton, calorimeter-particle and particle-parton levels in $ZH \rightarrow e^+e^-b\bar{b}$ (0.5 cone, energy scale corrected jets, no hard FSR).

The jet energy resolution can be parametrised in the following way:

$$\frac{\sigma_E}{E} = \frac{N}{E} \oplus \frac{S}{\sqrt{E}} \oplus C. \tag{3.9}$$

Here N is a noise term which represents the energy smearing caused by the noise of the readout electronics and by uranium decay in the calorimeter. S is the smearing due to fluctuations in energy sampling and C is a constant term representing the calorimeter calibration error. From Figure 3.2 it can be seen that at any given level, jet energy resolution improves with increasing energy, as one would expect. The more energy there is, the smaller the fractional uncertainty in the energy measurement. For low energy jets the resolution is dominated by the stochastic term while at high energies it is dominated by the constant term.

3.6.2 Effect of The Jet Algorithm on b-jet Resolution

The choice of jet algorithm has an impact on the b-jet energy resolution, as demonstrated in Figure 3.3 for the $ZH \rightarrow e^+e^-b\bar{b}$ channel. This effect was explored at the calorimeter-parton level, both including and excluding the effects of hard FSR. No jet corrections were applied as none currently exist for k_T jets.

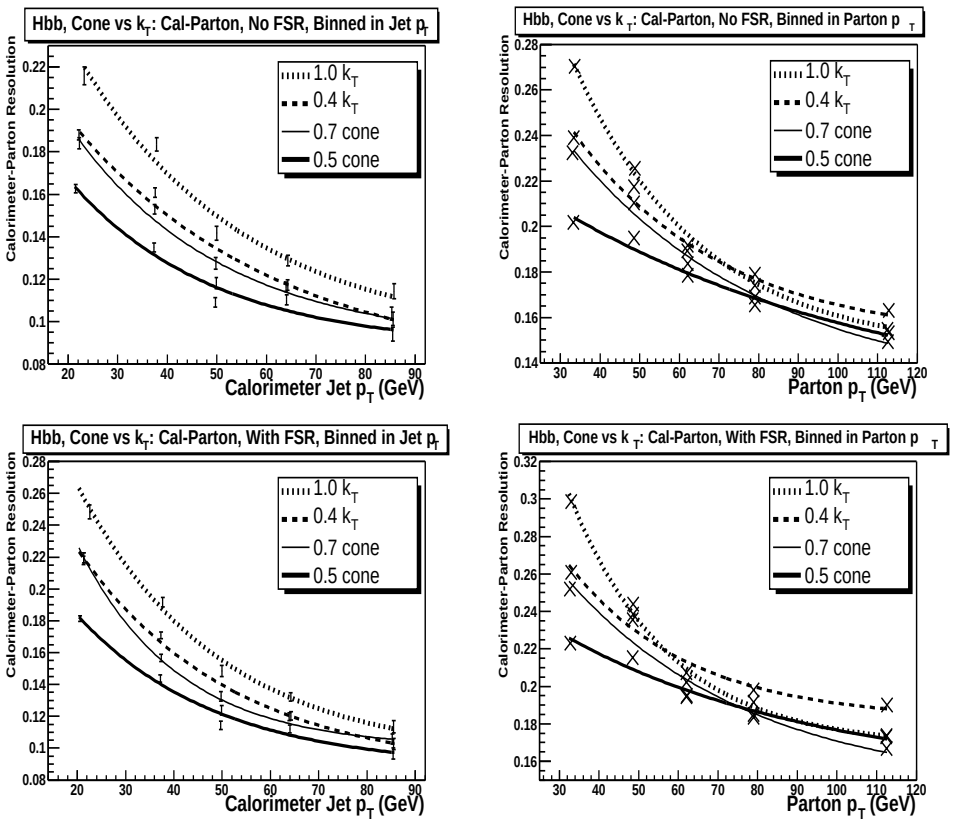

Figure 3.3: The effect of the jet algorithm on the b-jet resolution in $ZH \rightarrow e^+e^-b\bar{b}$. Comparisons were made at the calorimeter-parton level using uncorrected jets. Upper plots exclude hard FSR, lower ones include hard FSR. Binned in calorimeter jet p_T matched to partons (left) and in parton p_T before hard FSR (right).

When binned in jet p_T (left-hand plots), the jet resolution was calculated using Gaussian widths. The errors displayed are statistical. When binned in parton p_T (right-hand graphs) the resolution was measured using RMS values; in this case errors were determined by rebinning the distributions and measuring the effect on the RMS and found to be $\pm 0.5\%$. The motivation for using RMS values comes from

the fact that when binning in parton p_T, a larger tail is observed at low p_T - the result of radiation and fragmentation/hadronisation processes. A Gaussian fit is therefore less appropriate than using the RMS which takes into account the spread of the distribution due to the tails.

The DØ Run II jet cone algorithm provides better resolution than the k_T algorithm, implying that the k_T algorithm picks up more noise in a hadronic environment. In addition, 0.5 cone jets are better than 0.7 cone jets. In the low p_T regime where noise is dominant small jets have better resolution than large jets because larger jets contain more noise. As the jet energy increases the noise becomes less significant (as can be seen from Equation 3.9) and the difference in resolution between large and small jets decreases.

Binning in parton p_T (right-hand plots of Figure 3.3) illustrates the effects of hard FSR more clearly. As parton p_T increases, more (hard and soft) gluon radiation occurs, thus the amount of energy in each b-jet decreases regardless of jet size. At high p_T noise no longer dominates, therefore large jets are able to cluster in more of the available energy than small jets. In this case the larger jets ($R = 0.7$ cone, $D = 1.0$ k_T) provide superior resolution.

3.6.3 Effect of Final State Radiation on b-jet Resolution

The effect of hard gluon radiation on the b-jet resolution is shown in Figures 3.4 to 3.6 for 0.5 cone, fully-corrected jets in $ZH \rightarrow e^+e^-b\overline{b}$. RMS values were used to measure the jet resolution so as to fully include the effect of the FSR tail. Each measure of resolution was binned in parton p_T before hard FSR.

Table 3.4 presents the fractional effect at each level, at 50 GeV/c. The fractional effect is approximately 10% at the calorimeter-parton and particle-parton levels; FSR is a parton process and therefore it affects these parton-related jet energy resolutions. At the calorimeter-particle (detector) level the effect of FSR is very small since the calorimetric resolution, which is mainly a function of the energy deposited in the detector, is an instrumental effect.

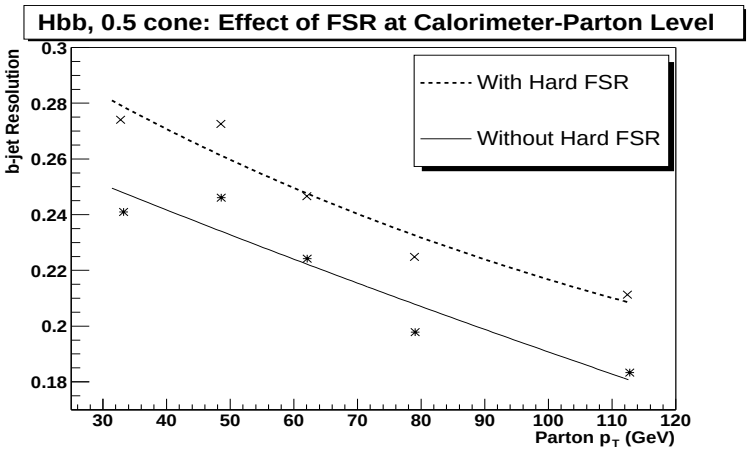

Figure 3.4: Effect of hard FSR on the b-jet resolution in $ZH \rightarrow e^+e^-b\overline{b}$ at the calorimeter-parton level.

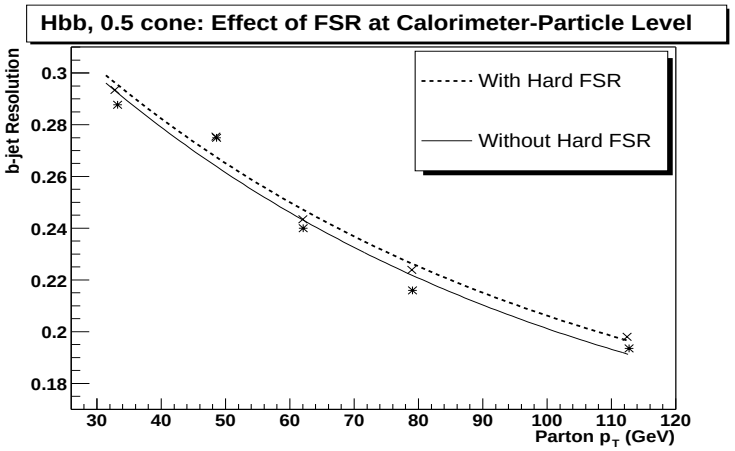

Figure 3.5: Effect of hard FSR on the b-jet resolution in $ZH \rightarrow e^+e^-b\overline{b}$ at the calorimeter-particle level.

3.6.4 Comparison of Z And Higgs b-jet Resolutions

Direct comparisons were made between the jet energy resolution attainable in $Z \rightarrow b\overline{b}$ and $ZH \rightarrow e^+e^-b\overline{b}$, for 0.5 cone energy-scale corrected jets. The resolution was binned in parton p_T before hard FSR. As Figure 3.7 shows (using the calorimeter-particle level as an example), for a given parton p_T the b-jet resolution is the same for the Z and Higgs resonances, within errors. The same effect is seen if hard FSR is included in the measurement. These observations can be explained by the fact that the jet energy resolution at the calorimeter-particle level depends upon the input

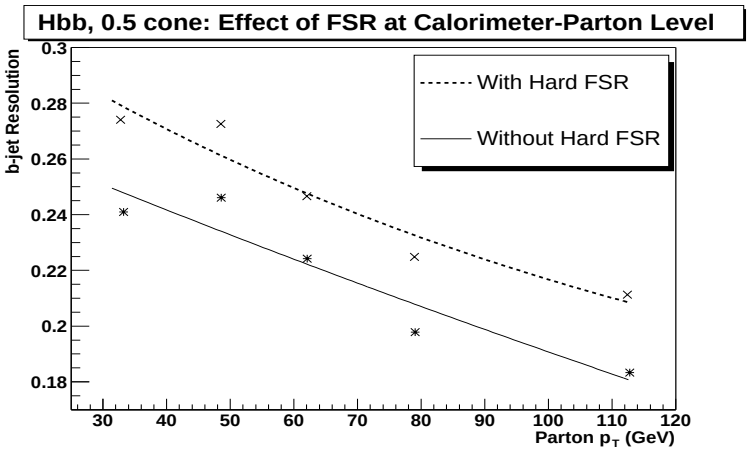

Figure 3.6: Effect of hard FSR on b-jet resolution in $ZH \to e^+e^-b\overline{b}$ at the particle-parton level.

Level of Resolution	Fractional Hard FSR Effect (%)
Calorimeter-Parton	11
Calorimeter-Particle	2
Particle-Parton	11

Table 3.4: The fractional effect of hard FSR on b-jet resolution at 50 GeV/c for $ZH \to e^+e^-b\overline{b}$.

energy into the detector regardless of whether that energy originates from the Z or the Higgs.

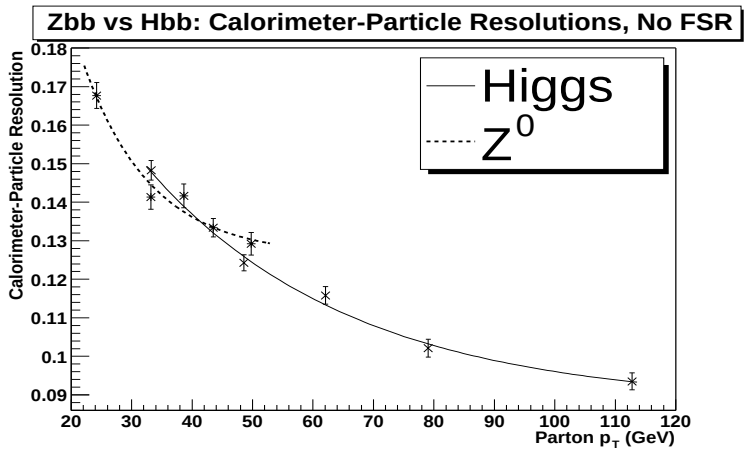

Figure 3.7: Comparison of Z and Higgs b-jet resolutions at calorimeter-particle level, excluding hard FSR. 0.5 cone corrected jets were used. Gaussian widths are plotted; error bars are statistical.

3.7 $b\bar{b}$ Mass Resolution

3.7.1 At The Three Levels

The dijet mass of two jets with energies E_1 and E_2 and azimuthal angles θ_1 and θ_2 can be approximated by

$$M_{jj} \approx \sqrt{(2E_1E_2(1+\cos(\theta_1+\theta_2))}. \tag{3.10}$$

Ignoring the angular resolution, we can then express the fractional mass reolution in terms of the individual jet energy resolutions:

$$\left(\frac{\Delta M_{jj}}{M_{jj}}\right)^2 = \frac{1}{2}\left(\left(\frac{\Delta E_1}{E_1}\right)^2 + \left(\frac{\Delta E_2}{E_2}\right)^2\right). \tag{3.11}$$

The Higgs and Z masses were reconstructed at the parton, particle- and calorimeter-jet levels. Figure 3.8 shows the resulting distributions for the Higgs (see Appendix A for the corresponding Z mass plots). The dashed profiles superimposed on the plots represent Gaussian fits to the central symmetric portion of the peak of each distribution. These fits were determined in the following way: For each mass distribution, the peak position was measured (let us call this m_{peak} GeV/c^2). Next, a suitable central, symmetric part of the peak was chosen for further fitting. The lower boundary of this central region was chosen by eye to be the mass below which the left-hand tail of the distribution began; let us call this x GeV/c^2 below m_{peak}. Finally, the mass distribution was fitted with a Gaussian over the range $m_{peak} \pm x$ GeV/c^2. Calorimeter-level distributions are not jet energy scale corrected at this point.

Diparton Mass

Without hard gluon radiation (top left pane of Figure 3.8), the Higgs mass is reconstructed perfectly at the parton level. Within the `PYTHIA` simulation the Higgs is assigned a zero width, which accounts for the zero spread seen in this distribution. As can be seen in the top right plot, inclusion of hard FSR introduces a broad low

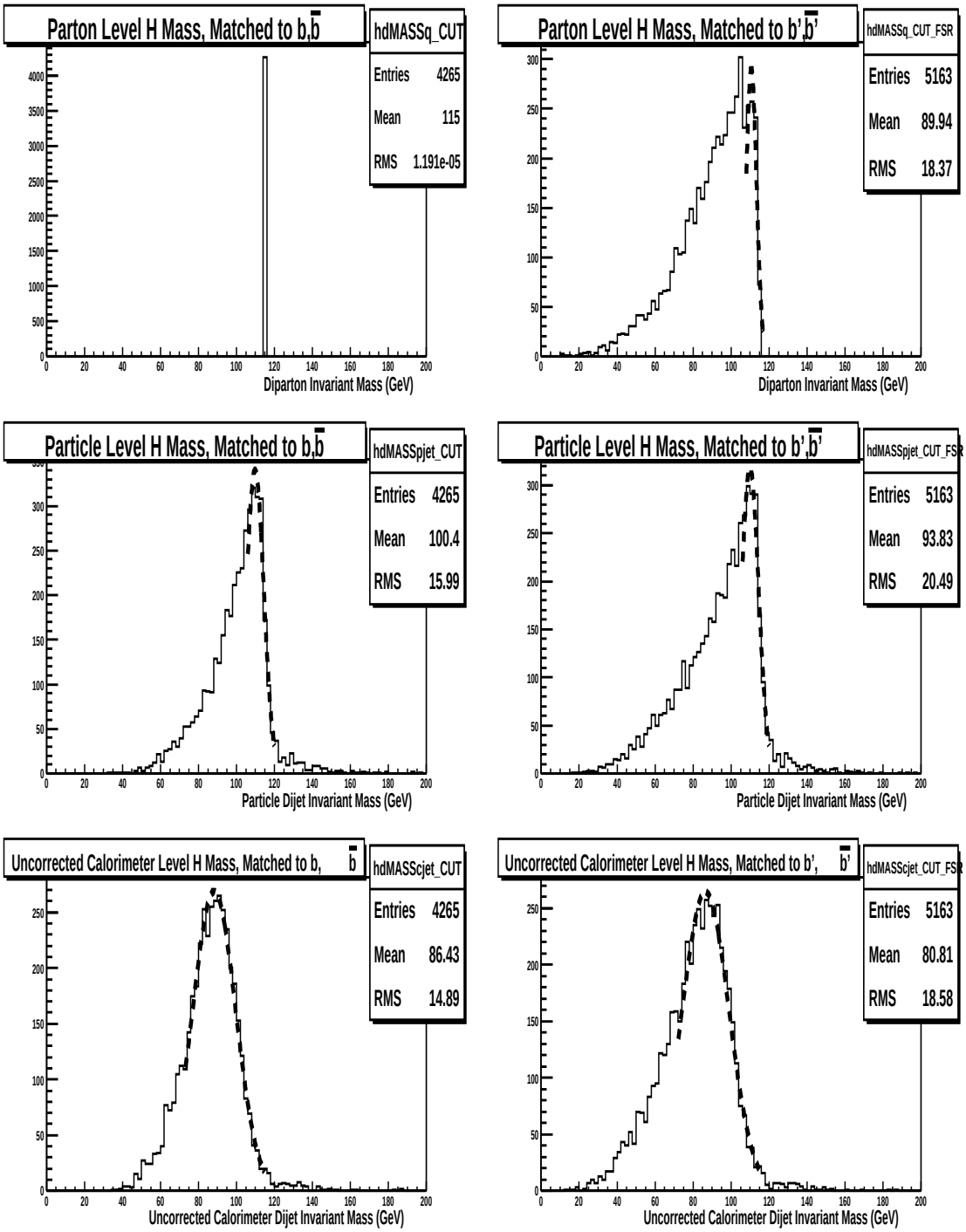

Figure 3.8: Reconstructed Higgs mass at parton (top), particle-jet (middle) and uncorrected calorimeter-jet (bottom) levels. Without hard FSR (left); with hard FSR (right). All jets are 0.5 cone. Dashed profiles show Gaussian fits to the central symmetric portion of the peak of each distribution (i.e. excluding any tails).

energy tail as a result of increased energy loss from the b-partons. This degrades the mass resolution.

Particle Dijet Mass

Particle dijet mass spectra are characterised by a low-side tail, as may be seen in the middle panel. Without hard FSR, the particle-level distribution consists of the following elements:

1. A central Gaussian due to fragmentation and hadronisation;

2. A low-end tail as a result of soft gluon radiation and jet splitting;

3. A high-end tail arising from the merging of jets.

When hard gluon radiation is included, the low energy tail becomes longer. As a consequence, the mean of the mass distribution decreases while the RMS increases.

Calorimeter Dijet Mass

At the calorimeter level the distributions correspond to the measurements made by the detector. The mass spectra are inherently Gaussian as a result of the various detector resolution effects. Moreover, the mean mass at this level is significantly smaller than at the parton and particle levels. This is mainly due to the energy response of the calorimeter to low energy particles, particles lost in 'cracks' of the detector and out-of-cone showering, and illustrates the need for jet energy scale corrections. Including hard FSR at the calorimeter level does not affect the shape of the mass spectrum as much as at the previous two levels. It does, however, significantly increase the width, thereby degrading mass resolution. In addition, it decreases the mean mass by a few GeV/c^2.

Calculating The Mass Resolution

There is no single way to evaluate the mass resolution, hence a number of different measures of the fractional resolution, $\frac{\sigma_M}{M}$, were explored:

1. **Central Gaussian (CG)**: A Gaussian curve was fitted to the central (symmetric) part of each distribution (as described previously) and the mass resolution was taken to be the $\frac{\sigma}{\mu}$ of this fitted curve;

2. $\boldsymbol{\mu \pm 3\sigma}$: The distribution was restricted to 3σ either side of the fitted mean (f the central Gaussian). Fractional mass resolution was defined as the $\frac{\text{RMS}}{\text{Mean}}$ of this restricted distribution;

3. $\boldsymbol{\mu \pm 5\sigma}$: The spectrum was restricted to 5σ either side of the fitted mean and, as above, the resolution was taken to be $\frac{\text{RMS}}{\text{Mean}}$ of this restricted distribution;

4. **Overall Distribution**: The mass resolution was defined as the $\frac{\text{RMS}}{\text{Mean}}$ of the overall distribution.

Distribution	Measure of Mass Resolution (%)			
	CG	$\mu \pm 3\sigma$	$\mu \pm 5\sigma$	Overall
Parton	\	\	\	\
Parton incl. FSR	2.5	3.4	5.0	20.4
Pjet	4.2	6.2	8.6	15.9
Pjet incl. FSR	4.1	5.7	9.1	21.8
Cjet	12.8	14.9	16.7	17.2
Cjet incl. FSR	14.2	18.1	22.4	23.0

Table 3.5: Fractional Higgs boson mass resolutions at parton, particle ('pjet') and uncorrected calorimeter ('cjet') levels, excluding and including hard FSR. Four different measures of resolution were calculated for each level. No jet energy scale corrections were applied at this stage.

Table 3.5 summarises the Higgs mass resolution at each level, calculated using these four different definitions. The errors on the mass resolutions were measured to be $\pm 0.5\%$. As we extend the range of the distribution used to calculate mass

resolution (going from left to right in Table 3.5), more FSR is gradually incorporated and the effects of the tails are included. Thus the mass resolution degrades.

The $\frac{\text{RMS}}{\text{Mean}}$ of the overall distribution (final column of Table 3.5) was determined to be the most appropriate measure of mass resolution with which to proceed. In further studies, this is the resolution quoted. Thus at the uncorrrected calorimeter level, one can expect to obtain a Higgs mass resolution of 17% (23%) excluding (including) hard gluon radiation.

As in the Higgs case, the Z resolutions generally worsen as more of the mass distribution is included in our measurement (see Table A.1 in Appendix A). At the calorimeter level, when hard final state radiation is excluded the Z and Higgs mass resolutions are equal at about 17%. This is as a result of two competing effects. In the Higgs decay more energy is available; since the fractional detector resolution improves with energy, this leads to more precise mass reconstruction. However, soft gluon radiation, which degrades mass resolution, also increases with energy. Overall these two effects cancel to yield equal Z and Higgs mass resolutions.

When hard gluon radiation is taken into account, the Higgs mass resolution is found to be approximately 2% worse (in absolute value) than that of the Z. The amount of gluon radiation increases with energy, so it occurs more frequently in the $ZH \to e^+e^-b\bar{b}$ decay and a worse Higgs mass resolution is obtained.

3.7.2 Effect of The Jet Correction on Mass Resolution

Figure 3.9 illustrates qualitatively the effect of jet energy corrections on the di-b-jet mass resolution, using the Higgs mass as an example. Table 3.6 summarises the effect quantitatively, for both $ZH \to e^+e^-b\bar{b}$ and $Z \to b\bar{b}$. The mass distributions studied are at calorimeter level. The measured resolutions have an error of the order of $\pm 0.5\%$, determined by systematically rebinning the distributions and measuring the effect on the value of the $\frac{\text{RMS}}{\text{Mean}}$.

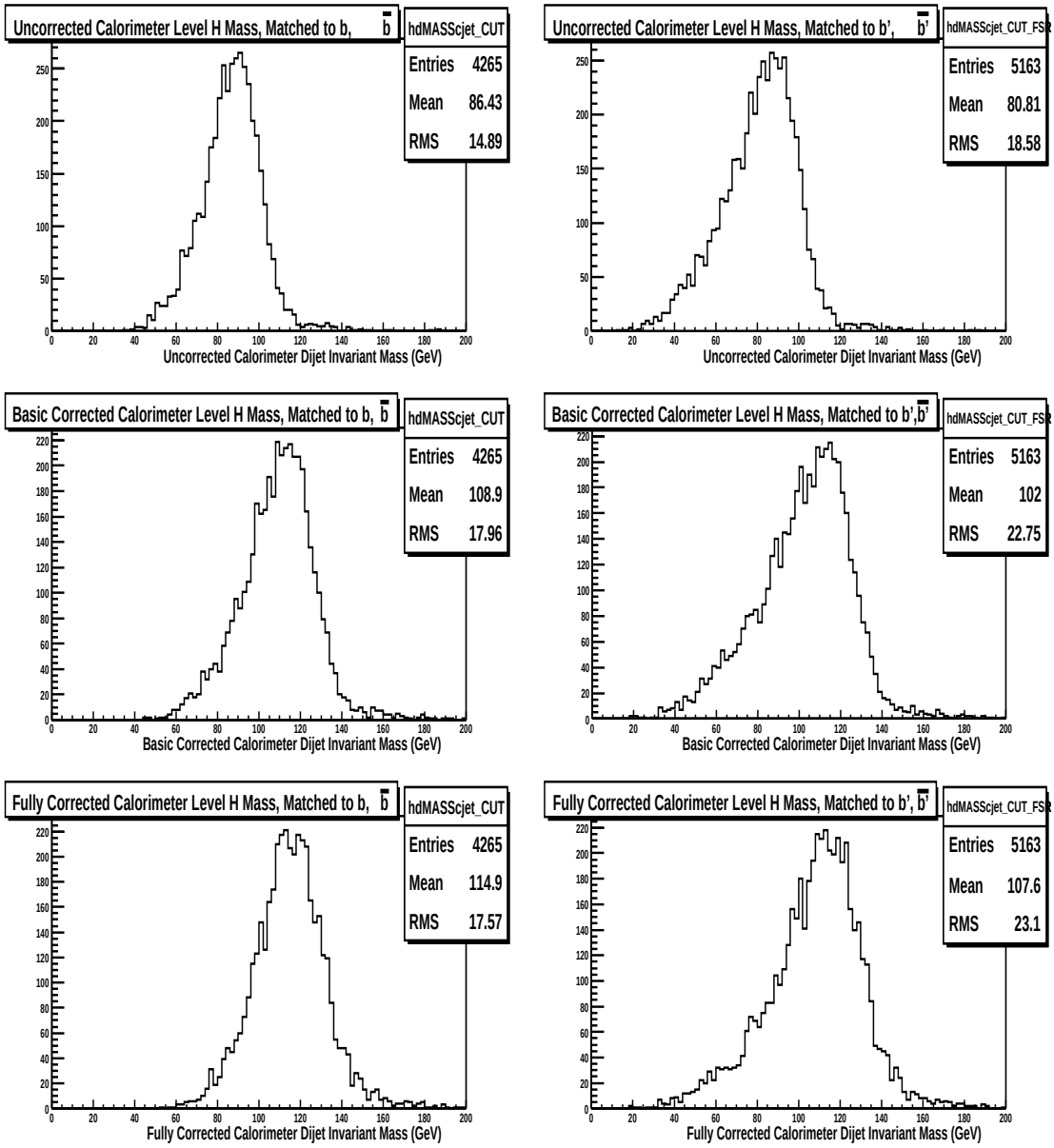

Figure 3.9: Reconstructed Higgs mass at calorimeter-jet level with no jet correction (top), basic correction (middle) and full, i.e. basic + muon, correction (bottom). Without hard FSR (left); with hard FSR (right). All jets are 0.5 cone.

As successive levels of the jet correction are applied, the fractional mass resolution improves. Jet energy corrections systematically shift the mean mass to higher values, and the spread of the distributions also tends to increase as the basic correction is applied. That said, the improvement in mean outweighs the increase in spread, thereby decreasing $\frac{\text{RMS}}{\text{Mean}}$ overall. The full jet energy scale correction provides

Jet Correction Applied	Mass Resolution at Calorimeter Level (%)			
	Higgs		Z	
	No FSR	With FSR	No FSR	With FSR
No correction	17.2	23.0	17.5	21.2
Basic correction	16.5	22.3	17.2	20.9
Basic + muon correction	15.3	21.5	16.4	20.4

Table 3.6: The effect of the jet correction on fractional Higgs and Z mass resolutions, including and excluding hard FSR. The basic correction compensates for response, offset and showering while the muon correction accounts for the semileptonic decay of b-jets (into muons).

the best mass resolution. As one would expect, the inclusion of hard FSR worsens mass resolution even with jet corrections.

3.7.3 Effect of Jet Multiplicity on Mass Resolution

The mass resolution was also measured as a function of the number of jets in the event. For this purpose, jet multiplicity was defined as the number of hadronic clusters in an event (termed here as 'nhad'). nhad represents the number of calorimeter jets which are isolated from electrons but which aren't necessarily good quality jets. The use of nhad rather than, say, the number of good jets in an event more accurately simulates the situation in real data.

The values of jet multiplicity tested were 2, 3, 4 and 5 or more, and Figure 3.10 presents the results for $ZH \rightarrow e^+e^-b\bar{b}$ as an example. The effect is illustrated at the calorimeter level, although constraining the jet multiplicity will also have an impact at the parton and particle levels. Table 3.7 provides the mass resolutions at all three levels; the resolutions were computed using the RMS and mean values of the overall mass distribution in each case. The errors on the mass resolutions were measured to be 0.5%.

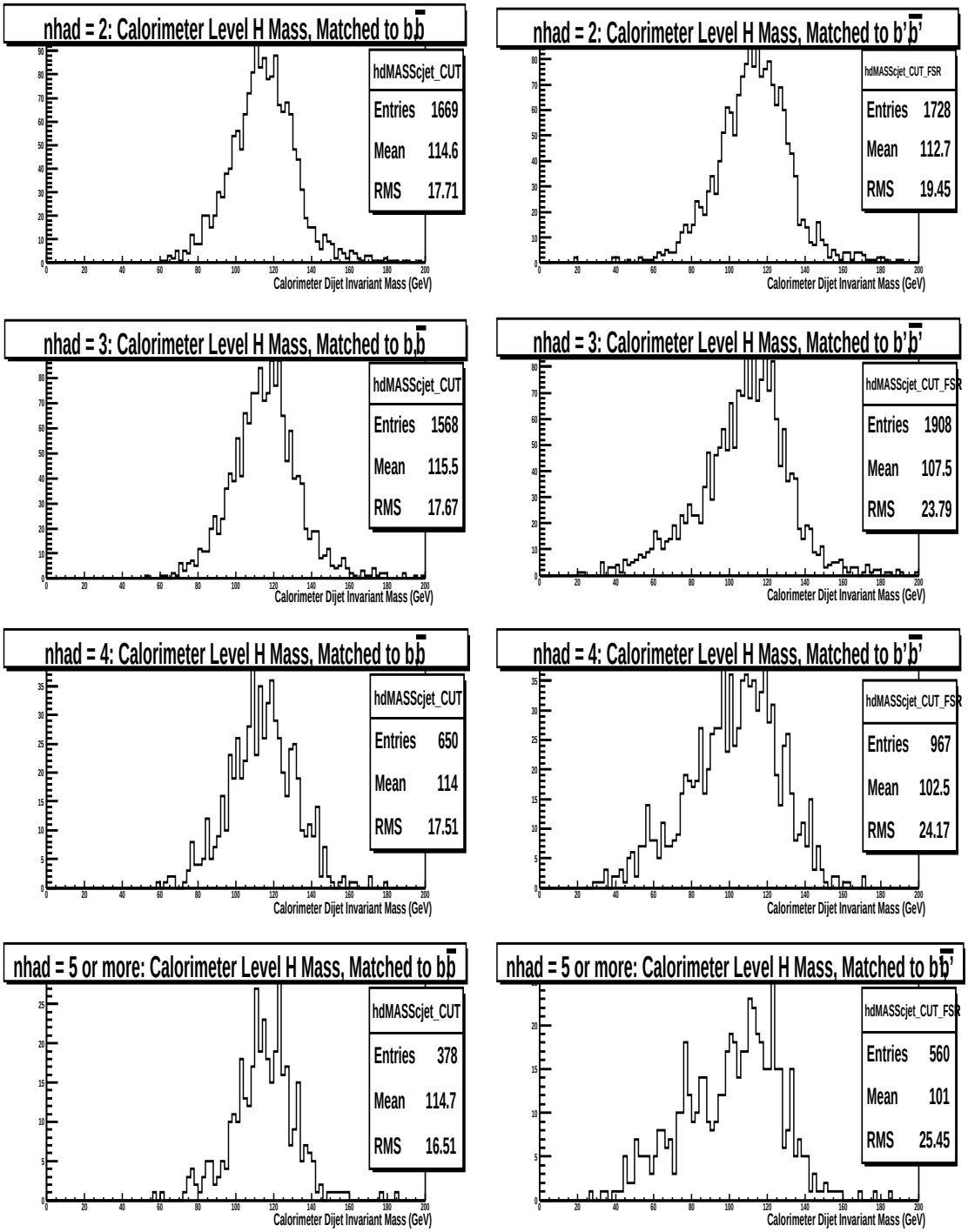

Figure 3.10: The effect of jet multiplicity on the Higgs mass resolution at calorimeter level. From top to bottom: nhad = 2; nhad = 3; nhad = 4; nhad $\geq$ 5. Without hard FSR (left); with hard FSR (right). All jets are 0.5 cone, no jet p_T cuts were imposed and full jet energy scale corrections were applied.

Similar effects are seen for both the Higgs and Z cases. Without hard FSR, increases in jet multiplicity have no effect on mass resolution at any given level, within the errors. However, when hard FSR is included, increases in jet multiplicity degrade the mass resolution. In particular, the resolution significantly degrades on moving from nhad = 2 to nhad = 3, where the third jet is most likely a hard gluon jet radiated from one of the b-jets. Note that statistics are lower for events with nhad $\geq$ 5.

Distribution	**Fractional Mass Resolution (%)**			
	nhad = 2	**nhad = 3**	**nhad = 4**	**nhad $\geq$ 5**
Parton	\	\	\	\
Parton incl. FSR	16.8	20.9	22.3	23.9
Pjet	16.2	15.8	15.9	14.9
Pjet incl. FSR	18.1	22.0	23.5	26.1
Cjet	15.5	15.3	15.4	14.4
Cjet incl. FSR	17.3	22.1	23.6	25.2

Table 3.7: Fractional Higgs boson mass resolutions as a function of jet multiplicity, at parton, particle ('pjet') and corrected calorimeter ('cjet') levels, excluding and including hard FSR. All jets are 0.5 cone, no jet p_T cuts were imposed and full energy scale corrections were applied.

3.7.4 Effect of Jet p_T Cut on Mass Resolution

Next, the effect of the jet p_T cut upon the mass resolution was investigated. The following p_T cuts were applied to all calorimeter jets: no cut (corresponding to the jet reconstruction threshold of $p_T > 8$ GeV/c), $p_T > 10$, 12, 15 and 20 GeV/c. As usual, 0.5 cone jets were used, all calorimeter jet energies were fully corrected and no constraints were imposed upon the jet multiplicity.

Figure 3.11 illustrates what happens to the Z mass as the jet p_T cuts are progressively applied, while Table 3.8 presents the mass resolutions measured. Once again, the RMS and mean of each overall distribution were used to compute these numbers. As can be seen from Table 3.8, as the jet p_T cut increases the Higgs and Z mass resolutions improve.

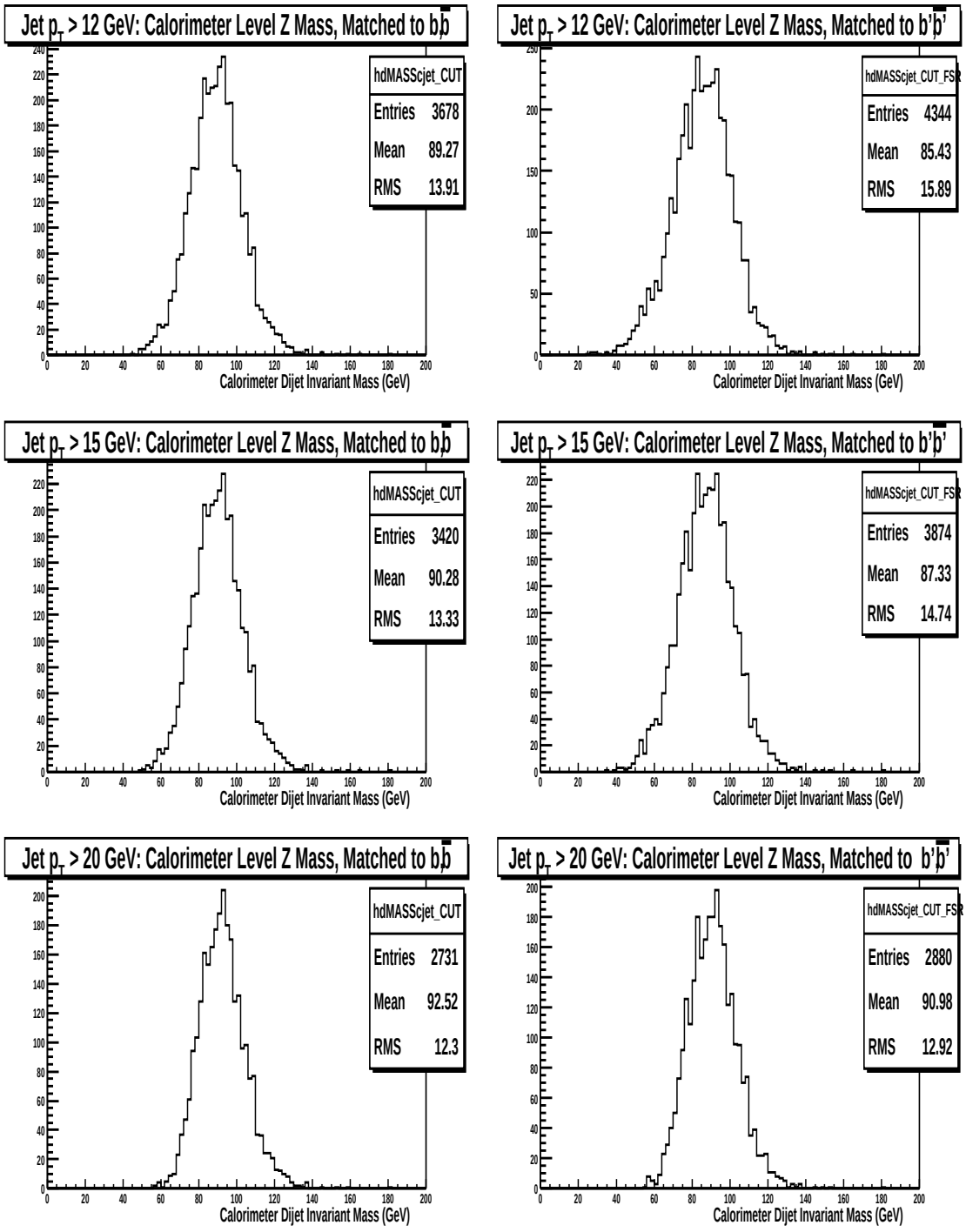

Figure 3.11: The effect of jet p_T cut on the Z dijet mass at calorimeter level. p_T cuts of 12 (top), 15 (middle), and 20 GeV/c (bottom) are shown, without hard FSR (left) and with hard FSR (right). Jets were 0.5 cone and full jet energy scale corrections were applied.

Jet p_T Cut Applied (GeV/c)	Mass Resolution at Calorimeter Level (%)			
	Higgs		*Z*	
	No FSR	With FSR	No FSR	With FSR
8 (no cut)	15.3	21.5	16.4	20.4
10	15.2	21.0	16.1	19.7
12	15.0	20.3	15.6	18.6
15	14.7	19.3	14.8	16.9
20	14.2	17.6	13.3	14.2

Table 3.8: Effect of calorimeter-jet p_T cut on Higgs and Z mass resolutions. All jets were 0.5 cone and full jet corrections were applied.

3.7.5 Effect of Recombination on Mass Resolution

Studies were carried out in order to determine whether or not the process of recombination - that is, combining a radiated gluon jet with its sister b-jet - could offer improvements in the mass resolution obtained. For every instance of hard FSR, the gluon jet was recombined with its corresponding b'- or $\overline{b'}$-jet at the calorimeter level. MC information was used to identify the b'- (or $\overline{b'}$-) jet and gluon jet; in a real-life analysis this information is not available and it is harder to identify the products of final state radiation.

The degree of recombination was varied by imposing different dR cuts on the (b'-jet, gluon jet) pair. As the value of dR was successively increased from 1 to 2 to 3 to 4, the amount of recombination was increased. These dR values were selected by studying the typical separation between gluon jets and their sister b-jets (see for example the distribution shown in the top left pane of Figure 3.12). These recombined jets were then used to reconstruct the Higgs and Z masses at calorimeter level. All jets were 0.5 cone, jet energy scale-corrected, no jet p_T cuts were applied and jet multiplicity was unconstrained. The resolutions are summarised in Table 3.9; they were again calculated using the RMS and mean amd errors on these values are $\pm 0.5\%$.

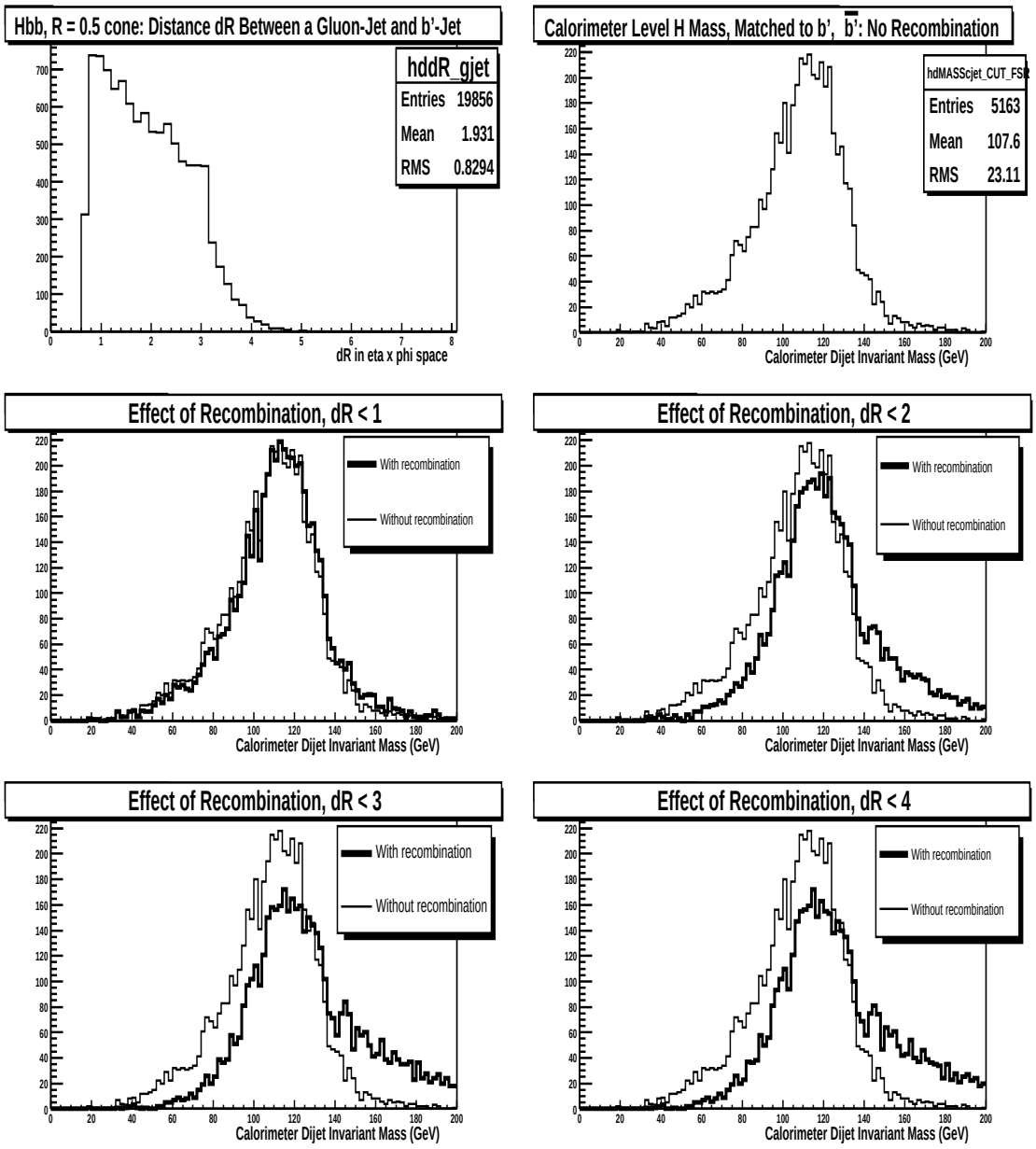

Figure 3.12: The effect of recombination on Higgs mass resolution. Top left: $dR(b'$-jet, gluon jet) distribution; top right: calorimeter dijet mass without recombination; the other plots show the effect of recombination for $dR < 1$, 2, 3, 4.

For the Higgs mass, recombination with a $dR < 2$ is the optimum choice. With no recombination the mass distribution is asymmetric, having a larger low-end tail than high-end tail as a result of hard FSR. Recombination (for $dR < 2$) effectively moves entries from the low-energy tail to the high-energy tail without degrading the mass resolution. This could potentially improve the signal to noise ratio when searching

Amount of Recombination Applied	Mass Resolution at Calorimeter Level (%)	
	Higgs	Z
None	21.5	20.4
$dR < 1$	21.4	21.2
$dR < 2$	21.6	24.8
$dR < 3$	22.3	27.2
$dR < 4$	22.3	27.6

Table 3.9: The effect of recombination on fractional Higgs and Z mass resolutions. As dR increases, the amount of recombination increases. All jets were 0.5 cone and calorimeter jets were fully energy-scale corrected.

for a mass peak against a large QCD background, however detailed studies of the effect of recombination on the background would be required. Further amounts of recombination are unsuitable as they degrade the mass resolution.

For the Z boson, its calorimeter-level mass distribution is already very symmetric before any recombination is applied, because less hard FSR occurs in the Z decay than in the Higgs decay (see bottom two panels of Figure A.1, Appendix A). Increasing amounts of recombination gradually worsen the mass resolution while degrading the symmetry of the distribution (plots not included here). Thus for $Z \rightarrow b\bar{b}$, recombination offers no significant advantages.

3.8 Summary

b-jet energy and mass resolutions were explored in detail in the $ZH \rightarrow e^+e^-b\overline{b}$ and $Z \rightarrow b\overline{b}$ channels. The b-partons and particle- and calorimeter-level b-jets were spatially matched after hard scattering and after hard final state radiation.

The b-jet energy resolution improves on moving from the calorimeter-parton to calorimeter-particle to particle-parton levels, as expected. Cone jets provide better resolution than k_T jets and the 0.5 cone algorithm is best. The magnitude of the effect of hard FSR on b-jet resolution (from the Higgs) is approximately 10% at calorimeter-parton and particle-parton levels, and negligible at the detector level. At a given p_T, b-jet resolutions from the Higgs and Z are equal without hard FSR. However, with hard FSR at the calorimeter-parton level the Higgs resolution is worse than that of the Z by approximately 5%.

Mass resolution studies reveal that the Higgs mass resolution ($\frac{\text{RMS}}{\text{Mean}}$ at calorimeter level, energy scale corrected) increases from 15% to 21% upon inclusion of hard FSR (the error on these measurements is of the order of 0.5%). For the Z, the increase is from 16 to 20%. Jet corrections improve the dijet mass resolution in absolute terms by 1 to 2%. Increases in jet multiplicity degrade the mass resolution after hard FSR while having little effect on the mass resolution before hard FSR. An increase in the jet p_T cut from no cut (implicit 8 GeV/c threshold) to a 20 GeV/c cut improves the Higgs (Z) mass resolution by 4% (6%), in real terms. Recombination is potentially useful for reconstructing the Higgs mass; a dR cut < 2 significantly improves the low-end tail of the distribution while leaving the resolution unchanged. For the Z mass, recombination offers no significant advantage.

As the first study of jet energy and mass resolutions at DØ using a full Run II simulation, this work served as a baseline for further progress. With regard to b-jet energy resolution, at the time of these studies the resolutions measured in Run II data were 1–2% worse than the Monte Carlo results predicted here (for b-jets with

an average E_T of 55 GeV, which is an appropriate energy for b-jets coming from the Higgs). In an effort to improve the resolution attainable, work was undertaken to fully calibrate the calorimeter (both the hadronic and electromagnetic components). These calibrations are now complete and have removed the discrepancy.

Higgs sensitivity investigations [16] that came after this work showed that the di-b-jet mass resolution could be improved by approximately 5% by imposing p_T cuts on the leading jets, restricting the mass range to a window around the Higgs mass and applying more sophisticated jet algorithms. A promising energy clustering algorithm involves combining track and jet information to form track-jets [46] and is currently being adopted at DØ.

Chapter 4

Triggering on $Z \to b\bar{b}$

"Results? Why, I have got a lot of results. I know 50,000 things that won't work."

Thomas Edison

4.1 Overview

This chapter describes the official triggers developed for the $Z \to b\bar{b}$ search at DØ. Five triggers were designed to operate up to luminosities of 0.80×10^{32} cm^{-2}s^{-1} as part of DØ's trigger list at the time, known as 'version 13' (v13).

The DØ trigger list contains triggers geared towards the study of B-physics, electroweak physics, new phenomena, QCD processes, Higgs physics and top-quark physics. The B-physics group in particular relies upon generic muon-based triggers that trigger on the presence of one or more muons in b-jet events. In the search for $Z \to b\bar{b}$ we also rely on muon triggers, however, the B-physics triggers are not suitable for our channel at high luminosity. B-physics measurements typically rely on being able to reconstruct the momentum and decay vertex of all particles with extremely high precision. As the resolution of these measurements worsens with increasing p_T, the B-physics group therefore applies prescales at high luminosities rather than applying tighter trigger conditions (i.e. higher p_T cuts) in order to comply with the experiment's overall bandwidth requirements. As such, at high

luminosities many of the B-physics triggers are turned off. Since signal acceptance is the product of signal efficiency × integrated luminosity and the B-physics triggers are turned off at high luminosity, their overall signal acceptance is low. We therefore needed to design specific $Z \rightarrow b\bar{b}$ triggers that would be able to run unprescaled at the highest luminosities.

For these $Z \rightarrow b\bar{b}$ triggers, events are selected at Levels 1 and 2 using different muon or muon plus jet triggers. At Level 3 further rejection is achieved using b-tagging, muon requirements and jet and vertexing tools. Each trigger has been optimised to yield a combined background rate of between 3 and 4 Hz averaged over all luminosities. The optimal trigger terms were then presented to the DØ Trigger Board, who accepted the proposal. These triggers have been running online since June 2004.

4.2 Triggering at DØ

Triggering is the crucial aspect of the physics at a hadron-hadron collider. Only with efficient and intelligent triggers can rare and interesting physics events be discriminated from the massive QCD background. Designing a physics filter that is specific to the $Z \rightarrow b\bar{b}$ channel improves the chance of observing the signal with Run II data. Light quark rejection is needed at the trigger level, prior to any offline event selection, in order to achieve an acceptable trigger rate.

Bandwidth constraints at Level 3 (L3)[1] limit the combined rate to tape for all DØ physics channels to a maximum of 50 Hz, as discussed in Section 2.4.5. For our five $Z \rightarrow b\bar{b}$ triggers this translates to an upper limit of 3 to 4 Hz out of L3, taking into account the other physics needs of the collaboration. Naturally there will be a degree of overlap between these triggers that will reduce the total amount of bandwidth occupied by all five. The triggers must be sufficiently tight to meet this bandwidth criterion, otherwise they have to be prescaled. When a trigger is

[1]The following notation is adopted: L1 for Level 1, L2 for Level 2 and L3 for Level 3.

prescaled it is run only on a fraction of events; for example a trigger with prescale 5 is only applied to 1 in every 5 events. In terms of event yield or integrated luminosity, a trigger that is 20% efficient for signal is always preferable to a prescale of 5, since a prescale is applied randomly.

As with any trigger there is a fine balance between the rejection of background events and the efficiency for passing signal events. The process is one of optimisation. Consideration must also be given to the evolution of the instantaneous luminosity with time and the subsequent changes in prescaling. All of these aspects make designing triggers extremely complex.

4.2.1 Tailoring Triggers Towards $Z \to b\bar{b}$

These $Z \to b\bar{b}$ triggers are a combination of muon plus jet triggers. Each event must contain at least one muon from a b-jet and must satisfy other jet criteria. Ideally one would trigger on dijet events with displaced vertices at Level 2 using the Silicon Track Trigger, but this capability was not available at the time of these studies. Instead, the semileptonic decay of the b-jets is exploited, harnessing the excellent muon coverage of the detector to trigger on events containing muons. Requiring muons from one or both of the b-jets in each event limits the signal efficiency as a result of the small $b \to \mu$ and $b \to c \to \mu$ branching fractions, but this remains the most feasible approach for now.

v13 Trigger	**Trigger Conditions**		
	Level 1	**Level 2**	**Level 3**
ZBB_TLM3_2JBID_V	Single muon + track	$\geq$1 muon	$\geq$1 muon, IP tag, vtx cut, 2 jets
ZBB_TLM3_2LM0_2J	Single muon + track	$\geq$1 muon	$\geq$2 medium muons, 2 jets
MUJ1_2JT12_LMB_V	Single muon + 2 jets	$\geq$1 muon + $\geq$1 jet	IP tag, vtx cut, muon, $\geq$2 jets
MUJ2_2JT12_LMB_V	Single muon + jet	$\geq$1 muon + $\geq$1 jet	IP tag, vtx cut, muon, $\geq$2 jets
DMU1_JT12_TLM3	Dimuon term	$\geq$1 muon	$\geq$1 trk-matched muon, jet

Table 4.1: Description of the five dedicated $Z \to b\bar{b}$ triggers designed to run unprescaled up to luminosities of about 0.80×10^{32} cm^{-2}s^{-1} as part of the v13 trigger list. "trk-matched" stands for track-matched; "vtx cut" indicates vertex cut.

Table 4.1 describes the finalised set of $Z \rightarrow b\overline{b}$ triggers; in the sections that follow we will describe how we arrived at these triggers. The aim is to construct a versatile suite of triggers that cover different characteristics of the $Z \rightarrow b\overline{b}$ decay, thus improving the access to a clean signal. Four of the triggers presented above identify single-muon events while the fifth selects clean but rare dimuon events. At L1 and L2 muon criteria, and in some cases additional jet conditions, are applied to pass or reject events. At L3 more refined tools are used to achieve the background rejection that will meet the detector's bandwidth constraints. These extra handles include constraints on muons, jets and the event's primary vertex (PV) as well as the use of impact parameter (IP) b-jet tagging.

4.2.2 Tagging Beautiful Jets

The lifetime of the b-quark (about 10^{-12} s) is significantly longer than the time it takes for hadrons to form (of the order of 10^{-22} s). Thus the b-parton emerges from the proton-antiproton interaction within a B hadron. A high-momentum B meson can typically travel a few mm before it decays and, with the help of very precise silicon-based tracking close to the interaction point, the secondary vertices associated with its decay can be reconstructed. Figure 4.1 illustrates such a displaced vertex. By triggering on the secondary vertices in events one can drastically reduce the overwhelming light-quark background that would otherwise swamp a $Z \rightarrow b\overline{b}$ signal.

The idea behind an impact parameter tagger is to make use of the long lifetime of B hadrons without explicitly having to identify a decay vertex. This can be done by considering the likelihood that a collection of charged tracks have originated from the interaction's PV. By analysing all of the tracks in a jet, one can deduce the probability that the jet contains a b-quark.

The discriminating variable that is used to construct this probability is the "impact parameter" or IP. Here the term impact parameter refers to the distance of

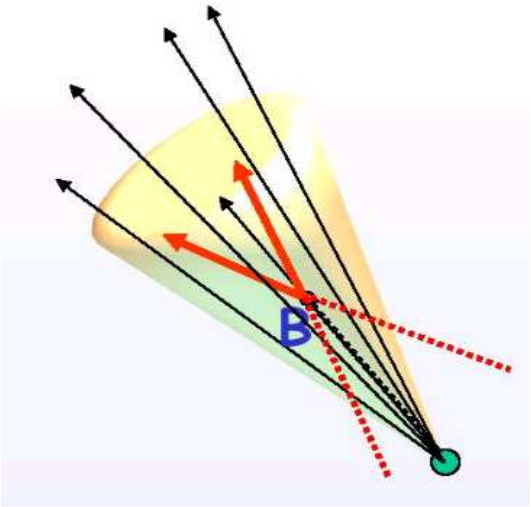

Figure 4.1: Illustration of a secondary vertex within a jet. A B hadron typically travels a few mm away from the interaction's primary vertex before it decays. By looking for tracks which originate from the secondary vertex (red (bold) dotted arrows) we can deduce the likelihood that the jet contains a b-quark.

closest approach of a track to the PV in the transverse (x-y) plane. Figure 4.2 shows a light-quark jet in this plane along with its associated tracks.

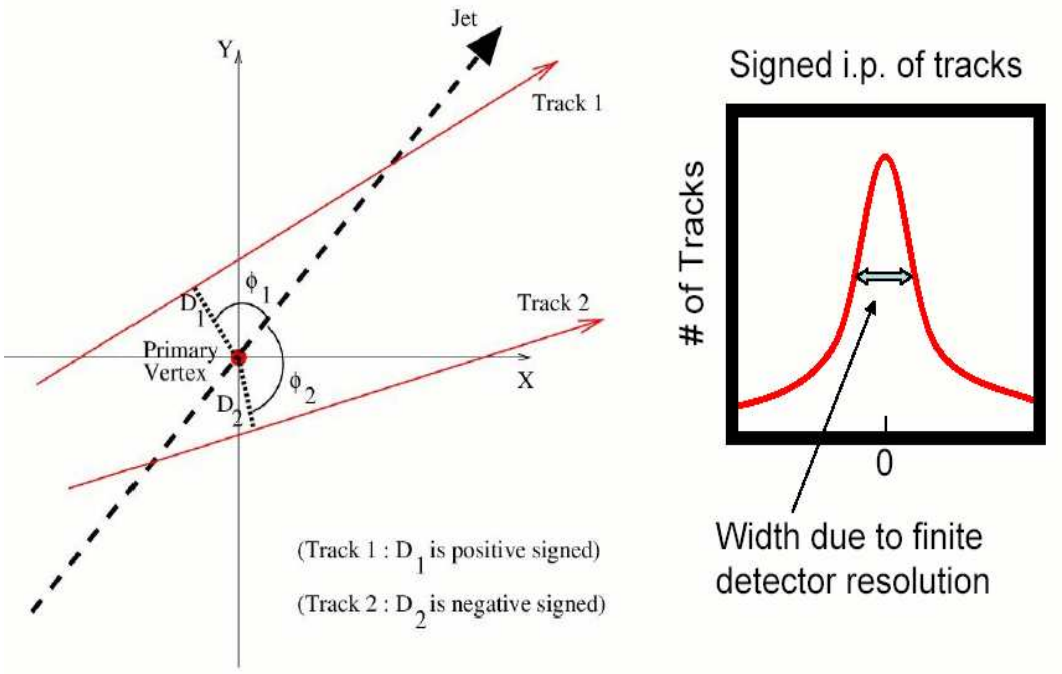

Figure 4.2: Tracks in a light-quark jet and their signed IPs, D_1 and D_2. The signed IP distribution is symmetric and has a non-zero width due to detector resolution effects.

Tracks 1 and 2 within the light-quark jet each yield an impact parameter, D_1 and D_2, as shown. Each IP is given a sign: positive if the track and jet direction intersect upstream of the PV (i.e., in the same hemisphere as the jet), and negative if they intersect downstream of the PV. In Figure 4.2 above, D_1 (from track 1) is positive signed and D_2 (from track 2) is negative signed. Now, if we were to plot the signed IPs of all tracks within the light-quark jet we would observe a symmetric distribution as shown on the right-hand side of Figure 4.2. It has a non-zero width as a result of finite detector resolution; resolution effects mean that we might measure a non-zero IP value even for tracks that really do come from the primary vertex, but with equal probability of being positively or negatively signed.

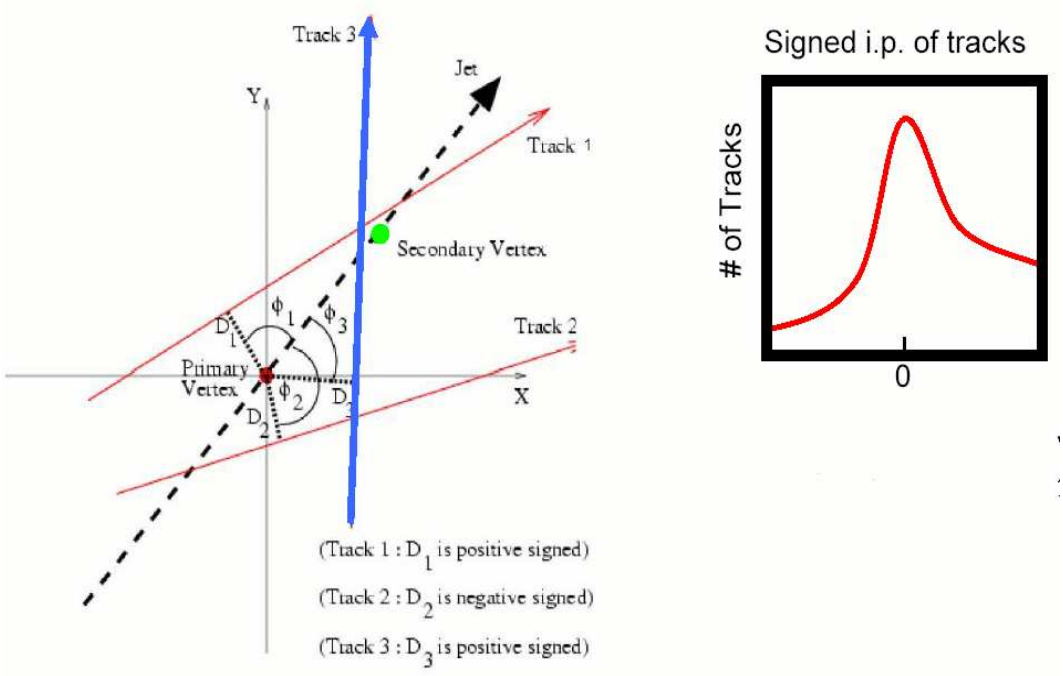

Figure 4.3: Tracks in a b-quark jet and their signed IPs, D_1, D_2 and D_3. The signed IP distribution becomes skewed towards positive values as a result of the secondary vertex.

Next, consider an event that contains a b-quark and therefore a displaced vertex (Figure 4.3). Still present are tracks 1 and 2, with corresponding signed IPs D_1 (positive signed) and D_2 (negative signed). But now a third track is found within the b-jet. This track originates from the secondary vertex and its IP, D_3, is positive

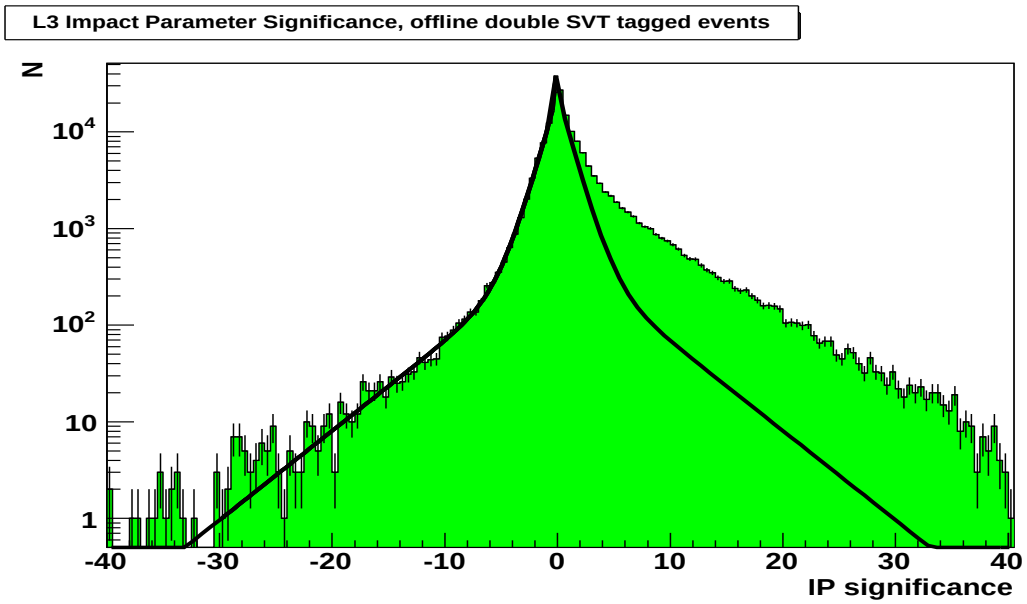

Figure 4.4: Signed impact parameter distribution from data events that contain two offline b-tags. The excess seen in the right-hand tail comes from b-tagged events. The bold black line shows a fit to the negative side of the distribution (IP significance < 0) folded over to the positive side.

signed. The presence of the secondary vertex causes the signed IP distribution to become skewed, as illustrated in the right-hand side of Figure 4.3, and it acquires a positively signed tail thanks to tracks associated with the displaced vertex. Figure 4.4 shows the signed impact parameter for data events that have two offline b-tags identified by DØ's secondary vertex or 'SVT' tagger (see Section 5.4.1 in Chapter 5 for further details). In this b-enriched sample, one can see an excess in the right-hand tail which corresponds to tracks not compatible with the PV - i.e., b-jet events with displaced vertices. The superimposed bold black line shows a fit to the negative (left-hand) side of the distribution, which is then folded over (reflected in the vertical plane given by signed IP $= 0$) to the positive (right-hand) side of the spectrum. The fit function used is a combination of a Gaussian plus two exponentials. By fitting the negative side, which consists of IPs coming from the PV, and folding the fit over, any discrepancy between the fit and data on the positive side reveals IPs that originate from displaced vertices.

From Impact Parameter to Jet Probability

Once the signed IP (D) of a track has been measured, a quantity known as the "signed impact parameter significance" (S_{IP}) is calculated. This is defined as the ratio of the signed IP to its total error, and is given by $S_{IP} = D/\sigma$, where σ is the error on the IP value for the track arising from the imperfect detector resolution. Using the IP significance one can compute, for each track in the event, a probability that the track originates from the PV:

$$P_{trk}(S_{IP}) = \frac{\int_{-\infty}^{-|S_{IP}|} R(s)\,ds}{\int_{-\infty}^{0} R(s)\,ds} \tag{4.1}$$

where $R(s)$ is a fit to the negative half of the signed impact parameter distribution for events with little or no b-quark (jet) content.

Then all N_{trk} tracks in the jet with a positive IP significance can be used to calculate an overall jet probability P_{jet}:

$$P_{jet} = \Pi \times \sum_{j=0}^{N_{trk}-1} \frac{(\text{-log}\prod)^j}{j!} \quad \text{where} \quad \Pi = \prod_{i=1}^{N_{trk}} P_{trk}(S_{IP}) \tag{4.2}$$

In equation 4.2 [47], P_{jet} represents the likelihood that a jet contains a displaced vertex and can be used to form an overall event b-tag probability. In practice, this is implemented by the `l3fbtag_ip` tool [48] at Level 3.

The event b-tag probability is plotted in Figure 4.5, for b-enriched data events that have passed two offline b-tags. It varies from 0 to 1; the closer the probability is to 0, the less likely the tracks derive from the PV and the more likely the event is to contain a b-quark. By cutting on this variable the rejection of light-quark background can be greatly increased at the trigger level. With respect to offline cuts (two loose secondary vertex tags), the Level 3 IP tagger identifies b-jets with an 80% efficiency (with a cut on the b-tag probability of 0.1), for a mistag rate (i.e. fraction of light quark jets that are incorrectly b-tagged) of 20%. Offline b-tagging algorithms do, however, offer much better discrimination.

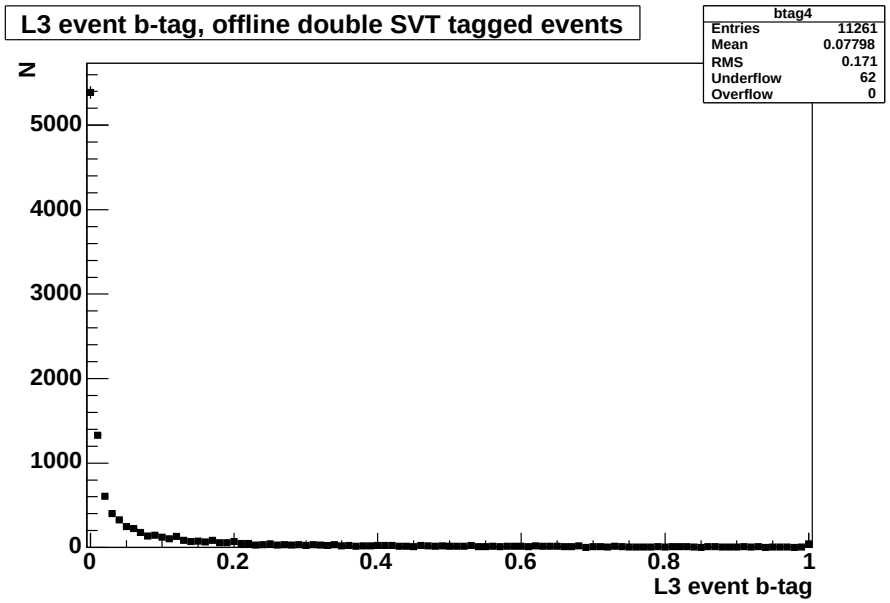

Figure 4.5: Level 3 event b-tag probability for data events that have two offline b-tags. The narrow peak near 0 indicates that the sample is rich in b-content.

4.3 Trigger Design Procedure

When preparing a new trigger list, one must first determine the new L1 and L2 terms and their efficiencies and rates before the L3 trigger conditions can be designed. The L1L2 portion of the trigger menu is established with the help of data collected in a "special run". Special runs are performed by the collaboration around normal data-taking for a variety of reasons: trigger development and study, detector calibration, tests of new hardware and software and accelerator studies. During a special run the trigger system is set up to operate a set of loose general L1 terms from which all other L1/L2 terms can be determined. Once L1 and L2 of the trigger list are fixed, another special run is taken with the new L1L2 trigger terms and just a prescale at L3. These data are then used offline to study the new proposed L3 terms and their rates.

Each of the five $Z \rightarrow b\overline{b}$ triggers were designed in this way, studying the efficiencies and rejections of each one in turn [49]. In the following section we demonstrate the process for one of those five triggers - MUJ1_2JT12_LMB_V. For this trigger the

base L1L2 conditions fixed from special runs were as follows:

- L1: a single muon located in any region of the detector plus two calorimeter jet trigger towers above 3 GeV (designated by the trigger term `mu1ptxatlx_CJT(2,3)`);

- L2: at least one "medium" quality muon and a 6 GeV jet. A muon is defined as medium if it produces at least two hits in the A layer wire chamber, at least one A layer scintillator hit, at least two BC[2] layer wire hits and one or more BC scintillator hits (except for central muons with less than four BC wire hits). A scintillator timing cut in the A and BC layers is used to reject muons from cosmic radiation. No constraints are imposed upon the muon p_T or its location in the detector.

Using this L1L2 foundation[3], we then studied the additional rejection that can be achieved by tuning the trigger conditions at L3. The goal is to obtain acceptable background rejection with an optimal signal efficiency. To this end various L3 parameters were investigated: event b-tag probability, first and second leading jet E_T and cut on the primary vertex z coordinate. In addition, the effect of cutting on the leading jet E_T at L2 was also studied.

The trigger studies were performed with two samples:

- MC: ∼70,000 $Z \rightarrow b\overline{b}$ events, generated with `PYTHIA` [37], passed through a full detector and trigger simulation and processed with version p14 of the DØ reconstruction software [39].

- Data: ∼40,000 events from special runs 180789 and 192720, also reconstructed with version p14. These data have a mean instantaneous luminosity of about $0.50 \times 10^{32}\text{cm}^{-2}\ \text{s}^{-1}$.

[2] A BC requirement means a hit in either layer B or layer C of the muon detector.

[3] For historical reasons this L1L2 base condition is referred to as the "prong B" trigger, as appears in later plots.

These events were processed using version p16.02.00 of the DØ trigger software - `d0trigsim` [50], `trigsim_analyze` [50] and `trigger_rate_tool` [51]. `d0trigsim` is a programme that passes raw events through a simulation of the online trigger system. `trigsim_analyze` takes `d0trigsim` output and produces a `ROOT` file containing histograms of all the trigger information desired. `trigger_rate_tool` calculates the anticipated trigger rates and overlaps for any trigger configuration.

While the above packages process and store trigger information for MC and data events, it is not trivial to gather together the offline and online information into the same roottuple for analysis. This is desirable because our studies must incorporate both online and offline elements, bearing in mind that the triggers are not independent of offline conditions. If the trigger and offline information appears in separate roottuples it is particularly difficult to deal with MC events that must pass both specific online conditions and offline requirements, especially when those online conditions are continuously evolving during a process of trigger design. First, the MC events must be passed through a trigger simulation. Second, the relevant trigger conditions are imposed and a 'trigger pass' list of events is generated. Meanwhile, the MC sample has to be separately processed through the offline event reconstruction software so that the correct offline information is stored for later use. Finally, the list of triggered events is fed into the offline analysis, taking care to ensure that the MC events in each processing stream (online and offline) match on an event-by-event basis. Once this has been done, the offline analysis can proceed using the triggered events. This routine had to be performed for every MC sample studied and involved a great deal of effort.

Efficiency (for signal and background) is defined as follows:

$$\text{Efficiency} = \frac{\text{Number of events passing L1L2L3}}{\text{Total number of events}}. \tag{4.3}$$

The efficiency in signal MC is a measure of how effectively the trigger selects $Z \rightarrow b\bar{b}$ events. Similarly, the efficiency in data is a measure of how much background passes

the trigger. In all of these studies, it is assumed that data represents the background. Since $S/\sqrt{S+B}$ is small for the $Z \rightarrow b\bar{b}$ process, this assumption is reasonable, and it is necessary since, at present, data model the background more accurately than MC. Background rejection is related to background efficiency by the expression

$$\text{Background rejection} = \frac{1}{\text{Background efficiency}}. \tag{4.4}$$

However, the denominator for real data is the number of events passing Levels 1 and 2, so the "efficiencies" are defined slightly differently for real data and MC events. In the figures that follow background efficiency rather than background rejection is always plotted. Efficiencies are quoted after events have satisfied all trigger level conditions.

4.4 Background Rejection

Figures 4.6 to 4.9 show the effect of L3 b-tag, L3 jet E_T and L2 jet E_T on the background efficiency. An efficiency of 100% corresponds to all events in the run. Events that contained no tracks or jets were eliminated prior to b-tagging at L3, since without this information the event b-tag probability cannot be determined.

Figure 4.6 shows the variation in background efficiency as a function of the cut on the b-tag probability. We apply a cut on the L3 b-tag probability first since this is likely to be the most powerful handle (for purposes of rejecting background) at our disposal. At this stage, only the set of 'basic' cuts are applied - i.e. those presented in the caption of Figure 4.6 - and no additional jet E_T cuts are imposed at L3 or L2.

It can be seen from Figure 4.6 that the background efficiency decreases as the cut on the b-tag probability tends towards 0. In other words, background rejection increases as a more strict constraint is imposed upon the b-content of the sample. As expected, a tighter L3 b-tag cut rejects more of the (light-quark) background.

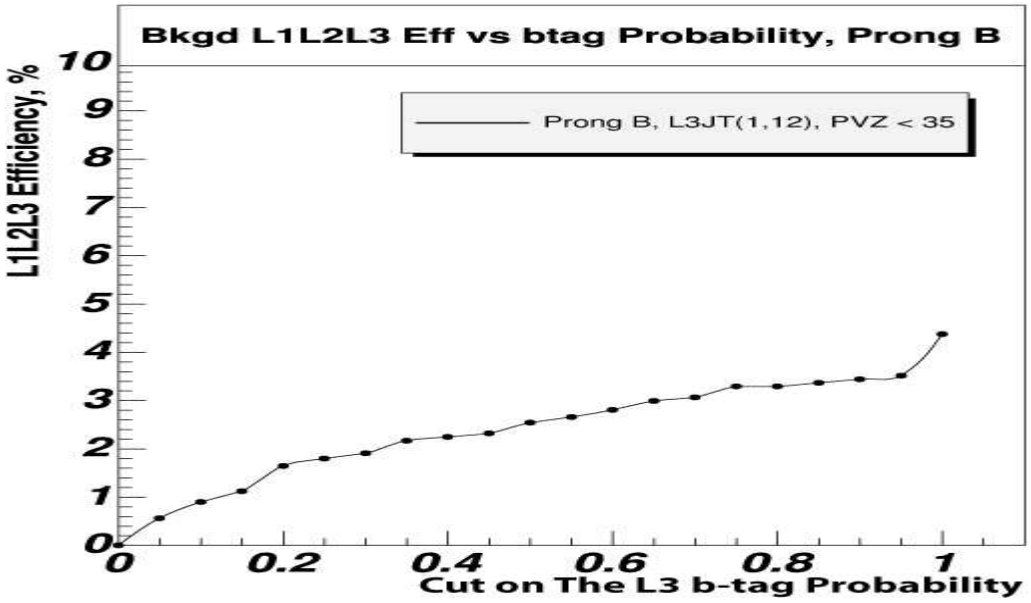

Figure 4.6: Background efficiency as a function of the cut on the L3 b-tag probability. The likelihood that the event is b-tagged increases as the probability approaches 0. Trigger combination applied while the cut on the b-tag probability was varied: one L2 jet above 6 GeV, one L3 jet above 12 GeVand an L3 primary vertex constraint of $|z| < 35$ cm.

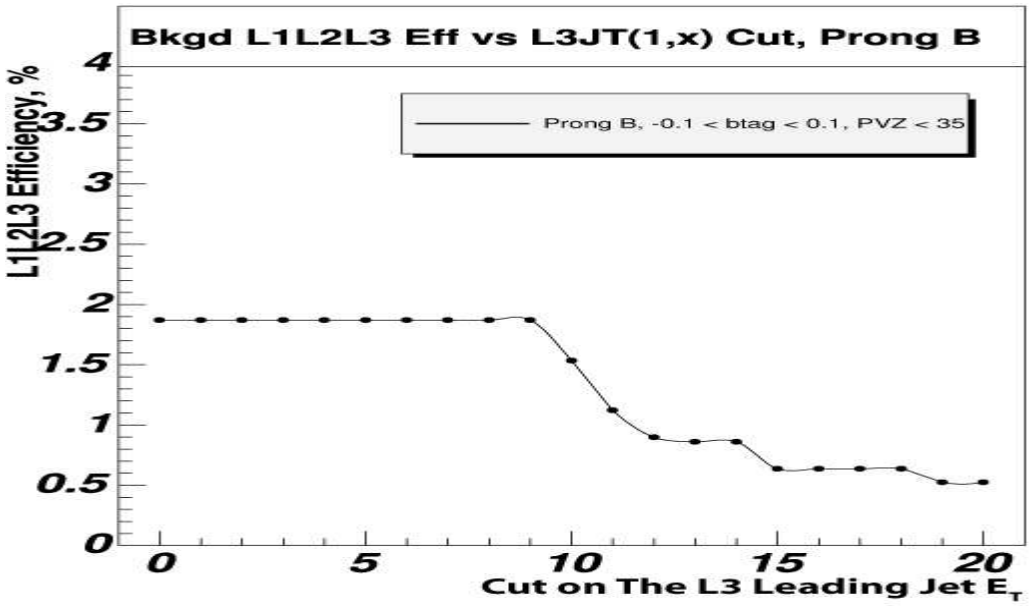

Figure 4.7: Background efficiency as a function of the cut on the leading jet E_T at Level 3. Trigger combination applied while the cut on the L3 jet E_T was varied: one L2 jet above 6 GeV, an L3 b-tag probability < 0.1 and an L3 primary vertex constraint of $|z| < 35$ cm.

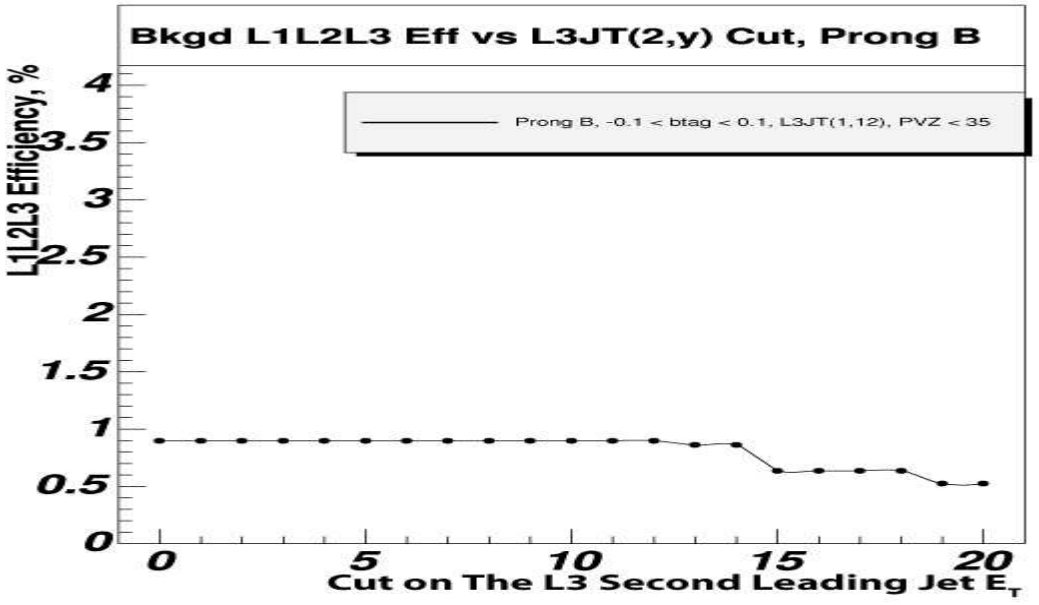

Figure 4.8: Background efficiency as a function of the cut on the second leading jet E_T at Level 3. Trigger combination applied while the cut on the L3 jet E_T was varied: one L2 jet above 6 GeV, one L3 jet above 12 GeV, an L3 b-tag probability < 0.1 and an L3 primary vertex constraint of $|z| < 35$ cm.

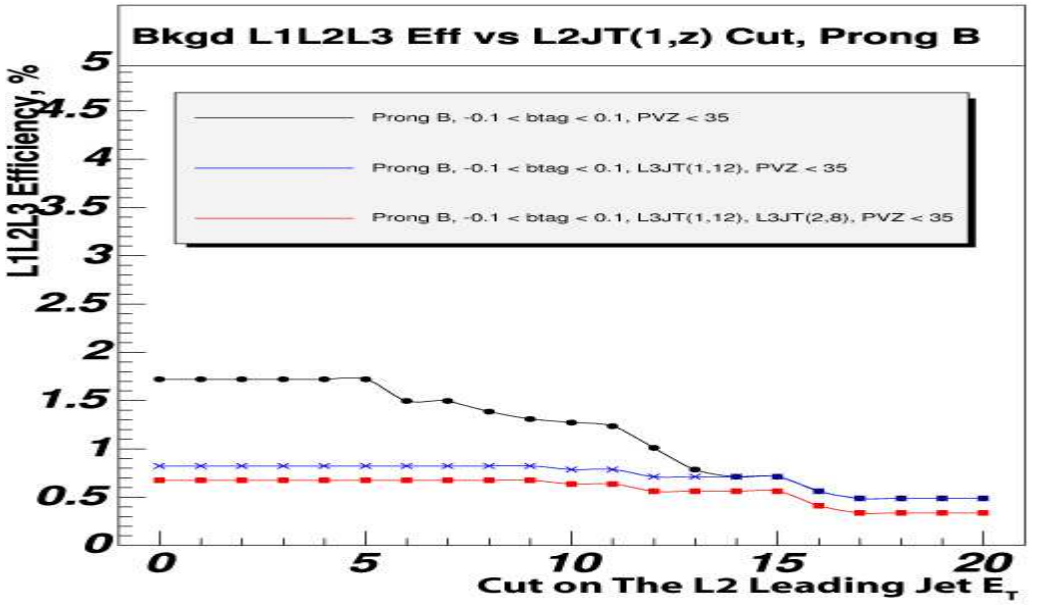

Figure 4.9: Background efficiency as a function of the cut on the jet E_T at Level 2. Black circles (upper line): b-tag constraint plus primary vertex cut applied at L3. Blue crosses (middle line): same as upper line, with an extra E_T cut on the leading L3 jet of 12 GeV. Red squares (bottom line): same as middle line with a cut of 8 GeV on the p_T of the second leading jet at L3.

For an IP tag probability of 0.1, the background efficiency is found to be 1%. The error on the efficiency measurements is of the order of ±0.1%.

Next, we impose cuts on the energy of the jets at L3. As the energy of the leading L3 jet increases (Figure 4.7), rejection (background efficiency) increases (decreases). By requiring one jet above 10 GeV the background efficiency is approximately 2%; this drops by a factor of 4 when we ask for a jet of 20 GeV. Cutting on the energy of the second leading jet at L3 provides additional background rejection as can be seen in Figure 4.8. Requiring two jets of 10 GeV reduces the background efficiency to about 1%.

Finally, Figure 4.9 plots the background efficiency as a function of the cut on the L2 jet energy. Asking for a more energetic jet at L2 improves background rejection as one would expect, but this L2 jet handle is not as powerful as imposing cuts on the L3 jet energies. Overall, the most powerful way to reject light-quark background is to cut hard on the b-tag event probability. Additional rejection can then be achieved by constraining the energy of the L3 jets. On top of this, the L2 jet energy threshold offers an extra, weaker, handle and is useful for requiring small extra improvements in background rejection. In the next section we shall see what impact these trigger conditions have on the signal efficiency.

4.5 Signal Efficiency

The signal efficiency studies (for this particular trigger) are summarised in Figures 4.10 to 4.13. Efficiency is quoted after events have passed all three trigger levels; 100% corresponds to all of the signal events in the sample. By comparing the efficiencies plotted in Figures 4.6 and 4.10, we can immediately see that the muon trigger under study - a single muon plus jet at L1, and a medium quality muon at L2 - is much more efficient for signal $Z \rightarrow b\overline{b}$ events than for background. Requiring a L3 event b-tag improves the discrimination between signal and background; it kills off both types of event but rejects background events more effectively than signal

events. As seen from Figure 4.10, for a cut on the b-tag probability of 0.1 the signal efficiency is 3% (compared to 1% for the background in Figure 4.6).

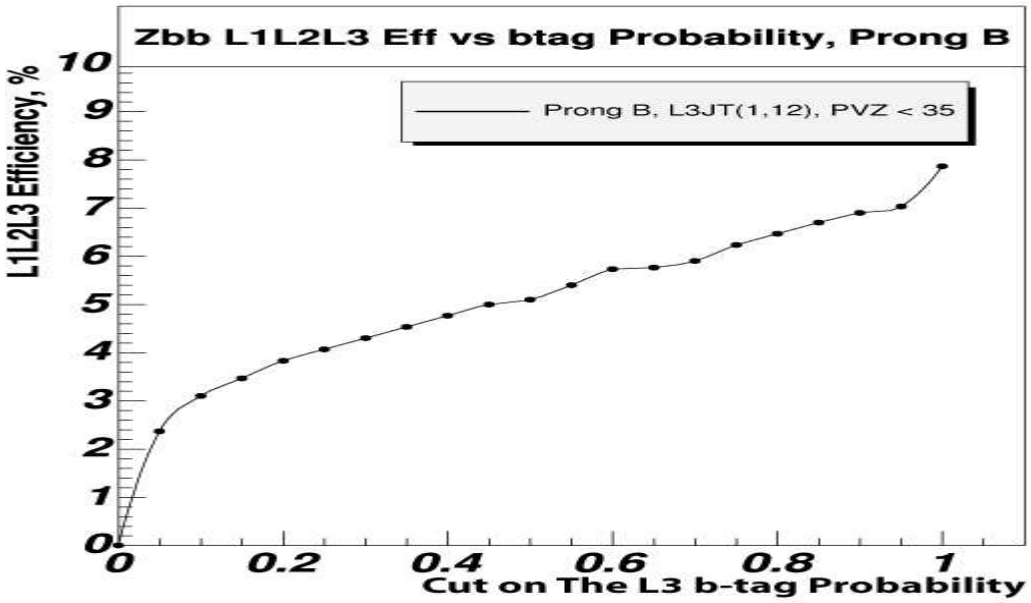

Figure 4.10: Signal efficiency as a function of L3 b-tag probability. The likelihood that the event is b-tagged increases as the probability tends to 0. Trigger combination applied here: one L2 jet above 6 GeV, one L3 jet above 12 GeV and an L3 primary vertex constraint of $|z| < 35$ cm.

Examination of Figure 4.11 reveals that constraining the energy of the leading L3 jet has little impact on the signal efficiency (having already applied an IP tag cut at L3). For leading L3 jet energies up to about 15 GeV, the signal efficiency remains flat at about 3%. Over this same range, however, the background efficiency drops by a factor of almost 4 (see Figure 4.7), demonstrating that the leading jet energy at L3 is a powerful discriminating variable. If we now require a second jet at L3, also of 15 GeV, the signal efficiency remains at about 3%, as observed in Figure 4.12. In contrast, asking for two L3 jets above 15 GeV yields a background efficiency of 0.5%.

Figure 4.13 shows that the signal efficiency is flat up to a L2 jet energy cut of about 7 GeV. Cutting beyond this value causes the efficiency begins to drop; it is therefore desirable to keep the L2 jet E_T threshold relatively low so as to preserve as much of the signal as possible. As we saw in Figure 4.12 (and again observe in

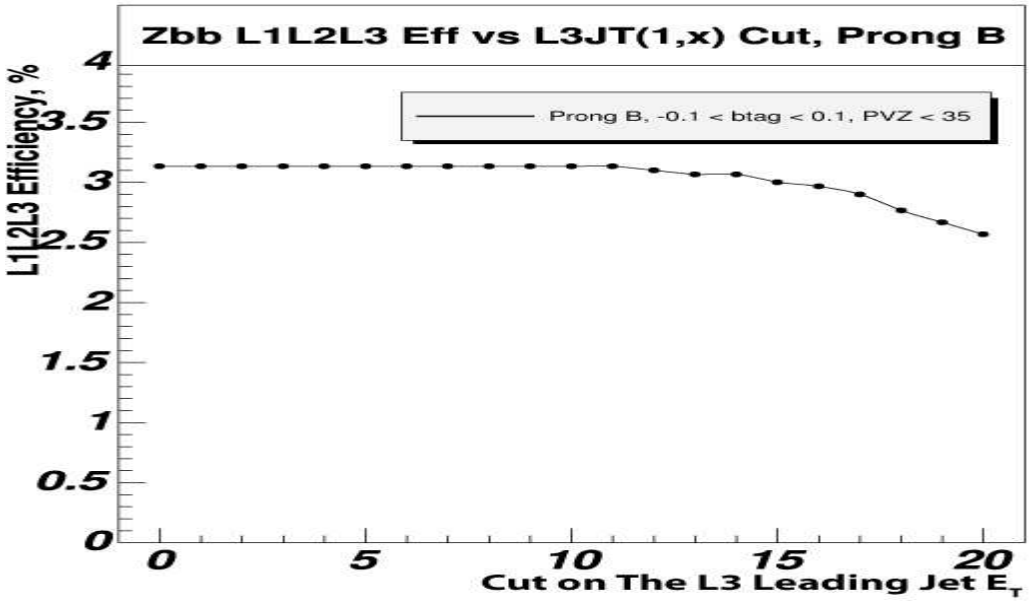

Figure 4.11: Signal efficiency as a function of leading jet E_T cut applied at Level 3. Trigger combination applied here: one L2 jet above 6 GeV, an L3 b-tag probability < 0.1 and an L3 primary vertex constraint of $|z| < 35$ cm.

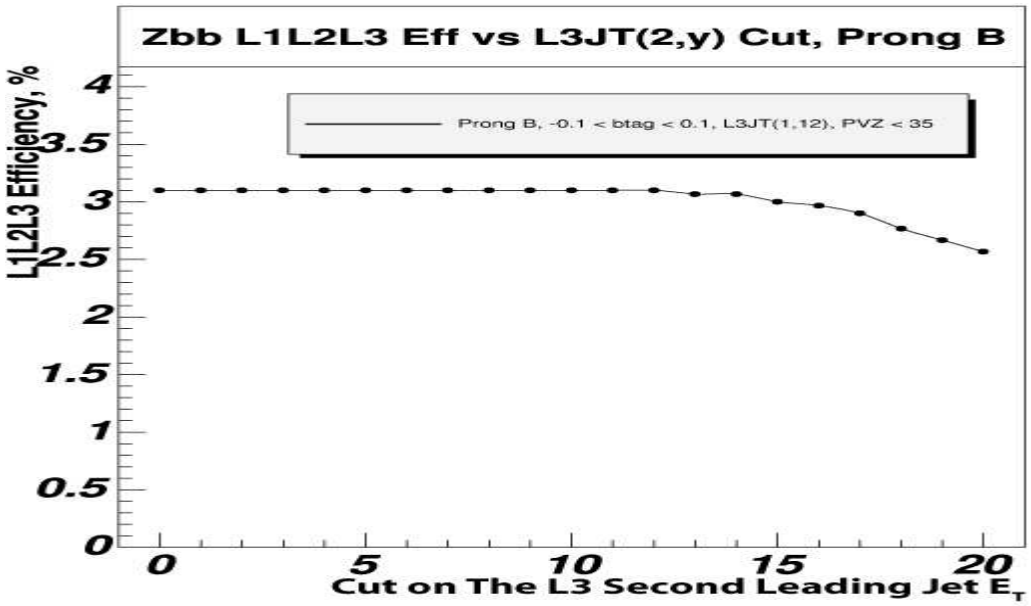

Figure 4.12: Signal efficiency as a function of second leading jet E_T cut applied at Level 3. Trigger combination applied here: one L2 jet above 6 GeV, one L3 jet above 12 GeV, an L3 b-tag probability < 0.1 and an L3 primary vertex constraint of $|z| < 35$ cm.

Figure 4.13), constraining the second leading jet energy at L3 has little effect on the signal efficiency (the two lines in Figure 4.13 are indistinguishable, within the 0.1%

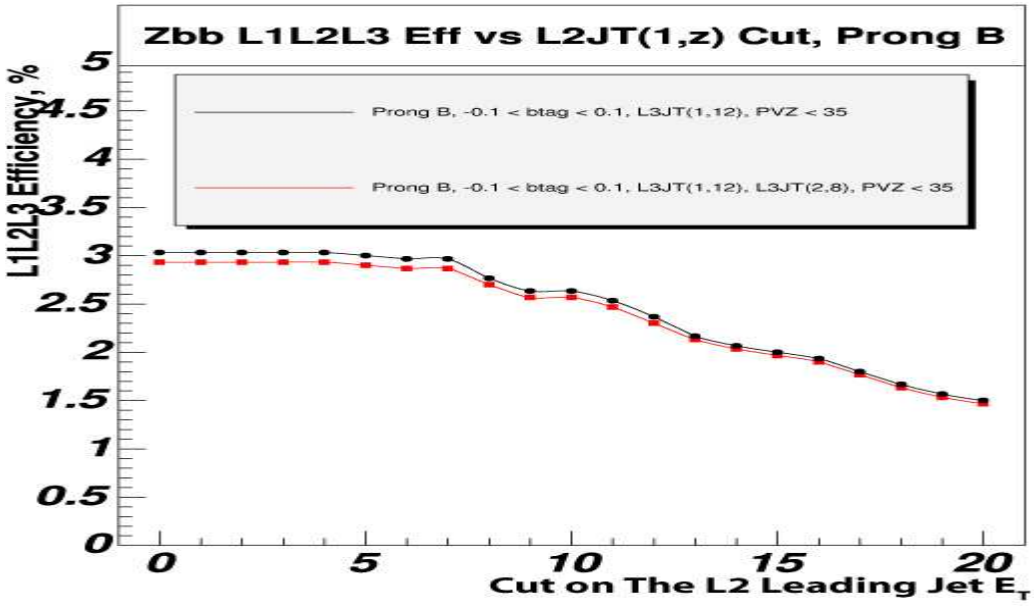

Figure 4.13: Signal efficiency as a function of jet E_T cut applied at Level 2. Black circles (upper line): b-tag constraint plus primary vertex cut applied at L3, with a cut on the leading L3 jet of 12 GeV. Red squares (lower line): same as upper line with an additional cut of 8 GeV on the second leading L3 jet.

error on the efficiency).

4.6 The Finalised $Z \to b\bar{b}$ Triggers

The final choice of triggers is a trade-off between the signal efficiency and the background rate. Figure 4.14 below illustrates the results of a process of optimisation (for one of the five final $Z \to b\bar{b}$ triggers). Each of our triggers was optimised in such a way as to reduce the rate to tape to 3–4 Hz overall (or ∼0.5 Hz for a given trigger) while maximising the signal efficiency. In order to achieve this, the cuts on the different event handles - for example b-tagging and jet energy at Level 3 and Level 2 - must be studied in detail, and in combination with one another.

For each trigger, we explored the parameter space systematically, scanning through the different trigger conditions one by one, seeing which combination gave the best efficiency (from signal MC) and rate (from data). The data were acquired during the special runs described in Section 4.3. The final result for one of the single muon plus jet triggers is shown in Figure 4.14; the process of optimisation was also performed for the other four $Z \to b\bar{b}$ triggers.

In the top right-hand corner of Figure 4.14, we impose a loose cut on the L3 b-tag event probability of 0.9, along with a constraint on the primary vertex ($|z| <$ 35 cm) and no cuts on the L3 or L2 jet energies. As the cut on the b-tag probability is gradually tightened under these conditions (see crosses) from 0.9 to 0.1, the rate (plotted on the x-axis) drops from 14 Hz to 4 Hz. Signal efficiency also roughly halves to about 3%.

From a tight b-tag cut of 0.1, we then impose an additional cut on the E_T of the leading jet at L3 (see results represented by the coloured circles). At this stage no cuts are placed on the second leading jet at L3 or on the L2 jets. Increasing the leading L3 jet E_T cut from 3 to 20 GeV decreases the background rate to about 2 Hz and the signal efficiency to 2%. Cutting harder than 12 GeV with this particular combination of trigger conditions simply hurts the signal efficiency and does nothing to improve the rate.

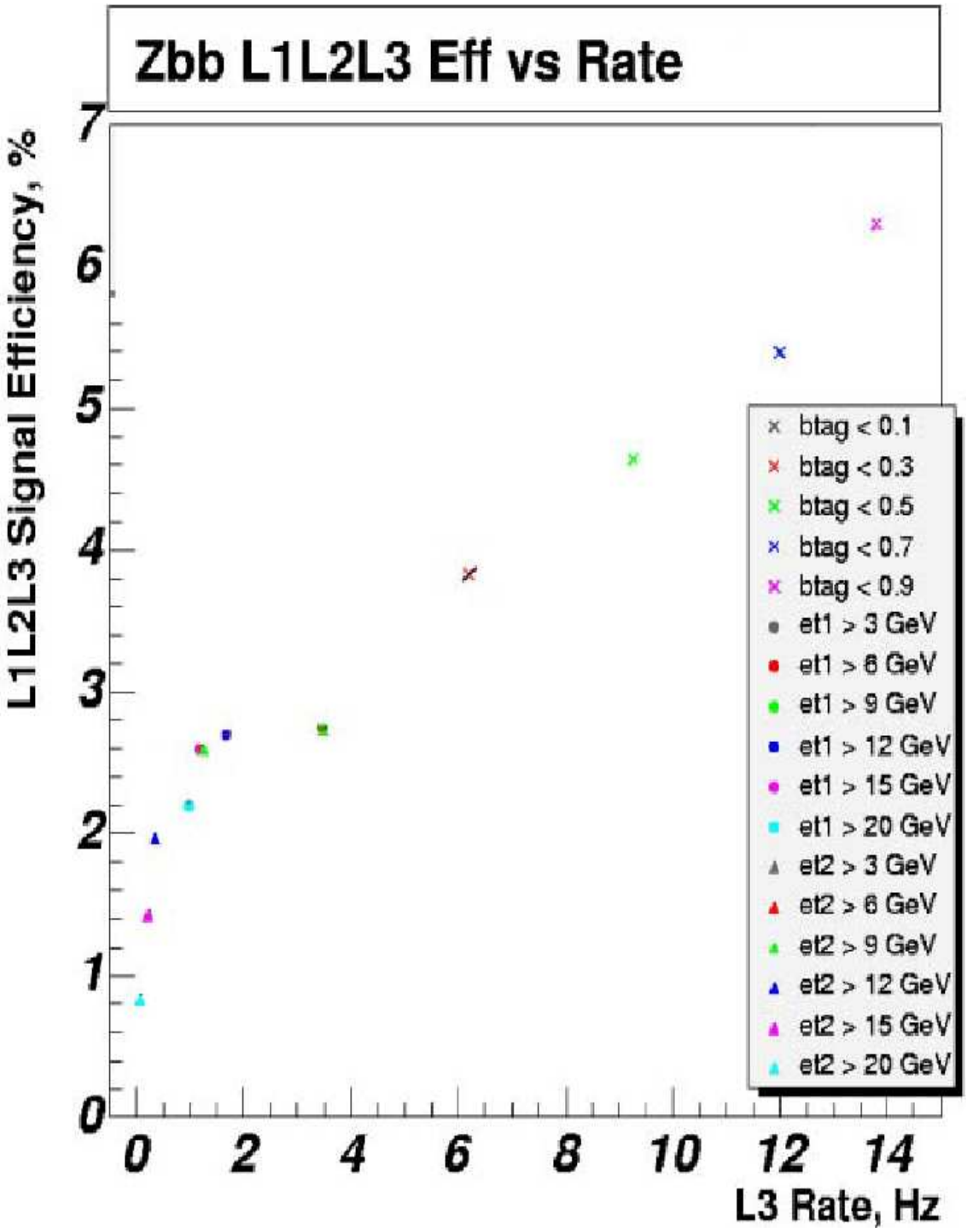

Figure 4.14: Signal efficiency as a function of background rate out of L3, for a single muon plus jet trigger at a luminosity of about 0.50×10^{32} cm^{-2}s^{-1}. Crosses, moving from top to bottom: cut on b-tag event probability is tightened. Circles, moving right to left: cut on leading jet E_T at L3 is gradually made more stringent. Triangles, top to bottom: cut on second leading jet E_T at L3 is systematically increased. As trigger conditions are tightened we move from the top right corner of the curve towards the bottom left corner.

If the leading jet energy at L3 is therefore then set at 12 GeV, and the E_T of the second leading jet at L3 is varied systematically, we obtain the results represented by the coloured triangles. By cutting on the second leading jet at L3 at 12 GeV, one obtains the additional rejection needed to reduce the rate to the required level of about 0.5 Hz (for a single trigger). For this particular trigger, the final configuration of b-tag < 0.1, two L3 jets above 12 GeV and a primary vertex cut of $|z| < 35$ cm yields a rate of approximately 0.5 Hz and a signal efficiency of 2.5%.

This is an example of the process of optimisation performed for each trigger, and is only one such result. It serves to provide an idea of the sorts of cuts that need to be made in order to obtain triggers which will successfully run online, and illustrates the effect of cuts on the trigger rate and efficiency as they are imposed in one particular sequence. Optimisation has been performed for all five of the $Z \to b\overline{b}$ triggers, and a full breakdown of the trigger terms is given in Section 4.6.1 below. The trigger rates are obtained from the online trigger database and shown in Table 4.2, for an instantaneous luminosity of 0.55×10^{32} cm^{-2}s^{-1}. The total output rate at L3 from all five triggers is between 3 and 4 Hz (given that there is overlap between them), which satisfies the bandwidth requirements of the experiment. Trigger rates and efficiencies for signal events are given in Section 4.7.

Trigger Name	**Trigger Rate (Hz)**		
	Level 1	**Level 2**	**Level 3**
ZBB_TLM3_2JBID_V	158.3	141.5	0.84
ZBB_TLM3_2LM0_2J	158.3	141.5	0.53
MUJ1_2JT12_LMB_V	40.1	33.2	1.02
MUJ2_2JT12_LMB_V	30.7	25.3	0.90
DMU1_JT12_TLM3	29.4	10.2	0.57

Table 4.2: $Z \to b\overline{b}$ trigger rates at an instantaneous luminosity of 0.55×10^{32} cm^{-2}s^{-1}.

4.6.1 Breakdown of The Triggers

Our trigger studies led us to the following set of $Z \rightarrow b\overline{b}$ triggers:

1. **ZBB_TLM3_2JBID_V:** Single muon trigger with a b-tag at L3.

   - At L1 the term `mu1pt2wtlx_TTK(1,3)` triggers on single muon objects in the wide ('w') region[4] of the detector that fulfill scintillator and wire conditions. A track with a p_T of at least 3 GeV/c is required.
   - At L2 the muon must be of at least "medium" quality. A muon is defined as medium if it produces at least two hits in the A layer wire chamber, at least one A layer scintillator hit, at least two BC layer wire hits and at least one BC scintillator hit (except for central muons with less than four BC wire hits). A scintillator timing cut in the A and BC layers is used to reject muons from cosmic radiation. No constraints are imposed upon the muon p_T or its location in the detector.
   - At L3 there must be at least one muon with $p_T > 3$ GeV/c, two jets of E_T above 12 GeV and at least one jet with a b-tag probability of 0.1 or less. A cut is also made on the z-coordinate of the primary vertex (PVZ): $|z| < 35$ cm.

[4] Wide refers to the CFT fiducial region.

2. **ZBB_TLM3_2LM0_2J:** Single muon trigger at L1, requiring two muons at L3 - in effect, a dimuon trigger.

   - At L1 the condition is as in trigger 1 (above).
   - At L2 the requirement is the same as for trigger 1.
   - At L3 all events should have at least one muon matched to its corresponding track in the central tracking system, with a $p_T > 3$ GeV/c. The event should also have a minimum of two "loose" quality muons (no p_T condition) and two jets of $E_T > 12$ GeV. A loose muon is defined as a medium muon (as described above) that fails one of the medium quality tests. For this purpose the A layer wire chamber and scintillator requirement are treated as one test and at least one scintillator hit is always required.

3. **MUJ1_2JT12_LMB_V OR MUJ2_2JT12_LMB_V:** These two muon plus jet triggers differ only by their L1 conditions. In practice they are combined into a single 'OR'd' combination within the v13 trigger list.

   - At L1, events must pass either the `mu1ptxatlx_CJT(2,3)` or `mu1ptxatlx_CJT(1,5)` trigger terms. These conditions involve muon scintillator and wire requirements and select single muons in the 'a' (all muon) region of the detector (that is, they can be located anywhere). The `CJT(2,3)` and `CJT(1,5)` terms ask for two calorimeter jet trigger towers above 3 GeV and one tower above 5 GeV, respectively.
   - At L2 the event must possess one or more medium muons; there is no p_T or region requirement. In addition, there must be at least one jet with $E_T > 8$ GeV.
   - The L3 condition involves at least two jets with $E_T > 12$ GeVand one loose muon with no p_T threshold. On top of this, we require one tight b-tag (with b-tag probability < 0.05) and a primary vertex cut of $|z| < 35$ cm.

4. **DMU1_JT12_TLM3:** Dimuon trigger.

   - At L1 the `mu2ptxatxx` term looks for dimuons in any region of the muon detector. This condition is based only on the muon scintillator readout.
   - At L2 events pass the trigger if they contain at least one medium quality muon; again no p_T or region criteria are imposed.
   - At L3 there must be at least one track-matched muon with $p_T > 3$ GeV/c and a single jet with transverse energy above 12 GeV (for which $|\eta| < 3.5$).

4.7 The v13 Dataset And The $Z \to b\bar{b}$ Analysis

The v13 $Z \to b\bar{b}$ triggers went online in June 2004 and ran for three months until the Tevatron was shut down. During this time each v13 trigger was exposed to between 50 and 62 pb^{-1} of integrated luminosity, which reduces to between 46 and 54 pb^{-1} after good run selection, that is, inclusion only of runs for which all subdetectors and luminosity blocks[5] were marked as "good" quality [52] (see Table 4.3). The collaboration could afford to keep the dimuon trigger completely unprescaled (since it has the lowest rate of all five triggers); this is why it was exposed to a larger integrated luminosity as listed in Table 4.3. The single-muon triggers were prescaled or turned off at the very highest luminosities around 0.60×10^{32} cm^{-2}s^{-1}, even though their individual rates fell within bandwidth constraints (as designed). In reality, this prescaling occurred because our triggers were grouped (within DØ's global trigger list) with other triggers whose rates were too high.

[5] A luminosity block represents the smallest unit of time in which luminosity is recorded.

v13 Trigger	Luminosity (pb^{-1})		
	Delivered	Recorded	Good
ZBB_TLM3_2JBID_V	68.9	49.7	45.9
ZBB_TLM3_2LM0_2J	68.9	49.7	45.9
MUJ1_2JT12_LMB_V	68.9	53.8	48.9
MUJ2_2JT12_LMB_V	68.9	51.6	47.4
DMU1_JT12_TLM3	68.9	62.0	54.2

Table 4.3: Delivered, recorded and good luminosity for the v13 $Z \to b\overline{b}$ triggers. 'Good' data excludes runs containing bad subdetector or luminosity information. The dimuon trigger was exposed to a larger integrated luminosity as it remained unprescaled. The single-muon triggers were prescaled or turned off at the very highest luminosities (0.60×10^{32} $cm^{-2}s^{-1}$ at this time).

Tables 4.4 and 4.5 provide performance data for the v13 triggers. The trigger rates of the most significant (i.e. the most frequently fired) v13 triggers are presented in Table 4.4. All three of the single muon-based triggers specifically designed for $Z \to b\overline{b}$ - MUJ1_2JT12_LMB_V, MUJ2_2JT12_LMB_V and ZBB_TLM3_2JBID_V - appear among these four leading triggers. The remaining trigger, MM1_JT25, is a B-physics trigger and has a higher rate of 2 Hz, making it susceptible to prescaling. Also presented in the final column of Table 4.4 is the signal candidate yield for each trigger. This signal yield consists of v13 data events that have passed both the relevant trigger and offline analysis cuts. (For details of these cuts see Section 5.4.1 in Chapter 5.)

v13 Trigger	Level 3 Trigger Rate at 0.60×10^{32} $cm^{-2}s^{-1}$ (Hz)	Signal Candidate Yield After Offline Cuts
MUJ1_2JT12_LMB_V	1.24	3741
MM1_JT25	2.09	2874
MUJ2_2JT12_LMB_V	1.09	3349
ZBB_TLM3_2JBID_V	0.95	2727

Table 4.4: Trigger rates and signal candidate yields in the v13 portion of the data, for the four leading v13 triggers. All three of the single muon-based triggers specifically designed for $Z \to b\overline{b}$ appear among these four leading triggers; MM1_JT25 is a B-physics trigger and has a higher rate.

v13 Trigger	L1L2L3 Trigger Efficiency (%)	
	Absolute	W.r.t. Offline Cuts
MUJ1_2JT12_LMB_V	3.3	11.1
MM1_JT25	3.8	11.8
MUJ2_2JT12_LMB_V	3.3	11.6
ZBB_TLM3_2JBID_V	2.7	9.3
OR of the above triggers	6.0	16.9

Table 4.5: v13 trigger efficiencies for MC signal events.

Table 4.5 provides efficiencies for each of these triggers, evaluated by passing $Z \rightarrow b\overline{b}$ MC events through a full trigger simulation (`d0trigsim`). Efficiencies are computed for each trigger individually and for their OR'd combination. The L1L2L3 pass rate is quoted both as an absolute number and as a fraction relative to the number of events passing offline cuts. Note that the absolute trigger efficiency for the MUJ1_2JT12_LMB_V trigger quoted above in Table 4.5 (3.3%) is larger than the value obtained in Section 4.6 (2.5%). The reason for this is that Table 4.5 was produced several months after the trigger design work of Section 4.6 was performed, and these later studies used a different Monte Carlo sample and an updated version of the trigger simulation package `d0trigsim`.

4.8 Summary

A set of five muon-based triggers have been designed to select $Z \rightarrow b\overline{b}$ events up to luminosities of 0.80×10^{32} cm^{-2}s^{-1}. These triggers employ muon selection, track constraints, jet conditions, primary vertex cuts and the Level 3 impact parameter tool in order to achieve the background rejection required. The combined rate to tape of this set of triggers is approximately 4 Hz, which satisfies the bandwidth constraints imposed by the collaboration. Absolute trigger efficiencies (for signal events passing Levels 1, 2 and 3) range from 1.4% for the dimuon trigger to 2.8% for a single muon trigger. Future upgrades to these triggers could make use of the Silicon Track Trigger at Level 2 in order to attain increased rejection at higher luminosities.

With these triggers in full use and a daily luminosity of 3 pb^{-1} delivered by the Tevatron (see Figure 2.4), we expect to collect per day approximately 300 candidate events against a background of a few thousand QCD events. The v14 trigger list, which ran online from December 2004 to March 2006 and was based upon the v13 triggers, was designed to cope with luminosities in excess of 0.80×10^{32} $\text{cm}^{-2}\text{s}^{-1}$. The v13 $Z \rightarrow b\bar{b}$ L3 conditions presented here remained the same in the v14 list, and these triggers now form the basis for definitive Run IIa publications.

Chapter 5

A Search For Z to $b\bar{b}$

"Everything is in a state of flux, including the status quo."

Robert Byrne

5.1 Overview

A search for the $Z \rightarrow b\bar{b}$ decay has been performed at DØ using the first 300 pb^{-1} of Run II data collected from June 2002 to August 2004. This chapter presents a description of the search strategy, the background subtraction techniques investigated and the results obtained.

5.2 Event Samples

5.2.1 The Data

Having carefully designed and implemented a set of $Z \rightarrow b\bar{b}$ triggers, as discussed in the previous chapter, ideally we would use the data collected with these triggers to search for a signal. However, at the time that a data cut-off was made for this analysis (the start of the autumn 2004 Tevatron shutdown), version 13 (v13) of the trigger list had only been running online for three months. As such the v13 data have limited statistics and correspond to an integrated luminosity of about 50.0 pb^{-1}. (See Table 4.3 in Chapter 4 for a detailed luminosity breakdown.) More

events are needed both to ensure statistical significance in the search and to model the background with sufficient precision. The analysis was therefore extended to incorporate data that was collected using trigger list versions older than v13 (known as 'pre-v13' data hereafter), corresponding to an integrated luminosity of approximately 300 pb^{-1}. Most of these events were obtained using version 12 (v12) of the trigger list, and the analysis described in this chapter will therefore concentrate largely on the pre-v13 sample.

The data originate from the pass2 "BID" skim, which is a dataset selected primarily for B-physics studies at DØ and contains events processed with version p14 (p14.05 or higher) of the reconstruction software [39]. The skim has the following properties:

- A "loose" offline reconstructed muon in each event with $p_T > 4$ GeV/c, matched within $dR < 0.7$ to a jet of cone radius 0.5. This requirement enhances the fraction of heavy-flavour events due to the decays of $b \to \mu$ and $b \to c \to \mu$;
- About 90 million events, corresponding to integrated luminosities of about 50 pb^{-1} and 300 pb^{-1} for the v13 and pre-v13 data, respectively.

A variety of selection criteria are imposed to ensure good data quality. Before an event in a given run can be fully incorporated into the signal search, we check to make sure that the DØ run quality database has flagged the run as 'good' for each of the subdetectors relevant to the analysis. For example, data may be flagged as 'bad' if a clear hardware problem is detected during a run. We also exclude runs that were not successfully processed, or special runs such as those collected with test trigger configurations. After applying this run quality selection we have:

- Only events contained in luminosity blocks labelled as "good";
- Runs with good calorimeter and jet/missing E_T response and no hot cells;

- Good quality muon information;
- Acceptable central-tracking information (from the SMT and CFT).

5.2.2 Monte Carlo

Various Monte Carlo (MC) samples were used in the analysis as listed in Table 5.1. Each MC sample was generated with `PYTHIA` [37], overlaid with an average of 0.8 minimum bias events, passed through the full `GEANT` [38] simulation of the detector and processed with version p14 of the reconstruction software. The events were produced partly on `SAMGrid`, the computational grid developed by Fermilab Computing Division and the DØ experiment, with strong UK involvement. The facilities at Imperial play a leading role in production activities.

Monte Carlo Sample	**p_T Cut Applied at Parton Level, GeV/c**	**Number of Events**
Signal		
$Z \to b\bar{b}$	None	82,000
Heavy-flavour backgrounds		
$b\bar{b}$	5–20	200,000
$b\bar{b}$	20–40	125,000
$b\bar{b}$	40–80	150,000
$b\bar{b}$	80–160	100,000
$b\bar{b}$	160–320	25,000
$b\bar{b}$	> 40	200,000
Light-quark (u,d,s) backgrounds		
$q\bar{q}$	5–20	200,000
$q\bar{q}$	20–40	125,000
$q\bar{q}$	40–80	150,000
$q\bar{q}$	80–160	100,000
$q\bar{q}$	160–320	25,000

Table 5.1: Summary of Monte Carlo samples used in the analysis. q refers to the light quarks u, d or s.

The data skim and MC samples were processed using either the `RASTA` [53] or `higgs_multijet` [54] roottuple-generating packages[1]. Jet energy scale corrections

[1]Both are analysis packages which produce roottuples containing events that have passed certain

were applied to all jets, including corrections for the semileptonic decay of b-jets, using version 5.3 of the jet energy correction software [44] [45]. No specific b-jet energy scale corrections were applied, as no officially approved corrections exist for these data.

Corrections were also applied to account for the differences between data and Monte Carlo. MC events need to be corrected so that they accurately reflect the response of the calorimeter, and jet energies must be smeared so as to fully match the jet energy resolution measured in data which is about 20-30% worse. In addition, the b-tagging efficiency in data is about 15% lower than in MC and this must be included in the simulated events by means of event weighting in terms of p_T and η. All of these corrections were implemented using the official DØ prescription [55] [56]. Modelling of the MC is improving but some residual differences will remain as this is the nature of analysis at a hadron-hadron collider.

desired criteria, in preparation for a ROOT-based analysis [26]. The event 'skims' created contain only the information necessary for the analysis and are therefore more manageable and useful than their larger parent datasets.

5.3 Triggers

From 2001 to June 2004 trigger list versions 8 to 12 ran online. These lists contain more than 60 different muon-based triggers of interest that were exposed to a luminosity of about 300 pb^{-1}. From these 60 different triggers, the leading muon triggers of the full data sample were identified - that is, the final event selection was imposed[2] and from these candidate events, we identified the "top" triggers that were fired most often. We then determined the minimum number of top triggers that, when combined in an OR'd term, would yield at least 95% of the candidate $Z \rightarrow b\overline{b}$ signal. In this way, we optimise the signal yield while minimising the amount of background noise events that filter through on insignificant triggers. Ultimately, the study revealed that for the v12 and v11 data a combination of the top three triggers was optimal. Including data from the older triggerlists (versions 8 to 10) adds very little statistics for a lot of effort as it is harder to model these early triggers, and the data quality was poor during these early runs. So we, along with many other analyses at DØ, decided to ignore the data collected with these older triggers.

The leading v12 and v11 triggers are described in Tables 5.2 and 5.3, respectively, in decreasing order of the frequency with which they were fired (from top to bottom in the tables). Also shown are the corresponding v12 and v11 trigger efficiencies, in Tables 5.4 and 5.5 respectively. (For comparison, the v13 trigger efficiencies are given in Table 4.5 of Chapter 4.) By comparing the v13, v12 and v11 trigger efficiencies we see that the v12 and v11 triggers are slightly more efficient than their v13 counterparts, which is as a result of the looser L3 conditions in the v12 and v11 triggers (in particular no b-tag or primary vertex requirements). However, these looser triggers have higher rates and therefore need to be prescaled at high luminosities. The tighter v13 criteria allow triggering without prescale at the higher

[2]Each event must contain two and only two jets both with $|\eta| < 2.5$ and $p_T > 15$ GeV/c. The primary vertex of the event must have more than two tracks associated with it and be located within ± 50 cm in the z-direction. Both jets must be offline b-tagged and separated by an angle larger than 2.75 radians. (See Section 5.4.1 for full details.)

instantaneous luminosities now being delivered and will prove valuable with a larger dataset.

The most frequently fired v12 trigger in data after offline event selection, MU_JT25_L2M0, was exposed to a good luminosity of 297.5 pb^{-1}. In order to simplify both the MC-data comparison and the analysis (in terms of dealing with the prescaling and overlap of triggers), all events in the pre-v13 data were selected using this single v12 trigger.

v12 Trigger	**Trigger Description**		
	Level 1	**Level 2**	**Level 3**
MU_JT25_L2M0	single muon + jet	$\geq$1 muon + $\geq$1 jet	$\geq$1 jet
MU_2TRK3_L2M0	single muon + jet	$\geq$1 muon	2 global tracks
MUW_W_L2M3_TRK10	single muon	$\geq$1 muon	1 global track

Table 5.2: Description of the three leading v12 muon triggers. Candidate signal events are required to pass MU_JT25_L2M0, which is the trigger that was most frequently fired in the pre-v13 data.

v11 Trigger	**Trigger Description**		
	Level 1	**Level 2**	**Level 3**
MU_JT20_L2M0	single muon + jet	$\geq$1 muon + $\geq$1 jet	$\geq$1 jet
MU_JT25_L2M0	single muon + jet	$\geq$1 muon + $\geq$1 jet	$\geq$1 jet
MUW_W_L2M3_TRK10	single muon	$\geq$1 muon	1 global track

Table 5.3: Description of the three leading v11 muon triggers. Candidate signal events are required to pass MU_JT25_L2M0, which is the trigger that was most frequently fired in the pre-v13 data..

v12 Trigger	**L1L2L3 Trigger Efficiency (%)**	
	Absolute	**W.r.t. Offline Cuts**
MU_JT25_L2M0	5.5	15.6
MU_2TRK3_L2M0	7.0	18.1
MUW_W_L2M3_TRK10	3.4	8.9
OR of the above 3 triggers	8.7	20.2

Table 5.4: v12 trigger efficiencies for MC signal events.

v11 Trigger	L1L2L3 Trigger Efficiency (%)	
	Absolute	W.r.t. Offline Cuts
MU_JT20_L2M0	7.4	18.3
MU_JT25_L2M0	5.5	15.6
MUW_W_L2M3_TRK10	3.4	8.9
OR of the above 3 triggers	8.4	19.7

Table 5.5: v11 trigger efficiencies for MC signal events.

5.4 Event Selection

There are few kinematic handles with which to discriminate between the $Z \rightarrow b\overline{b}$ signal and the QCD $b\overline{b}$ background. For a given jet p_T, one would expect the two leading jets to be somewhat more back-to-back in $Z \rightarrow b\overline{b}$ events than in the QCD background, due to the increased colour processes in QCD. In QCD there is a colour connection between the initial and final states that does not exist for the $Z \rightarrow b\overline{b}$ events, and hence the presence of more gluon radiation in the QCD processes.

The two most powerful variables, besides the invariant dijet mass, are the angular separation of the two leading b-jets, $\Delta\varphi$ (plotted in Figure 5.1), and the number of jets in the event, n_{jet}. Figure 5.1 shows that signal events are slightly more back-to-back than the background events. Optimisation of these cuts is summarised in Figures 5.2 and 5.3 and is discussed in the following pages.

5.4.1 Analysis Cuts

With this in mind, candidate events were selected using the following offline prescription:

Cut 1 Trigger selection: MU_JT25_L2M0 (the trigger that was fired most frequently in the pre-v13 dataset).

Cut 2 The event must contain two and only two good quality jets and at least one

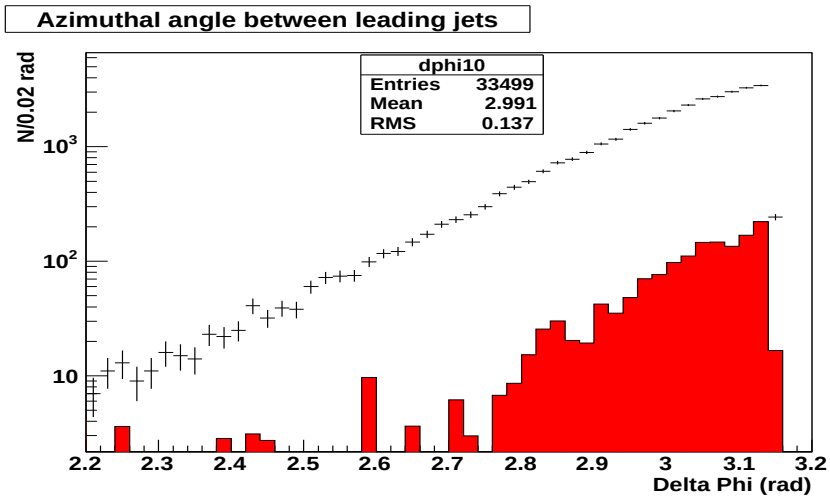

Figure 5.1: Comparison of the angular dijet distribution (delta phi or $\Delta\varphi$) between pre-v13 data and $Z \rightarrow b\overline{b}$ MC, after passing offline cuts 1–6. Red (dark grey) histogram: MC signal; black points: data. The signal is slightly more back-to-back than the background.

loose quality[3] offline muon. The $n_{jet} = 2$ cut provides the largest signal significance, as shown in Figure 5.2. (Details of how the significance is calculated are discussed later.)

Cut 3 The two jets must both have $|\eta| < 2.5$, and a $p_T > 15$ GeV/c after applying the jet energy scale.

Cut 4 For b-tagging purposes, both jets must be taggable. The definition of taggability involves requirements on the track and hit information in each event, and provides a sample of stable jets with a much reduced dependence on daily detector conditions.

Calorimeter jets are said to be 'taggable' if they are matched (within a cone of radius $\Delta R < 0.5$) to a reconstructed track-jet object, i.e. a jet made from charged tracks. The track-jet must satisfy the following conditions:

- the track p_T of every track in the track-jet is larger than 0.5 GeV/c;

[3]As discussed in Chapter 4, a loose muon is defined as a medium muon that fails one of the medium quality tests. A medium muon has to produce at the very minimum two hits in the A layer wire chamber, one A layer scintillator hit, two BC layer wire hits and one BC scintillator hit.

- each track that makes up the track-jet must have at least one SMT hit;
- at least one track within the track-jet object has $p_T > 1$ GeV/c;
- the track-jet cone size ΔR is smaller than 0.5;
- each track in the track-jet must have an impact parameter (with respect to the track-jet axis) in the $x - y$ plane that is less than 0.2 cm;
- each track in the track-jet must have an impact parameter (with respect to the track-jet axis) in the z plane that is smaller than 0.4 cm.

Cut 5 The primary vertex of the event must have more than two tracks attached to it and be located within $\pm$50 cm in the z-direction.

Cut 6 The two jets must both be loose SVT-tagged according to standard p14 DØ definitions. The SVT, or secondary vertex tagger [57], is one of DØ's offline b-tagging algorithms. It attempts to identify the location (or 'vertex') at which the b-hadron (or a daughter c-hadron) decayed by using the high impact parameter tracks and finding a common point where they intersect. A "loose" SVT b-tag provides the highest b-tagging efficiency; in data the tagging efficiency is 45% per jet for a mistag rate (i.e. fraction of light quarks that are incorrectly b-tagged) of 1%.

Two loose b-tags are required in each event in order to reject the $Z \rightarrow j\overline{j}$ background (where j represents any light quark). However, the b-tags remain loose so that signal events are not thrown away unnecessarily; tightening the b-tag criteria will not help to reject the remaining background which consists of $b\overline{b}$ QCD events.

Cut 7 The two b-jets must be strongly back-to-back, i.e. $\Delta\varphi > 2.75$ radians. This cut is chosen, from Figure 5.3, to yield maximum signal significance (details of how the significance is calculated are discussed later).

5.4.2 Signal Significance Studies

The aim is to optimise the expected signal significance (i.e. relative size of the $Z \to b\overline{b}$ signal), so as to have a chance of observing a $Z \to b\overline{b}$ peak. After triggering and requiring a double offline b-tag in the data (cut 6) virtually all of the light-quark QCD background is rejected. However, a large heavy-flavour component remains that still swamps the signal: S:S+B (where S and B are signal and background event counts respectively) is of the order of 1:23. By restricting the number of jets and the angle between the two b-jets (i.e. by applying cuts 2 and 7 respectively), the signal significance can be improved. We have investigated the effect of these two cuts on the effective signal significance, where effective significance is defined by the following expression:

$$\text{Effective Significance} = \frac{N_{signal}}{\sigma_{bkg}^{stat} \oplus \sigma_{bkg}^{syst} \oplus \sqrt{N_{tot}}}. \tag{5.1}$$

Here N_{signal} is the number of MC signal (double b-tagged) events passing the analysis cuts, weighted by cross-section and luminosity. N_{tot} is the total number of events in data passing the same cuts. They are related by the equation $N_{tot} = N_{signal} + N_{bkg}$, where N_{bkg} is the estimated number of background events that pass the cuts. The key to this analysis is to obtain an accurate value for N_{bkg}, and to carefully understand and minimise the error on its value.

In expression 5.1, σ_{bkg}^{stat} and σ_{bkg}^{syst} are, respectively, the statistical and systematic errors on the estimated number of background events passing all cuts. In what follows of Section 5.4, $\sqrt{N_{tot} - N_{signal}}$ is used as a conservative estimate of the *size* of the statistical error on the background estimate. In the actual analysis (see Section 5.5 onwards), the expected background is modelled from a separate and larger data sample, the single b-tagged events, and the resulting statistical error from this sample is used instead.

As we shall see, however, σ_{bkg}^{syst} is the limiting factor to our signal sensitivity. It is therefore important to obtain as small a value for σ_{bkg}^{syst} as is possible. Our best

estimate of the systematic error is 1.8%. A full description of the systematic error calculation is presented in Section 5.6.5.

Figure 5.2 shows the variation of effective signal significance with the cut on the number of jets in the event, and indicates that restricting the number of jets to exactly two provides optimal significance. Requiring two and only two jets desirably cleans up the signal by restricting the amount of radiation between the jets.

In Figure 5.1 we compare the azimuthal angle between the two jets for signal and data, after applying cuts 1–6 and accounting for the trigger efficiency and the integrated luminosity of 297.5 pb^{-1}. The signal:(signal+background) ratio is 1:23 and, as expected, the jets in $Z \rightarrow b\overline{b}$ are slightly more back-to-back than in the background.

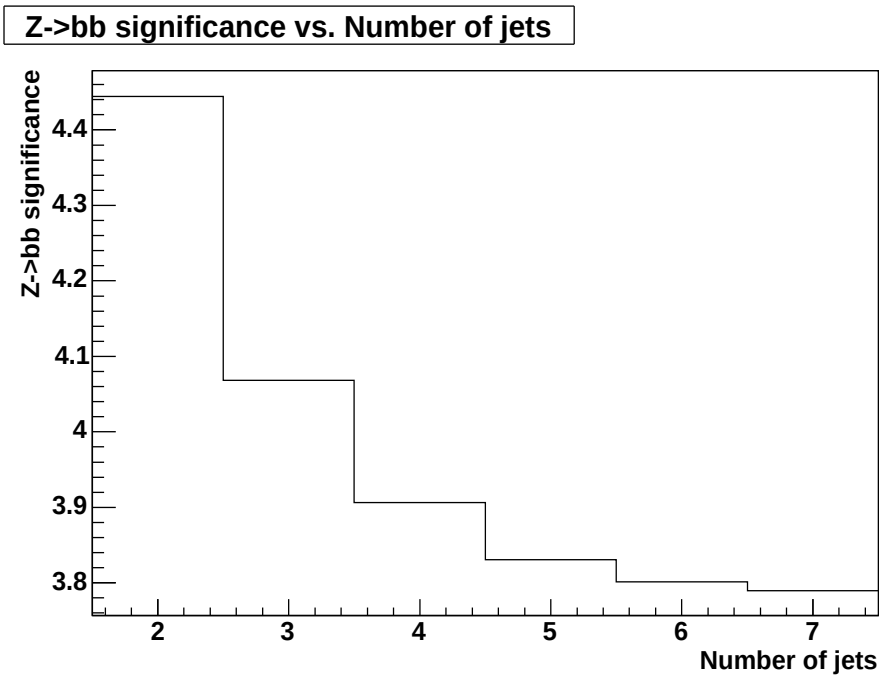

Figure 5.2: Effective signal significance, before cut 7 (the $\Delta\varphi$ requirement), as a function of the cut on the number of good jets in the event (n_{jet}) in the pre-v13 data. The systematic error on the number of background events was set to 1% for the purposes of illustration. Maximum significance is obtained in events with two and only two jets.

Effective significance is plotted as a function of $\Delta\varphi$ cut in Figure 5.3, applying different values for the systematic error on the background. Taking into account

the trigger efficiency and integrated luminosity, a significance of 4 is obtained with a cut of $\Delta\varphi > 2.75$ radians and a background systematic uncertainty of 1% (again, see Section 5.6.5 for a discussion of background uncertainties). Up to this point, no invariant mass cut has been applied. Since signal events are expected to be concentrated in an invariant mass window around the Z-boson mass (see Figure 5.4), such a cut around the region of interest can be expected to enhance the significance of the signal further. It is therefore surmised that an excess of $Z \rightarrow b\overline{b}$ events of the order of 4 standard deviations above the background may already be observable in the pre-v13 data sample, provided that the background can be estimated with sufficient precision.

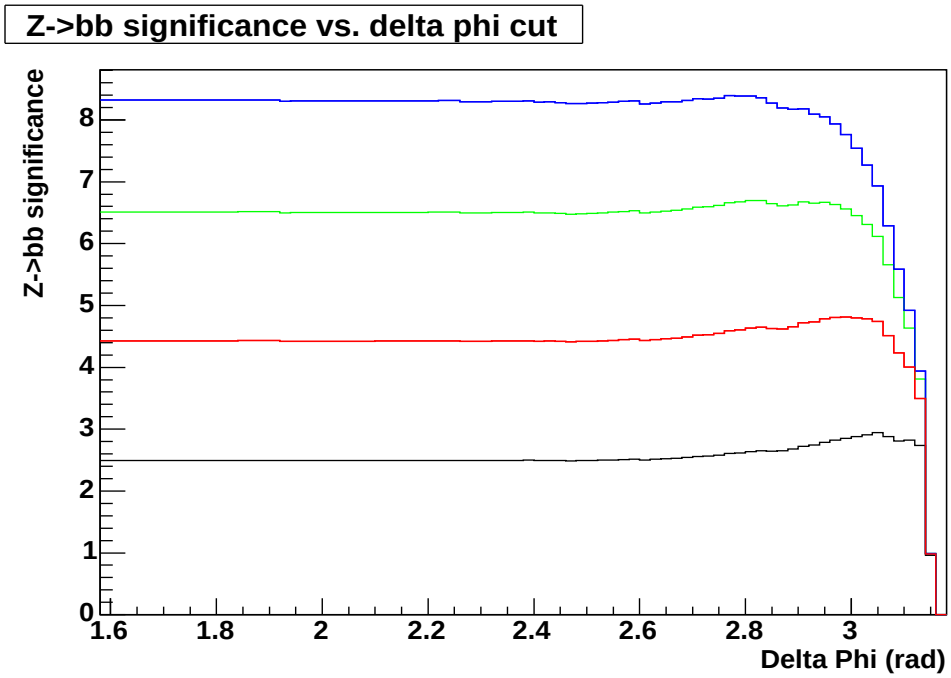

Figure 5.3: Effective signal significance as a function of $\Delta\varphi$ cut in pre-v13 data, for a systematic error of 0% (blue (top line)), 0.5% (green (second line down)), 1% (red (third line down)) and 2% (black (bottom line)) on the number of background events. The dependence on $\Delta\varphi$ is weak and a loose cut of 2.75 is applied to the pre-v13 analysis.

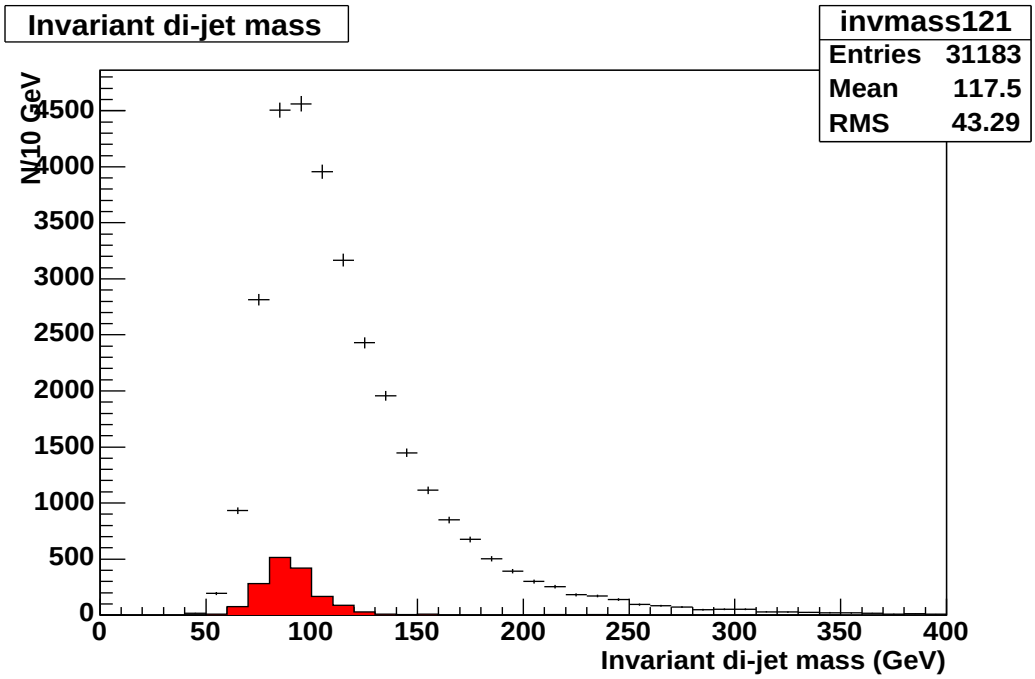

Figure 5.4: Comparison of the invariant di-b-jet mass in data and MC after event selection. Black points: pre-v13 data; red (grey) shading: expected $Z \to b\overline{b}$ signal from MC. The region above 120 GeV/c^2 is almost signal-free.

5.4.3 Cut Flow Results

Pre-v13 Dataset

Tables 5.6 and 5.7 show the number of events passing each analysis cut in signal MC and data, for the pre-v13 dataset. All events are required to pass the v12 trigger MU_JT25_L2M0, which was exposed to a good luminosity of 297.5 pb^{-1}. Monte Carlo event counts are weighted by cross-section and luminosity.

Analysis Cut	No. Signal MC Events Passing Cut	% of Total Events Passing Cut	% of Triggered Events Passing Cut
No selection	336500 ± 1300	100	\
1 (MU_JT25_L2M0)	18430 ± 310	5.5	100
2	10480 ± 230	3.1	56.8
3	8600 ± 210	2.4	46.6
4	7400 ± 200	2.1	40.1
5	7110 ± 190	2.0	38.5
6	1658 ± 92	0.4	9.0
7	1612 ± 91	0.4	8.7

Table 5.6: Cut flow statistics for $Z \rightarrow b\bar{b}$ Monte Carlo events passing the leading pre-v13 trigger, MU_JT25_L2M0. Event counts are weighted by cross-section and luminosity; the errors are statistical. The last two columns present the fraction of total and triggered events passing each cut.

Analysis Cut	No. Data Events Passing Cut	% of Triggered Events Passing Cut
1 (MU_JT25_L2M0 trigger)	10883000	100
2	5135700	47.2
3	4030900	37.0
4	2726900	25.1
5	2698500	24.8
6	33499	0.3
7	31183	0.3

Table 5.7: Cut flow statistics for events in data passing the leading pre-v13 trigger, MU_JT25_L2M0. The final column presents the fraction of triggered events passing each cut.

v13 Dataset

Tables 5.8 and 5.9 show the number of events passing each analysis cut in signal MC and data, for the v13 dataset[4]. In this instance, all events were selected exclusively from the v13 trigger MUJ1_2JT12_LMB_V, which was exposed to a good luminosity of 48.9 pb^{-1} (see Table 4.3 in Chapter 4 for more details). Monte Carlo event counts are weighted by cross-section and luminosity.

Analysis Cut	No. Signal MC Events Passing Cut	% of Total Events Passing Cut	% of Triggered Events Passing Cut
No selection	55200 ± 190	100	\
1 (MUJ1_2JT12_LMB_V trigger)	1814 ± 36	2.5	100
2	1012 ± 26	1.8	55.8
3	784 ± 23	1.4	43.2
4	746 ± 22	1.4	41.1
5	716 ± 22	1.3	39.5
6	183 ± 11	0.3	10.1
7 ($\Delta\phi > 3.0$)	120 ± 10	0.2	6.6

Table 5.8: Cut flow statistics for $Z \rightarrow b\overline{b}$ Monte Carlo events passing the leading v13 trigger, MUJ1_2JT12_LMB_V. Event counts are weighted by cross-section and luminosity; the errors are statistical. The last two columns present the fraction of total and triggered events passing each cut.

From Tables 5.6 (pre-v13) and 5.8 (v13), we see that the v12 trigger (MU_JT25_L2M0) is more efficient for signal than the leading v13 trigger (MUJ1_2JT12_LMB_V). However, at higher luminosities the v12 trigger was significantly prescaled, while the v13 trigger - which is designed to operate at high luminosities - remained unprescaled.

A comparison of Tables 5.7 (pre-v13) and 5.9 (v13) reveals that a larger proportion of events pass the offline criteria in the v13 dataset than in the pre-v13 data. This is despite the fact that the v13 cut flow numbers were obtained using a tighter $\Delta\phi$ cut (> 3.0 radians as opposed to > 2.75), which will kill off more of the signal.Overall, the v13 triggers do a better job of selecting candidate signal

[4]Cut 7 (the $\Delta\varphi$ cut) is slightly tighter here and set to 3.0 radians instead of 2.75.

Analysis Cut	No. Data Events Passing Cut	% of Triggered Events Passing Cut
1 (MUJ1_2JT12_LMB_V trigger)	536200	100
2	259700	48.4
3	218000	40.4
4	179700	33.5
5	177500	33.1
6	7409	1.4
7 ($\Delta\phi > 3.0$)	3741	0.7

Table 5.9: Cut flow statistics for events in data passing the leading v13 trigger, MUJ1_2JT12_LMB_V. The final column presents the fraction of triggered events passing each cut. Note that the fraction of events passing the offline criteria in the v13 data is larger. This suggests that the v13 triggers do a better job of selecting candidate signal events.

events. While the leading v13 trigger lets through slightly more data events than the older pre-v13 trigger, the overall signal acceptance - which is the product of signal efficiency and integrated luminosity - is higher for the new trigger which can run unprescaled at higher luminosities.

Unfortunately, the small v13 sample has much lower statistics than the pre-v13 data and possesses new triggers with different systematics, which at this time makes it difficult to extract a $Z \rightarrow b\overline{b}$ signal of any significance from this data. In the near future, however, it will be possible to take full advantage of a several times larger data sample that has now been collected with these new $Z \rightarrow b\overline{b}$ triggers, and to exploit the potential of a significantly larger signal.

5.5 Background Philosophy

Understanding the background to the $Z \rightarrow b\overline{b}$ signal in the double b-tagged data sample is crucial to this analysis. The background is composed almost entirely of heavy-flavour dijet production and mistagged gluon/light-quark jet production, none of which can be accurately simulated using current techniques. Thus the double tagged background must be derived from data, using either single tagged (and/or untagged) events. Once the background shape is well understood, it can then be subtracted from the data with confidence. In the BID skim data, the $b\overline{b}$/light-quark fraction is about 10% after imposing a single b-tag requirement. After the additional muon and trigger selection (cuts 1 and 2) the $b\overline{b}$/light fraction becomes about 20% and after requiring a double offline b-tag in the data (cut 6) the light-quark QCD background component is reduced to about 10% of the sample.

There are two steps to estimating the doubly-tagged background:

1. A background template is formed from single b-tagged candidate signal events in data;

2. This single tagged template is then scaled by an appropriate "tag ratio", which is the fraction of double b-tags to single b-tags in the data sample. The tag ratio is basically the probability to b-tag a jet. The resulting weighted distribution corresponds to an estimate of the double tagged background that is masking the $Z \rightarrow b\overline{b}$ signal.

The tag ratio depends on various event quantities such as the number of jets, the reconstructed invariant mass, jet p_T and jet η. When parametrised as a function of one or more of these variables, the tag ratio becomes known as a "tag rate function" or "TRF", and the TRF is used to weight each singly-tagged event. Examples of TRFs are shown in Figures 5.5 to 5.7, which illustrate how the tag ratio varies with jet p_T and η. As can be seen from the distributions, the fraction of jets tagged

changes slightly as a function of $|\eta|$: it is higher in the central region and lower in the forward detector regions.

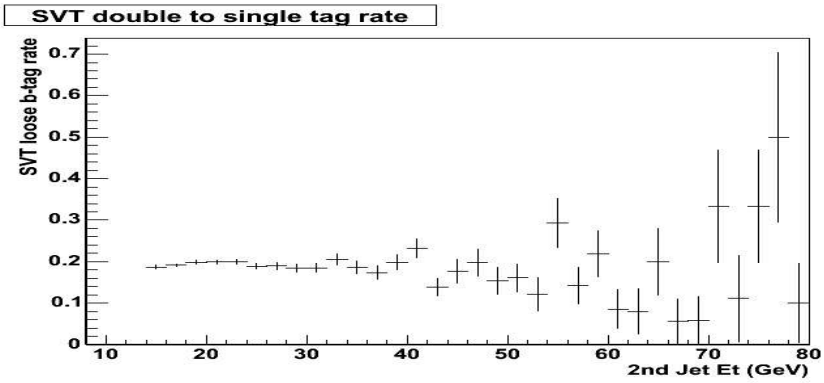

Figure 5.5: Tag ratio as a function of the second leading jet p_T for jets in the central region of the detector ($|\eta| < 1.1$), measured from pre-v13 data.

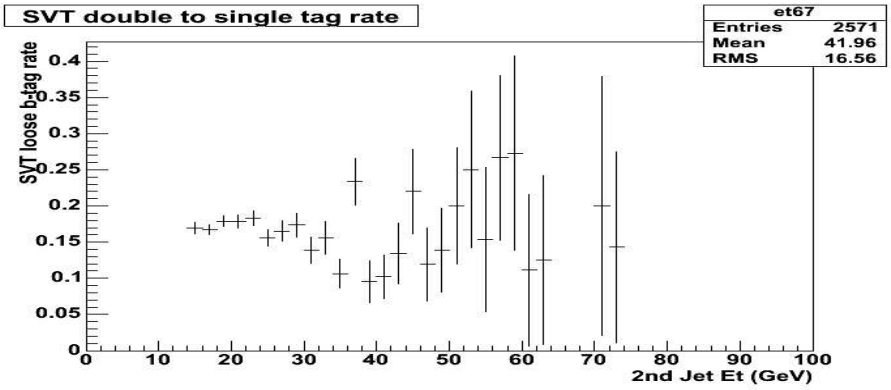

Figure 5.6: Tag ratio as a function of the second leading jet p_T for jets in the medium region of the detector ($1.1 < |\eta| < 1.5$), measured from pre-v13 data.

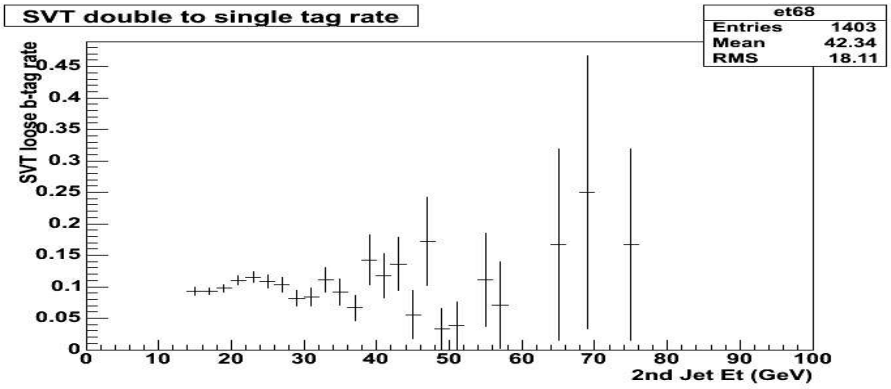

Figure 5.7: Tag ratio as a function of second leading jet p_T for jets in the forward region of the detector ($1.5 < |\eta| < 2.5$), measured from pre-v13 data.

The TRF weighting can be applied on an event-by-event basis to the final invariant mass distribution (the mass peak of interest), or at an earlier stage, for example at the jet level. The resulting scaled dijet mass spectrum is an estimate of the number of double b-tagged background events that enter our candidate signal sample. This calculated background is then subtracted from the final mass peak observed. After subtraction, provided that the number of events occupying the sideband regions is consistent with zero, an excess around the mass of the Z constitutes evidence for a signal.

While this is the basic premise underlying the modelling of the background, the technique can be implemented in various ways. As the analysis has proceeded, our approach has evolved. In the following sections I will describe and motivate this evolution and in Section 5.6.5 I will present the results of the final background subtraction.

5.6 Background Subtraction

5.6.1 I: The Concept of Signal And Background "Zones"

A convenient starting point to this analysis was the strategy and method used by the CDF $Z \rightarrow b\overline{b}$ analysis in Run I [58]. One can attempt to estimate the background by defining two regions or "zones" in $\Delta\varphi$ space:

1. "In-zone": a region rich in signal. These events pass cuts 1–5 and cut 7 (as outlined in Section 5.4). Cut 7, the requirement that $\Delta\varphi > 2.75$ radians, ensures a more back-to-back topology in the event.

2. "Out-of-zone": a background-enriched region. Events only pass cuts 1–5. They fail the $\Delta\varphi$ criterion, in other words $\Delta\varphi \leq 2.75$ in these events.

The data are then further divided into a double b-tagged sample (by asking for two loose SVT b-tags, cut 6) and a single b-tagged sample (by requiring only one loose SVT b-tag). There are thus four types of events:

- In-zone, double tagged: Total number of events = N_{in}^{++}
- In-zone, single tagged: Total number of events = N_{in}^{+}
- Out-of-zone, double tagged: Total number of events = N_{out}^{++}
- Out-of-zone, single tagged: Total number of events = N_{out}^{+}

In the signal-enhanced region (in-zone), N_{in}^{++} is an admixture of genuine signal events plus 'fake' double b-tagged background events. These background double tagged events need to be subtracted to reveal a signal. In order to estimate the doubly-tagged background, which we call $(N_{in}^{++})_{exp}^{bkg}$, we calculate the tag ratio of double to single b-tags out-of-zone, i.e. $(N_{out}^{++})_{obs}/(N_{out}^{+})_{obs}$. (Here the '*exp*' and '*obs*' subscripts stand for 'expected' and 'observed' respectively.) This ratio is then used to scale the invariant mass distribution of single tagged in-zone events. In other words, the double tagged background in each invariant mass bin is computed using the following equation:

$$(N_{in}^{++})_{exp}^{bkg} = (N_{in}^{+})_{obs} \text{ x } \frac{(N_{out}^{++})_{obs}}{(N_{out}^{+})_{obs}}. \tag{5.2}$$

$(N_{in}^{++})_{exp}^{bkg}$ is subtracted bin-by-bin from the invariant mass spectrum obtained after applying all analysis cuts (cuts 1–7).

Underpinning this method is the assumption that it is valid to extrapolate a TRF measured outside the signal zone into the signal zone. This in turn assumes that the TRF is independent of the choice of zone, that is, of the choice of $\Delta\varphi$ cut. The validity of this assumption is considered in Section 5.6.2. Furthermore, signal events that might appear out-of-zone have been neglected, resulting in a somewhat conservative signal estimate. In reality, a small amount of $Z \to b\bar{b}$ events will have $\Delta\varphi \leq 2.75$ and therefore satisfy the out-of-zone condition (of the order of 2% of events, from Figure 5.1).

Figure 5.8 plots the invariant di-b-jet mass obtained in the pre-v13 data, along with the expected signal from MC and the background calculated using the above method. An excess around the mass of the Z can be seen, but it is clear that the background shape is not modelled well at high masses. In the sidebands the data points lie consistently above the background estimate, which implies that the amount of background is being underestimated. The excess of events observed is thus likely to be an overestimate.

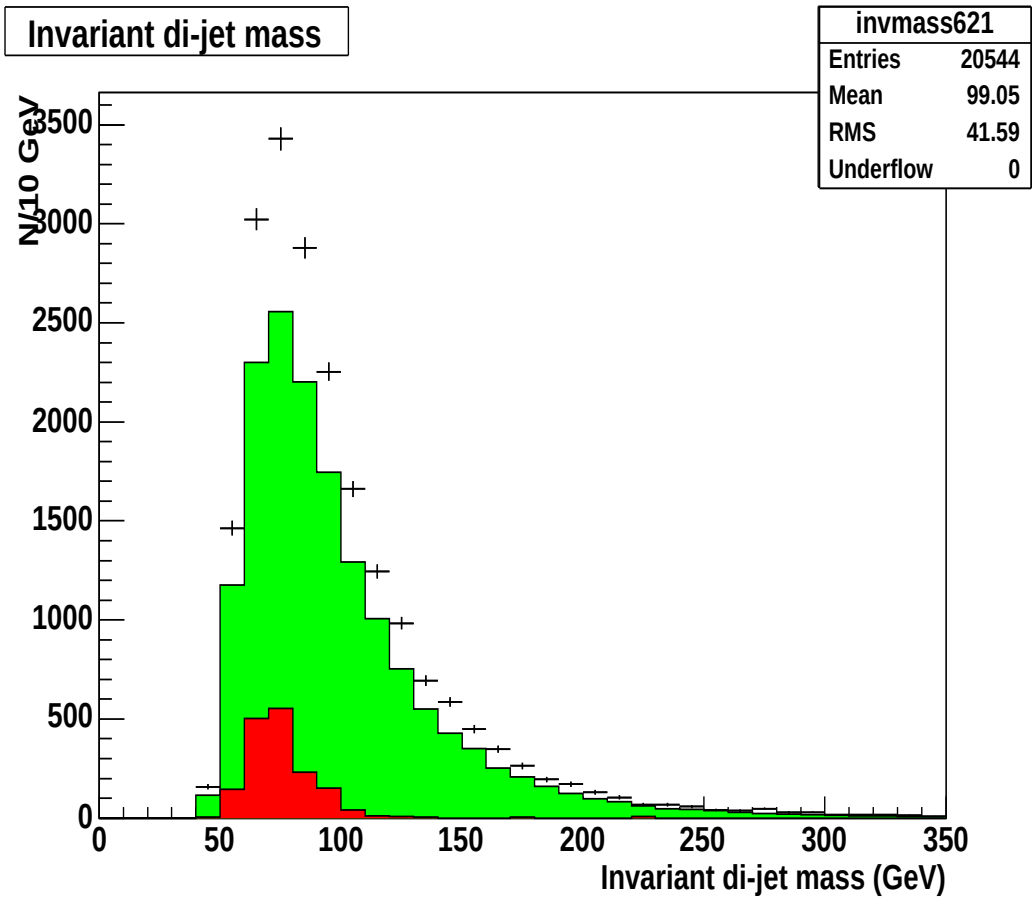

Figure 5.8: Invariant dijet mass in the pre-v13 data *before* background subtraction. Green (light grey) shaded histogram: expected background, estimated using the invariant mass-based TRF described in equation 5.2. Black points: total dijet mass distribution observed in pre-v13 data. Red (dark grey) shaded histogram: expected $Z \rightarrow b\overline{b}$ signal from MC, weighted by cross-section and luminosity.

5.6.2 II: Correcting For The Zone Dependency of The TRF

Up to this point, it has been assumed that the ratio of double to single tags outside the signal zone is independent of where that zone is defined, i.e. it is independent of the particular $\Delta\varphi$ value chosen to differentiate signal from background. However, Figure 5.9, which displays the double to single tag ratio as a function of $\Delta\varphi$, suggests that a linear dependence exists. Similar behaviour of the TRF is observed in Monte Carlo. If we do not take this effect into account, the background will not be modelled accurately.

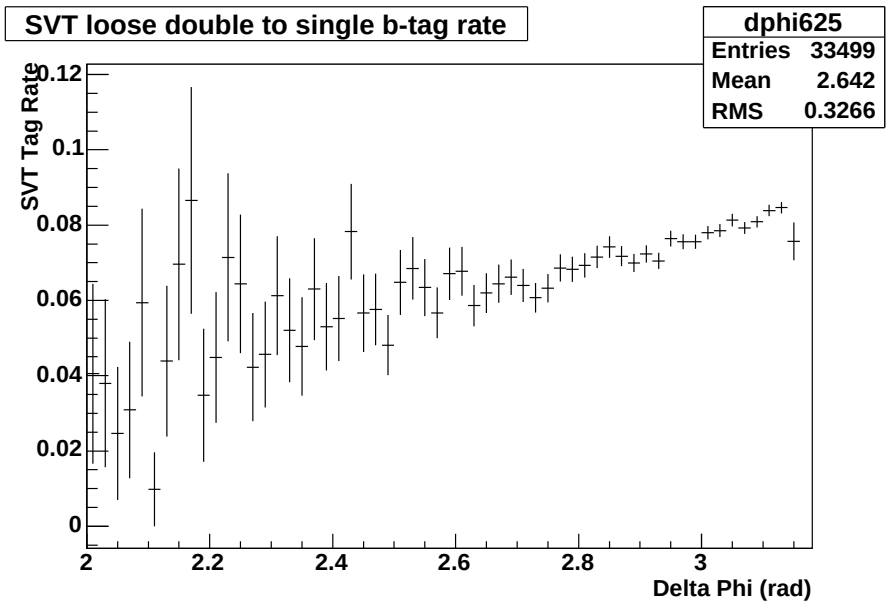

Figure 5.9: The variation of tag ratio with $\Delta\varphi$ between the two leading b-jets in each event, for pre-v13 data, using jets from all η regions. A linear dependence of the tag ratio upon $\Delta\varphi$ is observed.

As $\Delta\varphi$ increases, the ratio of double to single tags increases linearly, and we can evaluate and apply a correction for this effect. It would seem sensible to fit the plot linearly (using out-of-zone events) and then to extrapolate from the mean value of $\Delta\varphi$ out-of-zone to the average $\Delta\varphi$ value in-zone and derive a correction factor.

The main challenge posed by such a strategy is the difficulty of obtaining a sufficiently precise fit to the TRF. The systematic uncertainty on the number of

background events is dominated by the error on the linear fit, and this was found to be relatively large (of the order of 4%). A more accurate approach would be as follows: construct the TRF-weighted invariant mass as described above, and then fix the overall normalisation of this weighted distribution to match that of the observed double tagged mass spectrum. We fix the normalisation by fitting to the observed doubly-tagged mass distribution above 120 GeV/c^2, since this region is almost completely signal-depleted. Performing normalisation outside the signal region allows us to see an excess of events inside the signal region more precisely, and leads to a more accurate background estimation.

5.6.3 III: From $\Delta\varphi$ Zones to Mass Zones

While the above method helps us to account for the TRF's dependency on $\Delta\varphi$, it still relies upon the definition of two different $\Delta\varphi$ zones to distinguish signal from background. This could complicate matters and could still introduce a residual $\Delta\varphi$-dependent bias. It would be preferable to do away with the two $\Delta\varphi$ zones and instead define the signal-rich and signal-depleted regions purely in terms of invariant mass instead, given that we measure the final peak in the invariant mass plane.

Up till now we have been calculating the TRF using out-of-zone events, and applying it to in-zone events. It would be better to evaluate the TRF using the same in-zone events to which it will be applied, and then again to fix the overall normalisation by fitting the invariant mass distribution to the data above 120 GeV/c^2. This will remove any $\Delta\varphi$-dependent difference between the events used for the TRF and the candidate signal (in-zone) events. It will also result in larger statistics for the background determination. In what follows, this is the approach used to model the background.

As with the previous methods, the main obstacle is to derive a sufficiently accurate normalisation fit of the invariant mass to the double tagged data. The systematic uncertainty of the background which, as we have seen from equation 5.1, is critical to extract a signal of any significance, is dominated by the error on this fit.

5.6.4 IV: Moving From a Mass-based to a Jet-based TRF

The derivation of the TRF can be further improved by moving away from a mass-based TRF. Instead of forming the TRF using invariant mass, the TRF can be constructed on a jet-by-jet basis. A similar approach was adopted in the DØ Run II $hb\bar{b}$ analysis [59], and it offers two advantages. First, it eliminates any bias that might arise as a result of any possible dependence of the dijet mass upon $\Delta\varphi$. Second, it avoids having to determine the TRF from the very quantity - invariant mass - to which it is being applied.

In practice, we consider events in which the first-leading jet is b-tagged (with a loose offline SVT tag). For all such events, the second leading jet is categorised according to its location in one of three different η regions of the detector: $|\eta| < 1.1$, $1.1 < |\eta| < 1.5$ and $1.5 < |\eta| < 2.5$. Within each of these η ranges, the TRF is then parametrised as a function of the p_T of the second leading jet. This generates a TRF *per jet*, as shown in Figure 5.10, and is likely to be a more accurate method as it provides a finer resolution to the weighting. Remember that we are now only using signal-enriched in-zone events to form the TRF so as to minimise any $\Delta\varphi$ bias. For comparison, the analysis is repeated using a TRF derived from background out-of-zone events; the results can be found in Appendix B.

This jet-based TRF technique is the method used to measure the double tagged background. In summary, it involves the following steps:

1. Select single b-tagged in-zone events (i.e. signal-like events that pass the cut $\Delta\varphi > 2.75$);

2. Using these single tagged in-zone events, construct a jet-based TRF as a function of the p_T and η of the second leading jet;

3. Weight the singly-tagged in-zone events with this TRF to yield an estimate of the double tagged background;

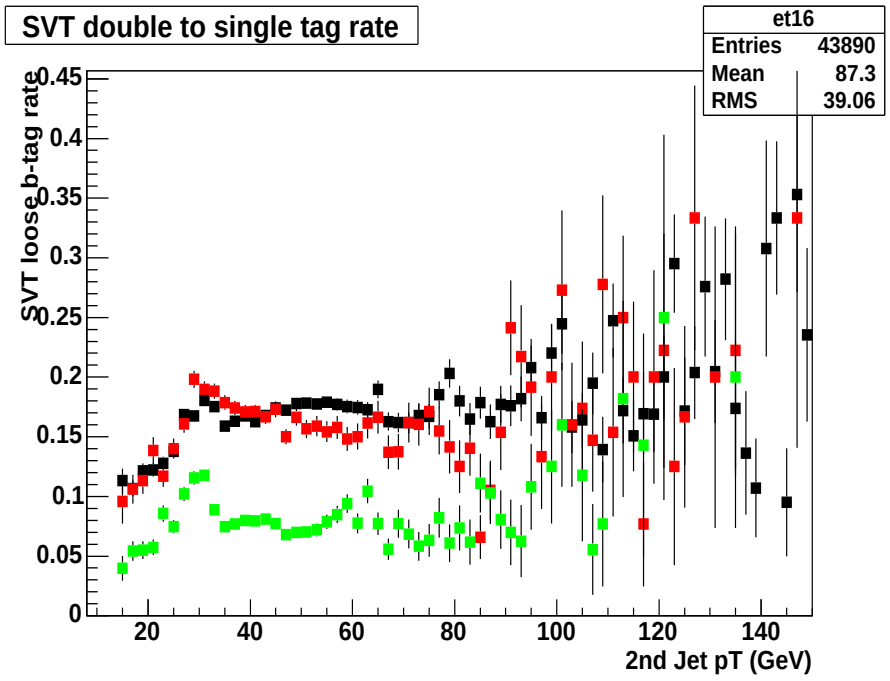

Figure 5.10: Tag ratio as a function of second leading jet p_T for jets in the regions $|\eta| < 1.1$ (black), $1.1 < |\eta| < 1.5$ (red (medium grey)) and $1.5 < |\eta| < 2.5$ (green (light grey)), evaluated for in-zone events in pre-v13 data.

4. Form the estimated background invariant mass using double tagged events;

5. Fit the normalisation of this background template to the observed double tagged mass distribution, using a fit to the signal-depleted invariant mass region above 120 GeV/c^2;

6. Subtract this normalisation-fitted background from the data and look for an excess of events.

5.6.5 Comparing The Background Model to Data

We now apply this background model to the entire pre-v13 dataset. Figure 5.11 shows the double tagged mass distribution, superimposed onto which are the predicted double tagged background and the expected signal from MC. Also shown is the fit of the background to the high-mass sideband (above 120 GeV/c^2). The normalisation correction is represented by a single fit parameter "bkg"[5].

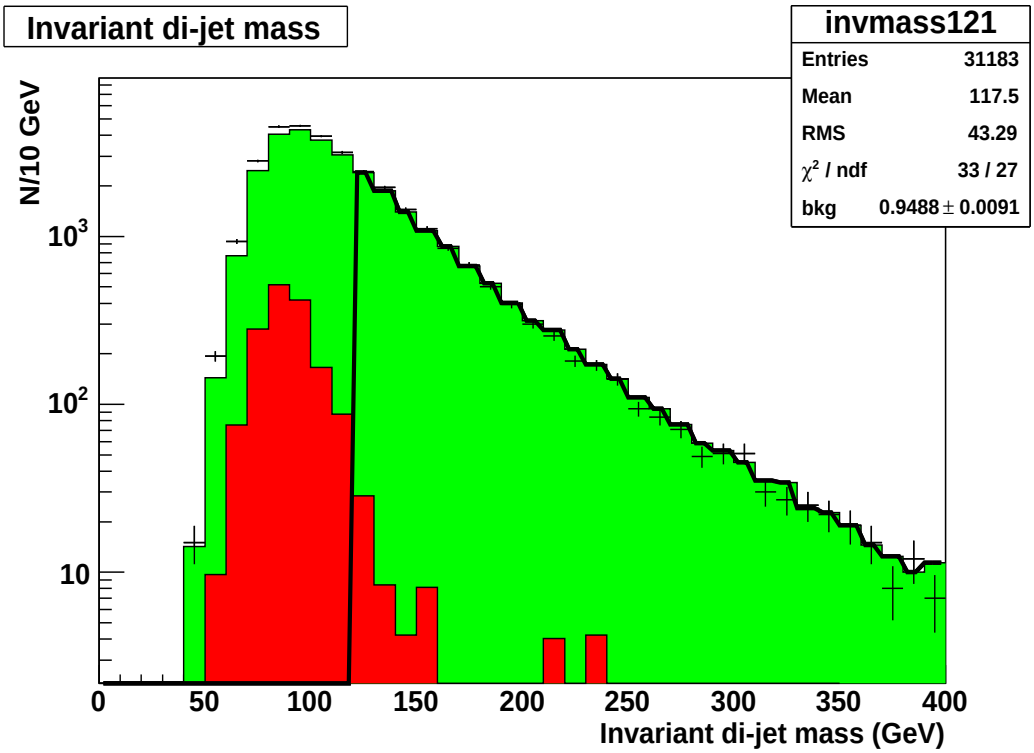

Figure 5.11: Invariant dijet mass in the pre-v13 data *before* background subtraction. Green (light grey) shaded histogram: expected background, estimated using a jet-based TRF from in-zone events and fitted with a one parameter fit to the observed data above 120 GeV/c^2. Black points: total dijet mass distribution observed in data. Red (dark grey) shaded histogram: expected $Z \to b\overline{b}$ signal from MC. The fit (bold black line) results in a correction to the background scale of 0.9488 ± 0.0091.

The mass spectrum of the normalised background template is compared to data

[5]By construction this method produces an invariant mass template for the background that has an identical number of integrated events as the observed double tag distribution. If the invariant mass shape of the background and observed data were identical, the normalisation would be equal to 1. In fact, the fit yields a scale factor of 0.95. This indicates a difference in the relative fraction of events above and below 120 GeV/c^2 between the background template and the double tagged data. There are more events in the Z mass region within the double tagged data.

and $Z \rightarrow b\bar{b}$ MC in Figure 5.12. The dark blue (black) band represents an overall systematic error on the background of ±1.8%, discussed in Section 5.6.6. Figure 5.13 presents the invariant mass after subtraction of the background; a Gaussian distribution is found to describe both the data and MC peaks nicely. A complete breakdown, mass-bin by mass-bin, of the excess in pre-v13 data and Monte Carlo is given in Table 5.10. From these numbers we can see that the peak of the excess clearly lies in the 60–120 GeV/c^2 range as expected from Monte Carlo predictions. In fact, the excess peak has a mean mass of 84.7 GeV/c^2 and a width of 13.1 GeV/c^2 (Figure 5.13).

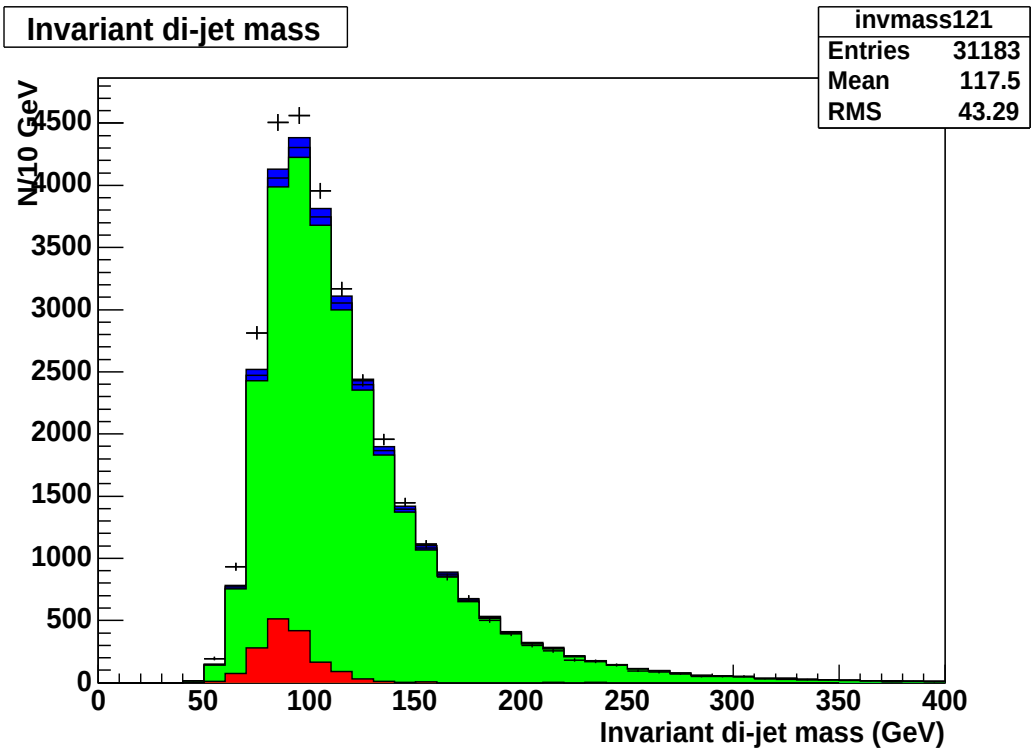

Figure 5.12: Invariant dijet mass in the pre-v13 data *before* background subtraction. Green (light grey) shaded histogram: expected background, estimated using a jet-based TRF from in-zone ($\Delta\varphi > 2.75$) events. The dark blue (black) band represents an overall systematic error on the background of ±1.8%, discussed in Section 5.6.6. Black points: total dijet mass distribution observed in data. Red (dark grey) shaded histogram: expected $Z \rightarrow b\bar{b}$ signal from MC.

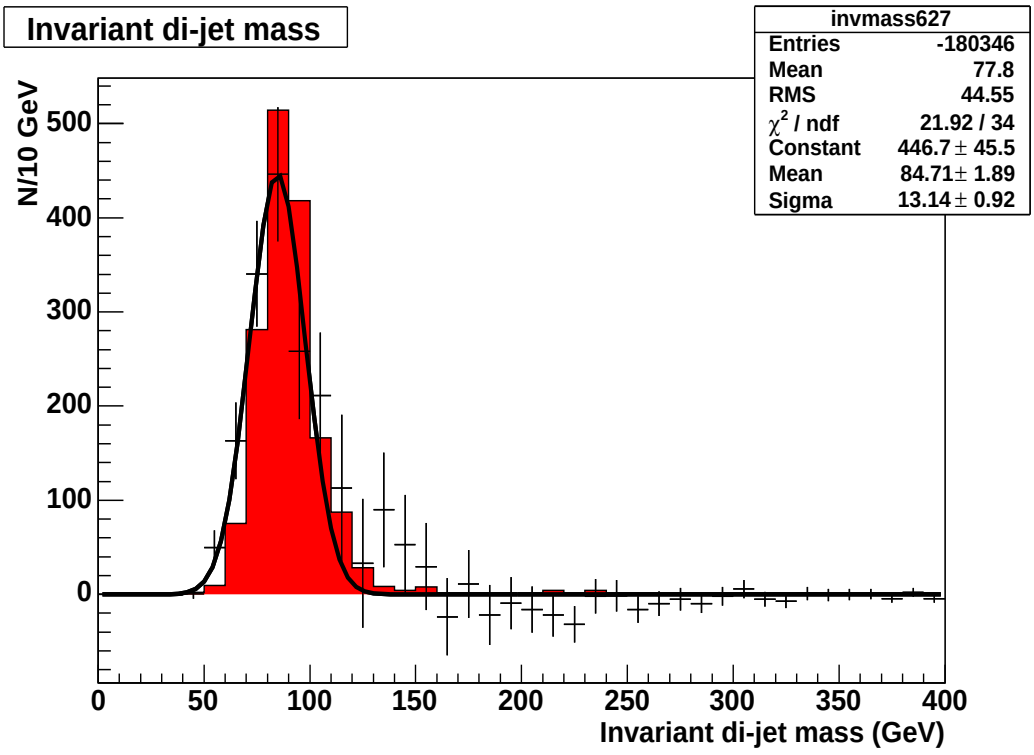

Figure 5.13: Invariant dijet mass spectrum in the pre-v13 data *after* background subtraction (using the in-zone, $\Delta\varphi > 2.75$, jet-based TRF). Black points: excess observed in data, fitted with a Gaussian. Error bars show statistical errors only. Red (dark grey) histogram: expected $Z \to b\bar{b}$ signal from MC. The excess peak has a mean mass of 84.7 GeV/c^2 and a width of 13.1 GeV/c^2.

Invariant Mass Bin (GeV/c²)	Events Observed	Events Predicted	Excess Observed	Excess Predicted
0–30	0	0	0	0
30–60	209	158.9 ± 4.8	50 ± 15	11.6 ± 7.7
60–90	8251	7301 ± 32	950 ± 96	871 ± 67
90–120	11686	11104 ± 40	580 ± 120	672 ± 59
120–150	5834	5658 ± 28	176 ± 81	41 ± 15
150–180	2639	2622 ± 19	17 ± 55	8.1 ± 6.5
180–210	1196	1243 ± 13	-47 ± 37	0
210–240	607	662.5 ± 9.7	-56 ± 26	8.3 ± 6.5
240–270	319	346.4 ± 7.0	-27 ± 19	0
270–300	171	187.9 ± 5.2	-17 ± 14	0
300–330	108	114.6 ± 4.0	-6.6 ± 11	0
330–360	66	65.7 ± 3.1	0.3 ± 8.7	0
360–390	35	37.0 ± 2.3	-2.0 ± 6.3	0

Table 5.10: Signal candidate counts before and after background subtraction in the pre-v13 data and MC. The errors are statistical.

Search Window (GeV/c^2)	Events Observed	Events Expected	Overall Excess	Total Stat. Error	Total Syst. Error	Overall Error
70–110	15840	14580	1260	130	260	290
Prediction from MC:			1380 $\pm$ 84 (stat.)			
Significance of Result:			4.3 σ			

Table 5.11: Excess of events observed in the 70–110 GeV/c^2 search window after background subtraction has been performed in the pre-v13 data, along with the signal prediction from MC. Agreement is seen between the excess observed and the number of signal events predicted.

After background subtraction we observe an excess of

1260 $\pm$ 130 (stat.) $\pm$ 260 (syst.) events

(297.5 pb^{-1} of pass2 data passing MU_JT25_L2M0)

in the 70–110 GeV/c^2 mass window, as plotted in Figure 5.13. The excess peak is fitted with a Gaussian and compared to the number of events expected from Monte Carlo. Using the Standard Model $\sigma \times$ B.R($Z \rightarrow b\overline{b}$) of 1.131 nb, we expect to see

1380 $\pm$ 84 (stat.) events

($Z \rightarrow b\overline{b}$ MC events passing MU_JT25_L2M0)

and therefore observe agreement between data and Monte Carlo within the errors. Table 5.11 summarises the overall excess of events in the pre-v13 dataset. Taking the significance of the result to be the signal size divided by the total error (assuming that this error is a purely Gaussian one), the observed signal corresponds to a significance of 4.3 standard deviations.

5.6.6 The Mass Peak And Its Uncertainty

The total statistical error on the observed excess is calculated by combining in quadrature the statistical errors on the number of observed double b-tagged events and the number of expected double b-tagged background events. Remember that the statistical error on the expected double-tagged background is not the same as the statistical error on the observed number of double-tagged events. The former is related to the TRF derived using *single-tagged* events that is then used to form the double-tagged background invariant mass distribution. The latter is related purely to the number of *double-tagged* events passing the analysis cuts.

The systematic uncertainty on the observed excess consists of two components:

1. A contribution related to the uncertainty on the normalisation of the background at high masses. This uncertainty is taken from the error on the normalisation fit parameter (given in Figure 5.11), and was found to be 1.0% of the number of background events.

2. A contribution arising from the uncertainty on the shape of the invariant mass background template. It is conceivable, for example, that the b-content of the sample might shift the invariant mass peak in some way, thus causing the shape of the double tagged background to be incorrectly modelled. We conclude that this factor is small, given that the χ^2/degree of freedom of the normalisation fit is small at masses above 120 GeV/c^2, nevertheless it is important to gauge its size.

   To this end, we compared the shape of the invariant mass spectrum derived from an untagged or '0 tag' sample (light-quark dominated) to that derived from a single tagged or '1 tag' sample (b-contaminated). Essentially, the background subtraction technique was applied exactly as usual, except that it was

applied to untagged and single tagged events (termed the '0 → 1 tag' approach) as opposed to our typical '1 → 2 tag' method. In this way we are able to measure any effect arising solely from the b-content of the sample.

The study revealed a net uncertainty on the number of background events of less than 1.5% in the 70–110 GeV/c^2 Z mass window. It is valid to extrapolate this systematic error from the 0 → 1 tag to the 1 → 2 tag scenario, since the b-content is increased by the same factor in each case.

Overall, the total systematic error on the background is found to be 1.8% (by combining 1.0% and 1.5% in quadrature). By combining the statistical and systematic uncertainties, we arrive at the total error on the background, as given in the final column of Table 5.11. Taking into account this systematic, the observed excess has a significance of 4.3 standard deviations.

The invariant mass peak of the excess lies at a mean mass of 85 ± 2 GeV/c^2 in both Monte Carlo and data after jet energy scale corrections have been applied. The width of the peak is approximately 13 ± 1 GeV/c^2 in both Monte Carlo and data. At the time of this analysis no official b-jet JES correction was available for this data (save for a correction for the semileptonic decay of the b-jet), which could account for the Z mass peak being shifted to lower masses. Moreover, energy loss during hard final state radiation could result in a mass shift, as suggested from the studies presented in Chapter 3 [60].

5.6.7 Closure Test

As a closure test, the sum of the invariant mass templates of the signal MC and estimated background were fitted to the entire mass range of the observed double tagged candidates. The scales of the two templates were fitted with two unconstrained scale parameters, "bkg" and "signal" (see Figure 5.14).

The fitted background scale parameter is 0.95 ± 0.01, which is compatible with the value obtained from Figure 5.11 within the errors. Meanwhile the fitted signal

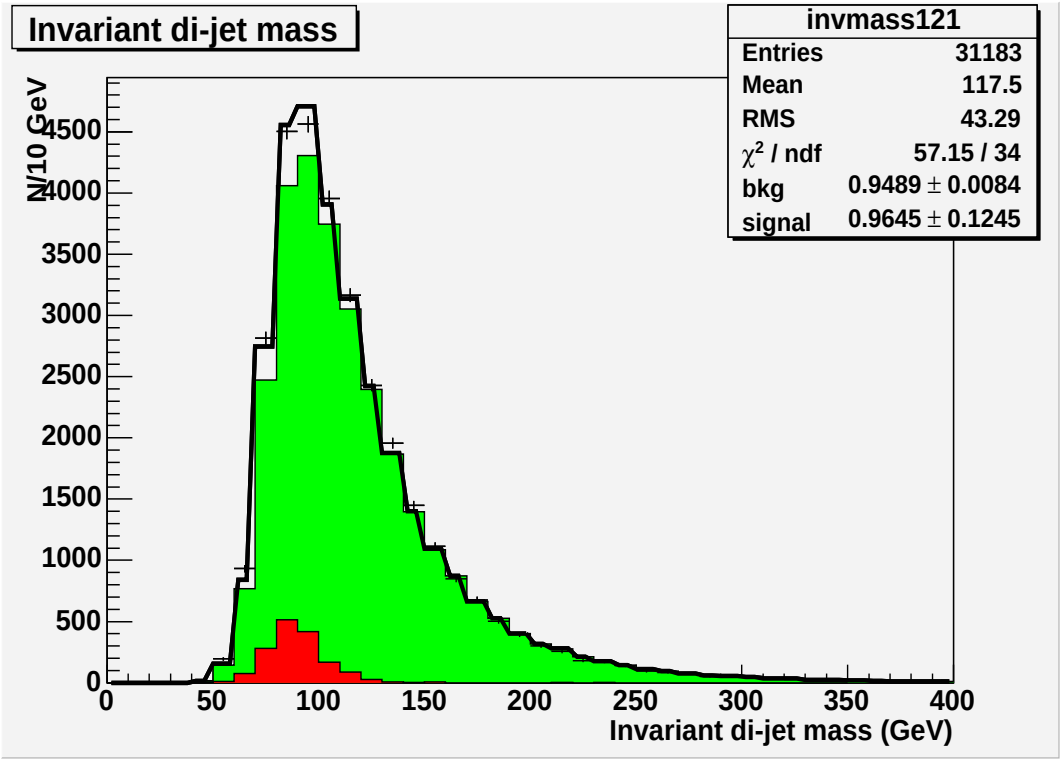

Figure 5.14: Closure test of the final invariant dijet mass spectrum observed in the pre-v13 data after background subtraction. Green (light grey) shaded histogram: expected background, estimated using a jet-based TRF from in-zone events. Black points: total dijet mass distribution observed in data. Red (dark grey) shaded histogram: expected signal from MC. The bold black line shows the fitted sum of the scaled background and MC templates.

scale parameter (0.96 ± 0.12) is in agreement with the expected value 1, within errors. It can therefore be concluded that the sum of the signal MC and the background - calculated using the in-zone TRF-based model and normalised to the high mass region - is compatible with the observed double tagged invariant mass over the full mass spectrum. In addition, we find that it is necessary to add the signal MC to the background template in order to obtain a better fit to the data.

5.7 Cross-checking The Background Model

An alternative method of background estimation ('Method 2') [61] has been developed in order to cross-check the results obtained above ('Method 1'). This second approach differs from the original method in the following ways:

- Pass1 rather than pass2 data are analysed. The pass1 data make use of a different algorithm for clustering calorimeter information, and employ an older version of the jet energy scale corrections (version 5.1 as opposed to version 5.3).

- No trigger selection is applied during event selection.

- A tighter primary vertex requirement is imposed - more than four tracks must be attached to the vertex and $|z|$ must be < 35 cm (i.e. within the fiducial b-tagging region).

- A tighter $\Delta\varphi$ cut is used: > 2.9 instead of > 2.75.

- A correction is explicitly applied to the estimated background in order to compensate for the '$0 \rightarrow 1$ tag' (b-content) effect described in Section 5.6.6. The final invariant mass peak is then shifted by this correction, which is found to be small. In contrast, method 1 deals with this effect by simply assigning a systematic error to the estimated bacgkround.

- An extra correction is applied in order to incorporate back into the mass peak 'lost' signal events that are not double b-tagged. First a signal peak (excess) is measured in double tagged data. Second, the number of signal events that would crop up in the untagged and single tagged backgrounds is determined from $Z \rightarrow b\overline{b}$ MC, by requiring zero, one and two b-tags. The signal peak measured in data is then scaled by these factors and the expected background in the double tagged dataset is computed. Overall, this effect is found to be

small [58]. Method 1, which does not account for these signal events, will provide a slightly more conservative measure of the excess.

5.7.1 Results Obtained With This Method

For full details of the results obtained with this method, see [61]. The final $Z \rightarrow b\bar{b}$ peak derived from data, after all corrections, is shown in Figure 5.15 as the green (light grey) "Corrected Diff" peak. This invariant mass distribution is compared to the shape of the $Z \rightarrow b\bar{b}$ peak in MC (blue (grey) curve). A Gaussian distribution is found to fit both the data and MC peaks well.

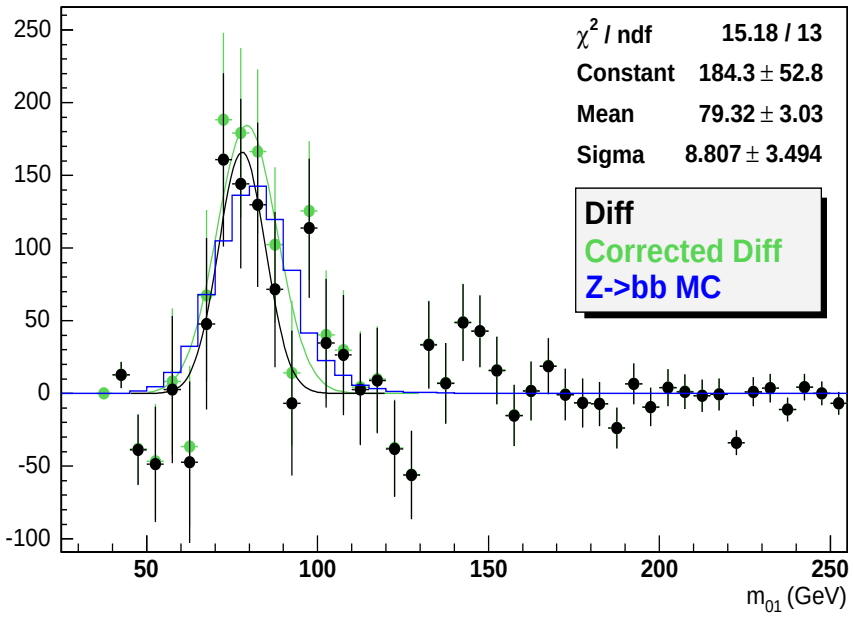

Figure 5.15: The final $Z \rightarrow b\bar{b}$ peak derived from data, after explicit $0 \rightarrow 1$ and signal corrections. Green (light grey) points: final distribution after all corrections. Blue (grey) line: the $Z \rightarrow b\bar{b}$ MC peak. Black points: excess in data without the signal correction.

Both the mean (79 ± 3 GeV/c^2) and width (9 ± 3 GeV/c^2) of the peak are comparable to those derived from signal MC (81 GeV/c^2 and 11 GeV/c^2, respectively). 810 ± 230 $Z \rightarrow b\bar{b}$ events are observed after background subtraction. Without correcting for signal events that are 'lost' within untagged or single tagged background-rich regions, 570 ± 160 events are observed. The total number of events expected

from $Z \rightarrow b\overline{b}$ MC cannot be estimated very accurately using this method, because events were not selected with a given trigger. However, for an assumed luminosity of 300 pb^{-1}, the size of the $Z \rightarrow b\overline{b}$ peak observed in data would correspond to an overall trigger/skimming efficiency of about 15% (which agrees with the efficiencies presented in Section 5.3).

5.8 Summary of Results

Various methods of background estimation were developed to be as accurate and robust as possible, in an attempt to extract an observable $Z \rightarrow b\bar{b}$ signal in the p14 dataset using the BID skim. By making use of events in the back-to-back $\Delta\varphi$ region to model the background, and specifically applying a jet-based TRF to these events, we observe the following excess in 297.5 pb^{-1} of data collected with the MU_JT25_L2M0 trigger:

1260 ± 130 (stat.) ± 260 (syst.) events

(297.5 pb^{-1} of pass2 data passing MU_JT25_L2M0)

This is compared to the following expectation from Monte Carlo:

1380 ± 84 (stat.) events

($Z \rightarrow b\bar{b}$ MC events passing MU_JT25_L2M0)

The observed signal amounts to a significance of 4.3 standard deviations.

A second approach, which uses a slightly different dataset and does not select events by trigger, confirms the observed excess:

810 ± 230 (stat.) events

(∼300 pb^{-1} of pass1 data)

The position and width of the observed mass peak agree with predictions from Monte Carlo in both cases. Method 1 finds a mass peak with a fitted mean of 85 ± 2 GeV/c^2 while method 2 observes a fitted mean mass of 79 ± 3 GeV/c^2. The difference between the observed mass peaks can be attributed to two factors. First, the event selection criteria are different; method 1 selects events using a single trigger condition with a high p_T cut, while method 2 does not use any trigger at all.

Second, the two approaches use two different datasets (pass1 versus pass2), and the response of the calorimeter is modelled differently in each case. MC studies have shown that the reconstructed peak position is sensitive to both trigger conditions and muon and jet p_T requirements.

5.9 Conclusions

It has been demonstrated, with the first 300 pb^{-1} of Run II data collected by DØ, that a $Z \to b\bar{b}$ dijet mass resonance can be successfully isolated from the large QCD background. The observed excess agrees well with expectations from signal Monte Carlo events.

Thanks to the new suite of dedicated $Z \to b\bar{b}$ triggers discussed in Chapter 4, DØ has already collected a data sample that is several times larger; this is now waiting to be analysed. The increased statistics from this sample are expected to provide not only a larger Z peak, but also to enable a more precise determination of the background.

Chapter 6

Conclusion

"The only absolute truth is that there are no absolute truths."

Paul Feyerabend

6.1 Summary

In the Standard Model, the Higgs boson is the last piece of the puzzle that remains to be discovered. The Higgs mechanism is thought to be the fundamental ingredient by which particles acquire mass and one of the main goals at the Tevatron is to search for signs of it. Until the LHC turns on in 2008/9, the Tevatron will remain at the forefront of discovery in the quest for the Higgs.

There is strong evidence that the Higgs particle in the Standard Model is light. Using direct and indirect experimental evidence we can place limits on its possible mass: it must be heavier than 114 GeV/c^2 and lighter than 260 GeV/c^2 [14]. At the Tevatron, DØ will need about 2 fb^{-1} of data to explore beyond the 114 GeV/c^2 lower bound and this integrated luminosity will be in hand soon.

Both the Tevatron and DØ are performing well. The Tevatron now regularly exceeds the design instantaneous luminosity and DØ is recording data with an efficiency of over 90%. DØ's Higgs physics programme is a rich and varied one, encompassing searches not only for the Standard Model Higgs but also for Higgs

signatures hypothesised by more exotic models. The Higgs group has already published six papers with more expected in the near future. These include searches for the Standard Model Higgs in $ZH \rightarrow \nu\nu b\overline{b}$ and $WH \rightarrow l\nu b\overline{b}$ (where l is an electron or muon), combined limits on the Standard Model Higgs production at the Tevatron and a search for supersymmetric Higgs boson partners.

If the Higgs has a mass less than 135 GeV/c^2, it decays predominantly to a b and $\overline{b}$ quark-antiquark pair. Reconstructing the parent Higgs relies upon having a good understanding of the b-quark jet energies and overcoming the $b\overline{b}$ background that will overwhelm any potential Higgs mass peak. Fortunately, there is a perfect testbed for the (light) Higgs process: the decay of a Z boson to $b\overline{b}$. It represents a proof of principle; the ability to reconstruct this Z decay at a hadron-hadron collider can offer valuable insights into our potential for detecting the Higgs via the $b\overline{b}$ channel. Finding $Z \rightarrow b\overline{b}$ is therefore a crucial part of DØ's physics programme. Moreover, this decay allows us to tune the jet energy scale, which affects much of the physics studied at DØ, in addition to refining our b-tagging methods and associated analysis techniques. A $Z \rightarrow b\overline{b}$ peak can be used to understand the jet processes that occur and the di-b-jet mass resolution attainable. $Z \rightarrow b\overline{b}$ will provide important insights into the approaches that are needed to isolate the signature of a light Higgs at the Tevatron and beyond.

In this thesis I have worked towards that end, contributing very significantly to the physics output of the DØ experiment. My studies of jet energy resolution and dijet mass resolution have furthered our understanding of the factors that will affect our ability to distinguish a Higgs mass peak above a large QCD background.

Triggering at a hadron-hadron collider is of paramount importance and is a challenging and complex task. If the Higgs (or indeed new physics signatures) are to be discovered, effective triggers must be put in place to select candidate events prior to any offline data analysis. With regard to $Z \rightarrow b\overline{b}$, the ability to trigger on the decay of the Z boson using the properties of its daughter b-jets is essential. My

development of triggers tailored specifically towards the $Z \rightarrow b\overline{b}$ process has made a valuable contribution to our knowledge of triggering at a hadron-hadron collider. This was the first time that triggers were designed using the impact parameter b-tagger at Level 3. The resulting suite of muon triggers are now an integral part of DØ's trigger strategy; they underpin the full Run IIa publications and form a trigger basis for future Run IIb publications. By exploiting the power of b-tagging at Level 3, these triggers have been shown to outperform pre-existing muon triggers and achieve the background rejection that is needed at the high instantaneous luminosities delivered by the Tevatron. With more data they will play an essential role in future measurements of the $Z \rightarrow b\overline{b}$ resonance.

The first observation of $Z \rightarrow b\overline{b}$ decays at DØ constitutes a significant advance forward for the Higgs physics group at DØ. Using 300 pb^{-1} of Run II data and exploiting the semileptonic decay of the b-jets to muons, the signal yield is 1260 ± 130 (stat.) $\pm$ 260 (syst.) events. The mass peak lies at a mean of 85 GeV/c^2 with a width of 13 GeV/c^2. This excess, obtained with non-optimised muon triggers, gives us hope that by exploiting the larger dataset and the $Z \rightarrow b\overline{b}$-specific triggers, DØ will be able to measure a large $Z \rightarrow b\overline{b}$ signal and use it for detailed calibration of the b-jet energy scale.

6.2 The Bigger Picture

The studies of jet energy and dijet mass resolution presented in this thesis were the first at DØ to employ a full Run IIa simulation, therefore serving as the basis for further studies. DØ has now gone on to fully calibrate the calorimeter (both the hadronic and the electromagnetic components) and to develop more sophisticated energy clustering methods such as the track-jet algorithm, which aims to improve the jet energy resolution by combining track and jet information together [46].

Due to increases in instantaneous luminosity there will always be further development and refinement of the $Z \rightarrow b\overline{b}$ triggers, and they were designed with extendability in mind. Extensions to the work described here include making use of three-dimensional b-tagging at Level 3 and using the Level 2 Silicon Track Trigger to select dijet events with displaced vertices at an earlier stage in the trigger level. By not having to rely on the muonic decays of the b-jets, this approach has the potential to greatly improve the signal significance. In a wider context, the $Z \rightarrow b\overline{b}$ triggers have proven to be valuable in other Higgs, B-physics and top physics analyses and, as the luminosity increases, they will become increasingly important to other decay channels.

Now that the $Z \rightarrow b\overline{b}$ decay has been reconstructed at DØ the Higgs physics group will continue the work started here. While we do not expect to find $H \rightarrow b\overline{b}$ except in association with a Z or W boson, $Z \rightarrow b\overline{b}$ is a very good test for any $H \rightarrow b\overline{b}$ search. This search has also improved our understanding of b-jet energy resolution and mass resolution. The limiting factor in the analysis is the systematic error on the estimated $b\overline{b}$ background. With increased statistics we can improve the accuracy of the tag-rate function used in the background determination and reduce the uncertainty on the normalisation of the fitted background template. By incorporating the 1 fb^{-1} of data now processed and exploiting the yield of the $Z \rightarrow b\overline{b}$ triggers, the analysis can be improved. Important new work will also lie in the use

of artificial neural networks to find optimal cut values for the decay, and future avenues could also involve the neural net b-tagger recently released at DØ [62].

With an increase in the size and significance of the excess, we can move towards testing the b-jet energy scale directly in data and ultimately calibrating it. This will reduce the uncertainty on the jet energy scale, with a significant impact on many analyses at DØ including the measurement of the top quark mass. A more accurate value of the top mass will enable us to constrain the mass of the Higgs more tightly. The DØ experiment has already shown that it is possible to extract a $Z \rightarrow b\overline{b}$ signal using a relatively small dataset from Run II. We can look forward to a more refined measurement of $Z \rightarrow b\overline{b}$ and the physics capabilities that accompany it.

Appendix A

Di-b-jet Mass Resolution in $Z \to b\bar{b}$

Z mass distributions (in $Z \to b\bar{b}$) are shown at the parton, particle and uncorrected calorimeter levels in Figure A.1 below. The effects observed at each stage of Figure A.1 are similar to those seen in $ZH \to e^+e^-b\bar{b}$. Moving from the parton to particle-jet to calorimeter-jet levels, one sees a shift of the mass distributions to lower energy and a worsening of mass resolution. Hard gluon radiation degrades these resolutions further. Table A.1 summarises the fractional Z mass resolution at each level, calculated using the four different definitions described in Section 3.7.1.

Distribution	**Measure of Mass Resolution (%)**			
	CG	$\boldsymbol{\mu \pm 3\sigma}$	$\boldsymbol{\mu \pm 5\sigma}$	**Overall**
Parton	1.6	2.2	2.8	5.6
Parton incl. FSR	5.3	7.8	10.8	17.6
Pjet	7.8	10.6	13.9	16.2
Pjet incl. FSR	9.1	12.5	17.6	20.3
Cjet	15.6	16.8	17.3	17.5
Cjet incl. FSR	17.7	20.3	21.2	21.2

Table A.1: Fractional Z boson mass resolutions at parton, particle ('pjet') and uncorrected calorimeter ('cjet') levels, excluding and including hard FSR. Four different measures of resolution were calculated for each level. No jet energy scale corrections were applied here.

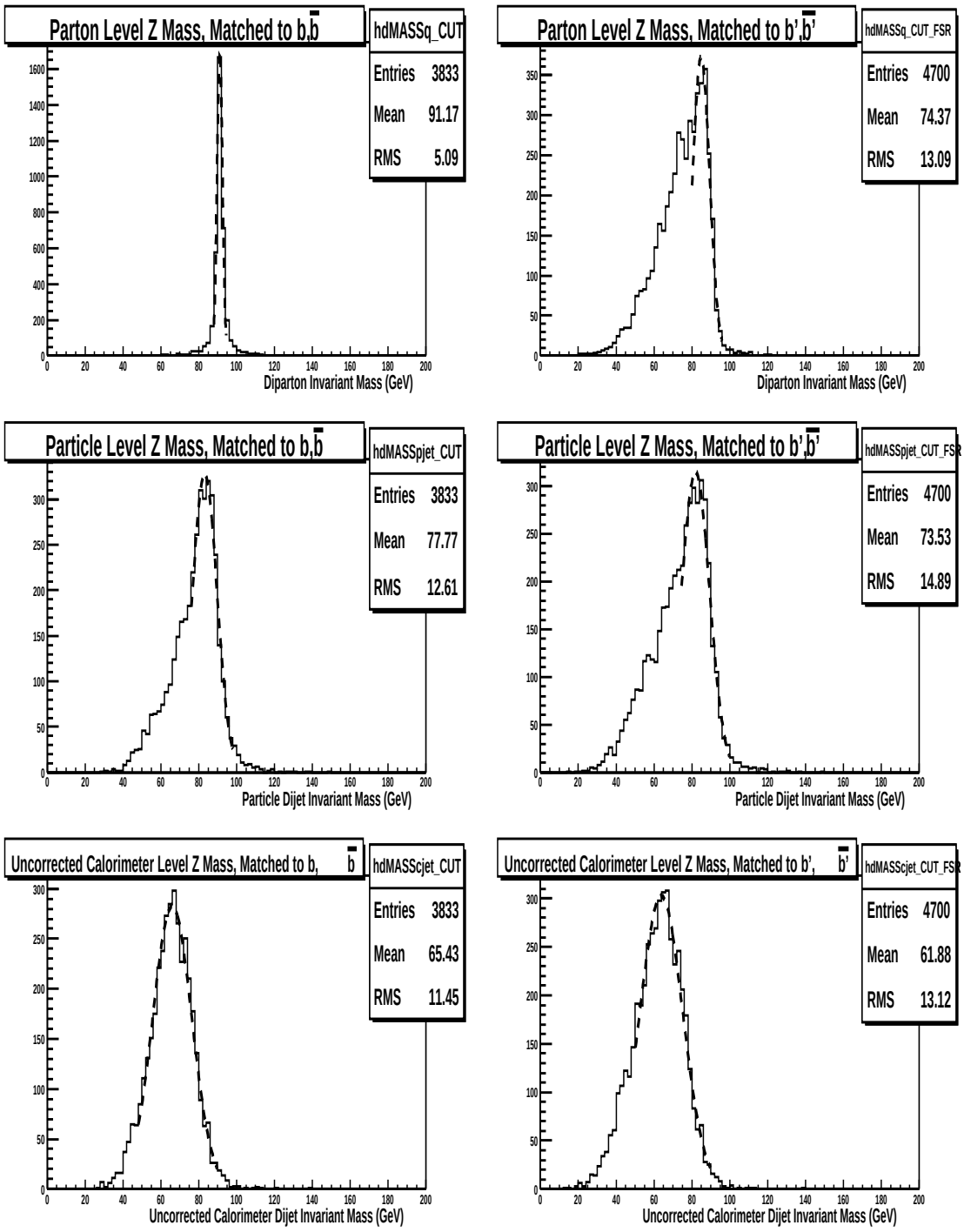

Figure A.1: Reconstructed Z mass at parton (top), particle-jet (middle) and uncorrected calorimeter-jet (bottom) levels. Without hard FSR (left); with hard FSR (right). All jets are 0.5 cone. Dashed profiles show central Gaussian fits to each distribution.

Appendix B

The Effect of Using Out-of-zone Events to Determine The TRF

In this appendix we repeat the analysis described in Section 5.6.4, but instead measure the double tagged background using out-of-zone events (as opposed to in-zone events). For historical reasons this study adopted a tighter $\Delta\varphi$ cut of 3.0 radians: in-zone events are defined as ones for which $\Delta\varphi > 3.0$ while out-of-zone events have $\Delta\varphi \leq 3.0$. In the plots that follow the jet energy scale correction for semileptonic b decay has not been applied, which will have the effect of shifting the invariant mass peaks to slightly lower masses. However, here we are more interested in the *relative* changes in the excess and background as a result of applying an out-of-zone TRF, rather than the absolute value of the mass peak obtained.

B.1 Using Out-of-zone Events

Figure B.1 plots the TRFs from out-of-zone events that are used to evaluate the background. Figures B.2 to B.4 show the invariant mass distributions before and after background subtraction.

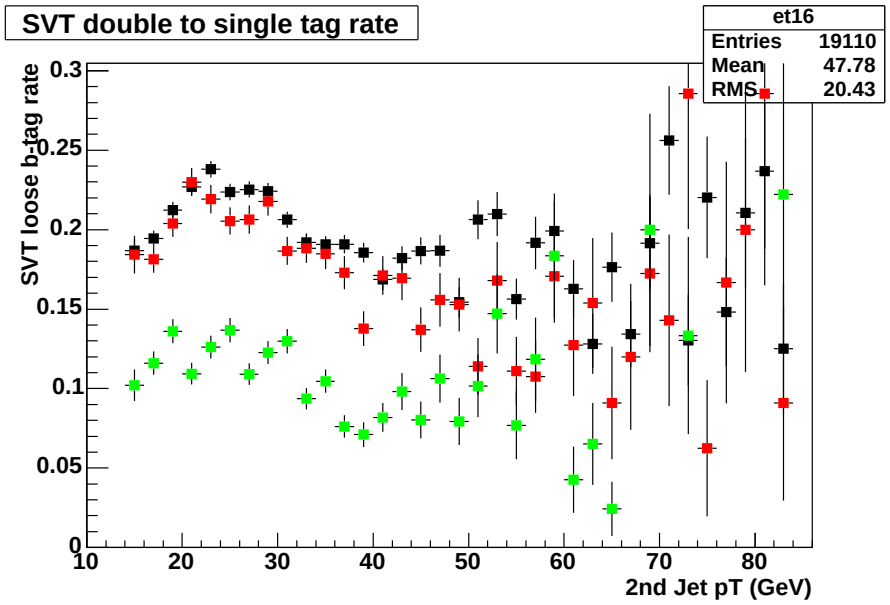

Figure B.1: Tag ratio as a function of second leading jet p_T for jets in the regions $|\eta| < 1.1$ (black), $1.1 < |\eta| < 1.5$ (red (medium grey)) and $1.5 < |\eta| < 2.5$ (green (light grey)), evaluated for out-of-zone ($\Delta\varphi \leq 3.0$) events in pre-v13 data.

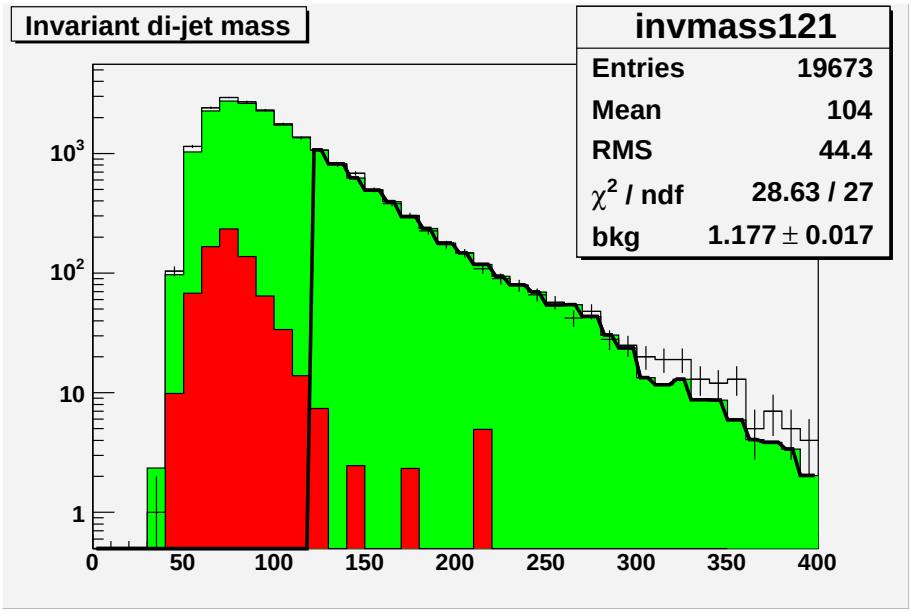

Figure B.2: Invariant dijet mass in the pre-v13 data *before* background subtraction. Green (light grey) shaded histogram: expected background, estimated using a jet-based TRF from out-of-zone events and fit to the observed data above 120 GeV/c^2. Black points: total dijet mass distribution observed in data. Red (dark grey) histogram: expected $Z \rightarrow b\overline{b}$ signal from MC. The fit (bold black line) results in a correction to the background scale of 1.177 ± 0.017.

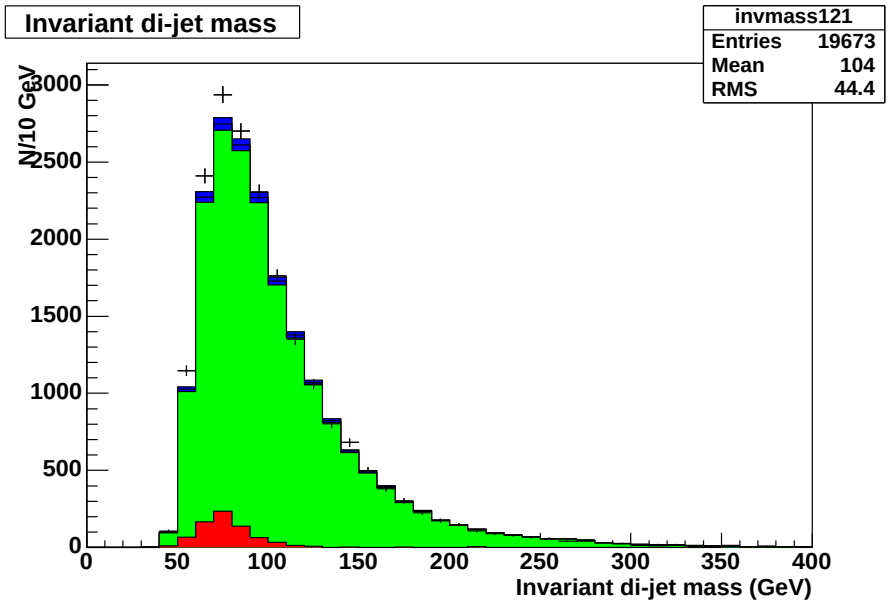

Figure B.3: Invariant dijet mass in the pre-v13 data *before* background subtraction. Green (light grey) shaded histogram: expected background, estimated using a jet-based TRF from out-of-zone events. The dark blue (black) band represents the ±1.5% systematic error on the background from the normalisation fit. Black points: total dijet mass distribution observed in data. Red (dark grey) histogram: expected $Z \to b\overline{b}$ signal from MC.

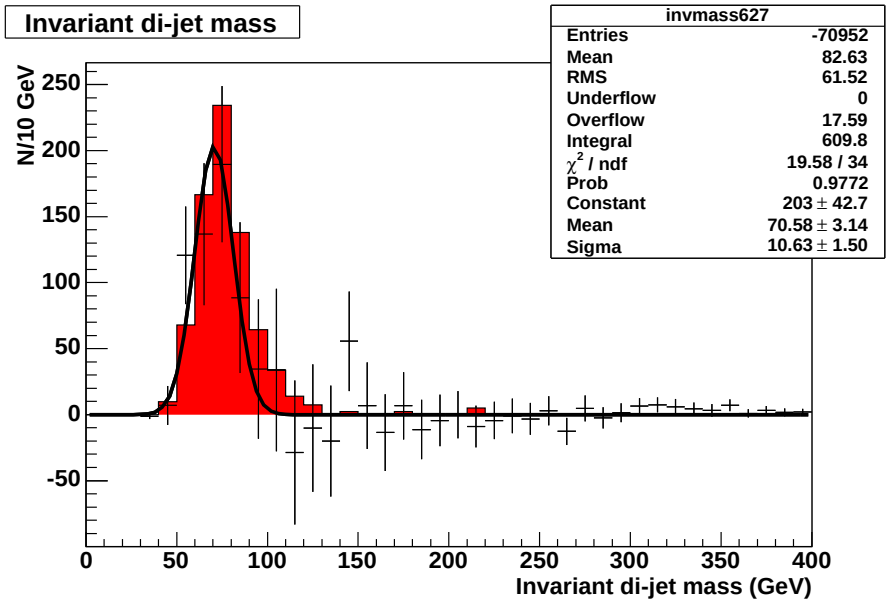

Figure B.4: Invariant dijet mass spectrum in the pre-v13 data *after* background subtraction (using the out-of-zone ($\Delta\varphi \leq 3.0$) TRF). Black points: excess observed in data, fitted with a Gaussian. Error bars show statistical errors only. Red (dark grey) histogram: expected $Z \to b\overline{b}$ signal from MC. The excess peak has a mean mass of 70.6 GeV/c^2 and a width of 10.6 GeV/c^2.

B.2 Using In-zone Events

Figure B.5 plots the TRFs from in-zone events that are used to evaluate the background. Figures B.6 to B.8 display the invariant mass distributions before and after background subtraction.

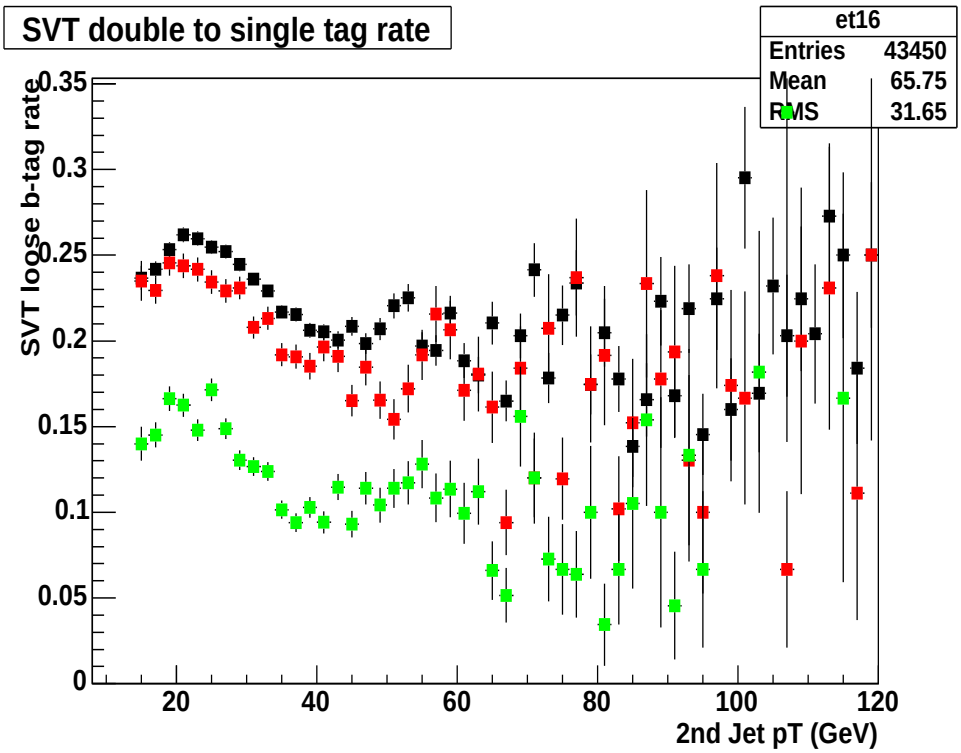

Figure B.5: Tag ratio as a function of second leading jet p_T for jets in the regions $|\eta| < 1.1$ (black), $1.1 < |\eta| < 1.5$ (red (medium grey)) and $1.5 < |\eta| < 2.5$ (green (light grey)), evaluated for in-zone ($\Delta\varphi > 3.0$) events in pre-v13 data.

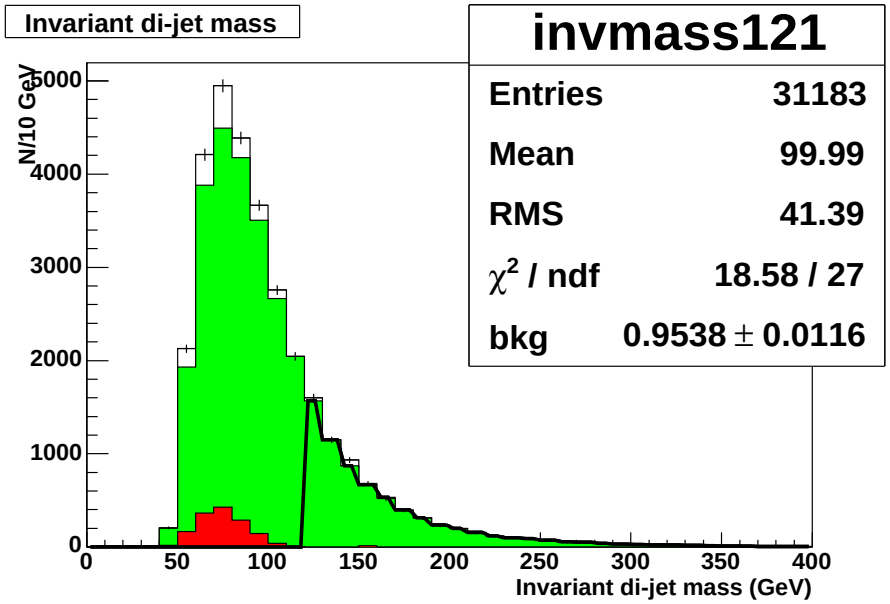

Figure B.6: Invariant dijet mass in the pre-v13 data *before* background subtraction. Green (light grey) shaded histogram: expected background, estimated using a jet-based TRF from in-zone events and fit to the observed data above 120 GeV/c^2. Black points: total dijet mass distribution observed in data. Red (dark grey) histogram: expected $Z \rightarrow b\bar{b}$ signal from MC. The fit (bold black line) results in a correction to the background scale of 0.9538 ± 0.0116.

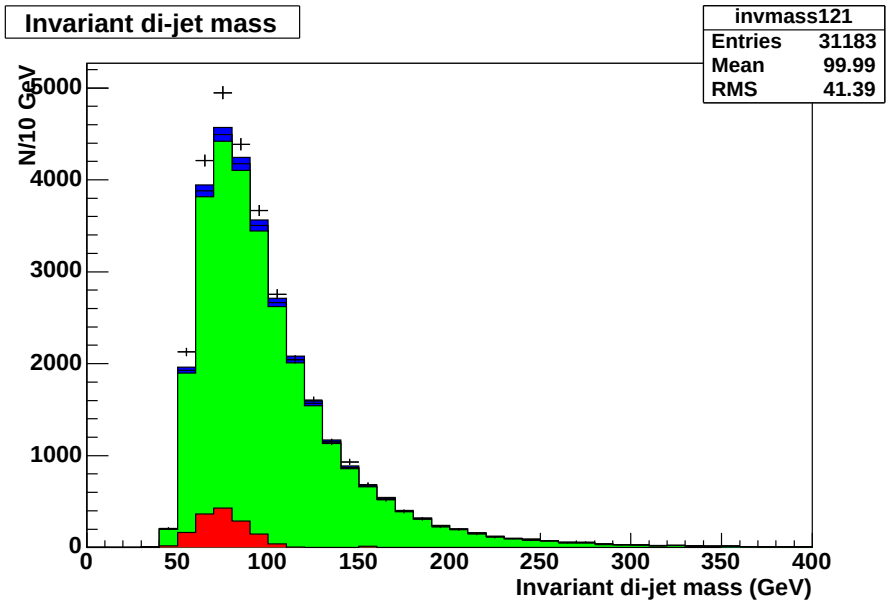

Figure B.7: Invariant dijet mass in the pre-v13 data *before* background subtraction. Green (light grey) shaded histogram: expected background, estimated using a jet-based TRF from in-zone events. The dark blue (black) band represents the ±1.2% systematic error on the background from the normalisation fit. Black points: total dijet mass distribution observed in data. Red (dark grey) histogram: expected $Z \rightarrow b\bar{b}$ signal from MC.

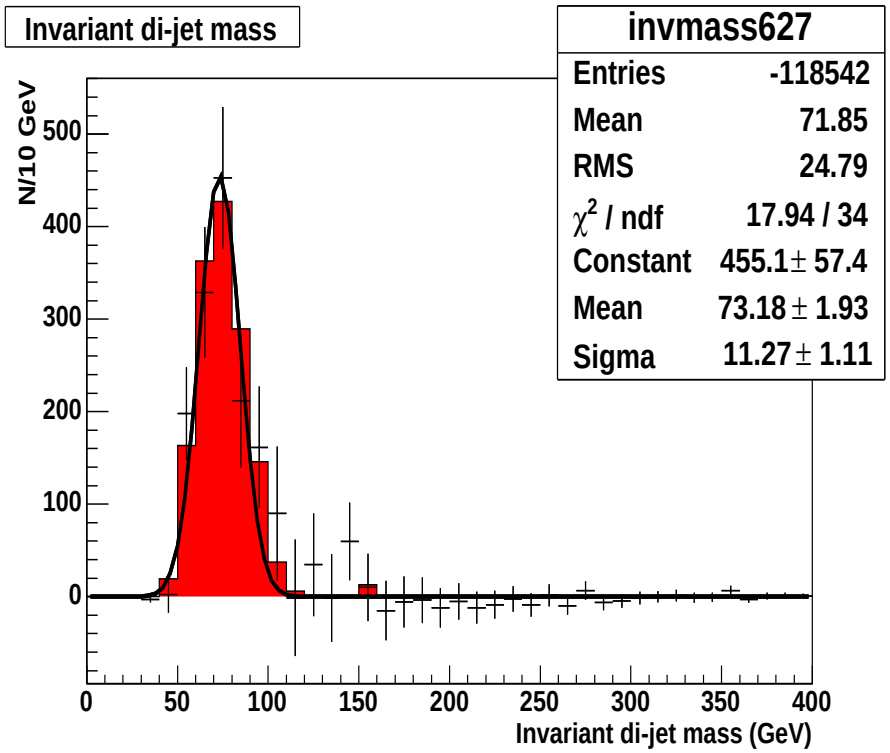

Figure B.8: Invariant dijet mass spectrum in the pre-v13 data *after* background subtraction (using the in-zone TRF). Black points: excess observed in data, fitted with a Gaussian. Error bars show statistical errors only. Red (dark grey) histogram: expected $Z \rightarrow b\overline{b}$ signal from MC. The excess peak has a mean mass of 73.2 GeV/c^2 and a width of 11.3 GeV/c^2.

B.3 Conclusion

By applying the in-zone TRF we obtain larger statistics for the TRF determination (thus a smaller systematic error), better data agreement at high masses and a smaller normalisation correction (as can be seen from Figure B.2). Thus we conclude that the in-zone TRF leads to a more accurate result and use this to extract the final results, discussed in Section 5.6.5 of Chapter 5.

Plots B.4 and B.8 show that the agreement between data and signal MC is better when the background is modelled using a TRF from in-zone events. The out-of-zone TRF results in a mass peak shifted to lower masses (approximately 3 GeV/c^2 lower), which suggests that a $\Delta\varphi$-dependent invariant mass bias does indeed exist for the out-of-zone events.

References

[1] E. M. Phillips & D. S. Pugh, "How to get a PhD", Open University Press, ISBN 0-355-20550-X (2000).

[2] F. Halzen, A. Martin, "Quarks & Leptons: An Introductory Course in Modern Particle Physics", John Wiley & Sons, ISBN 0-471-88741-2 (1984) and references therein.

[3] The SNO Collaboration, "Direct Evidence for Neutrino Flavour Transformation From Neutral-Current Interactions in the Sudbury Neutrino Observatory", Phys. Rev. Lett. **89**, 011301 (2002).

[4] F. Mandl, G. Shaw, "Quantum Field Theory", John Wiley & Sons, ISBN 0-471-94186-7 (1984).

[5] I. Aitchison, A. Hey, "Gauge Theories in Particle Physics", Institute of Physics Publishing, ISBN 0-85274-328-9 (1989).

[6] S. Glashow,"Partial Symmetries of Weak Interactions", Nucl. Phys. **22**, 579 (1961).

[7] S. Weinberg, "A Model of Leptons", Phys. Rev. Lett. **19**, 1264 (1967).

[8] P. Higgs, "Broken Symmetries, Massless Particles and Gauge fields", Phys. Lett. **12**, 132 (1964).

[9] P. Higgs, "Broken Symmetries and the Masses of Gauge Bosons", Phys. Rev. Lett. **13**, 508 (1964).

[10] P. Higgs, "Spontaneous Symmetry Breakdown Without Massless Bosons", Phys. Rev. **145**, 1156 (1966).

[11] G. t'Hooft, "Renormalizable Lagrangians for Massive Yang-Mills Fields", Nucl. Phys. **B35**, 167 (1971).

[12] The ALEPH, DELPHI, L3 and OPAL Collaborations, "Search for the Standard Model Higgs Boson at LEP", Phys. Lett. B **565**, 61 (2003).

[13] K. Riesselmann, "Limitations of a Standard Model Higgs Boson", arXiv:hep-ph/9711456 (1997).

[14] The LEP Collaboration, "LEP EW WG Plots for the Winter 2006", http://lepewwg.web.cern.ch/LEPEWWG/plots/winter2006.

[15] M. Carena *et al.*, "Report of the Tevatron Higgs Working Group", arXiv:hep-ph/0010338 (2000).

[16] L. Babukhadia *et al.*, "Results of the Tevatron Higgs Sensitivity Study", Fermilab-Pub-03/320E (2003).

[17] The LEP and SLD Collaborations, "Precision Electroweak Measurements on The Z Resonance", CERN-PH-EP/2005-042 (2005).

[18] The DØ Collaboration, S. Abachi *et al.*, "The DØ Detector", Nucl. Instrum. Methods Phys. Res. A **338**, 185 (1994).

[19] The DØ Collaboration, S. Abachi *et al.*, "Search for High Mass top Quark Production in $p\overline{p}$ Collisions at $\sqrt{s} = 1.8$ TeV", Phys. Rev. Lett. **74**, 2422 (1995).

[20] Fermilab Beams Division, "Run II Handbook", http://www-bd.fnal.gov/runII/index.html.

[21] The DØ Collaboration, V. Abazov *et al.*, "The Upgraded DØ Detector", Fermilab-Pub-05/341E (2005), to appear in Nucl. Instrum. Methods Phys. Res. A (2006).

[22] The DØ Collaboration, S. Abachi *et al.*, "The DØ Upgrade: the Detector and its Physics", Fermilab-Pub-96/357E (1996).

[23] Fermilab Visual Media Services, "Photo Archive", http://www.fnal.gov/pub/presspass/vismedia/gallery/buildings.html.

[24] S. Nagaitsev *et al.*, "Experimental Demonstration of Relativistic Electron Cooling", Phys. Rev. Lett. **96**, 044801 (2006).

[25] Fermilab Beams Division, "Accelerator Division Notification", http://www-bd.fnal.gov/notifyservlet/www.

[26] Fermilab Beams Division, "Collider Run II Peak Luminosity", http://www-bdnew.fnal.gov/operations/lum/plum.gif.

[27] Fermilab Beams Division, "Collider Run II Integrated Luminosity", http://www-bdnew.fnal.gov/operations/lum/lum.html.

[28] P. Bhat, "Run II Luminosity Upgrades", talk presented at U.S. Department of Energy Review of Tevatron Operations meeting (29 March 2005), http://www.fnal.gov/directorate/DOE_TeVOps05_Review.html.

[29] Fermilab Beams Division, "Run II Luminosity Upgrade Plan, Version 4.0", http://www-ad.fnal.gov/run2upgrade.

[30] The DØ Collaboration, W. E. Cooper *et al.*, "DØ Silicon Trackers", Nucl. Instrum. Methods Phys. Res. A **549**, 1 (2005).

[31] M. H. Kirby, "SMT Longevity and HDI Failures", talk presented at DØ Collaboration meeting (28 September 2005), http://www-d0.hef.kun.nl/fullAgenda.php?ida=a051759.

[32] J. Warchol, "CFT Status", talk presented at DØ Collaboration meeting (28 September 2005), http://www-d0.hef.kun.nl/fullAgenda.php?ida=a051684.

[33] V. Abazov *et al.*, "The Muon System of the Run II DØ Detector", Nucl. Instrum. Methods Phys. Res. A **552**, 372 (2005).

[34] R. Schwienhorst, "The DØ Run II Trigger System", DØ Note 4638 (2004).

[35] The DØ Collaboration, "DØ Run II Integrated Luminosity", http://d0server1.fnal.gov/projects/operations/D0RunIIa_DataTaking_files/image006.png.

[36] The DØ Collaboration, "DØ Efficiency (Daily)", http://d0server1.fnal.gov/projects/operations/D0RunIIa_DataTaking_files/image005.png.

[37] T. Sjöstrand, "PYTHIA Manual", Comput. Phys. Commun. **82**, 74 (1994).

[38] Y. Fisyak *et al.*, "DØgstar: DØ GEANT Simulation of the Total Apparatus Response", DØ Note 3191 (1997).

[39] H. Melanson *et al.*, "The d0reco Package", http://www-d0.fnal.gov/d0dist/dist/packages/d0reco/p14-br-11.

[40] R. Brun *et al.*, "ROOT Users Guide", Version 3.1c (2001).

[41] G. Blazey *et al.*, "Run II jet Physics", arXiv:hep-ex/0005012 (2000).

[42] J. M. Butterworth *et al.*, "KtJet: A C++ Implementation of the $K_\perp$ Clustering Algorithm", arXiv:hep-ph/0210022 (2002).

[43] S. D. Ellis *et al.*, "Successive Combination jet Algorithm for Hadron Collisions", CERN-TH.6860/93 (2005).

[44] J.-L. Agram *et al.*, "Jet Energy Scale at DØ Run II", DØ Note 4720 (2005).

[45] DØ Jet Energy Scale Group, "Jetcorr Instructions", http://www-d0.fnal.gov/phys_id/jes/d0_private/certified/v5.3/jetcorr_v5.3.html.

[46] A. Schwartzman, "Jets With Tracking", talk presented at CDF/DØ Jet Workshop (2002), http://www-d0.fnal.gov/∼sch.

[47] D. Bloch *et al.*, "Jet Lifetime b-tagging", DØ Note 4069 (2002).

[48] P. Jonsson, "The Level 3 IP Tagger", http://www-d0.fnal.gov/d0dist/dist/packages/l3fbtag_ip.

[49] A. Jenkins *et al.*, "A $Z \to b\overline{b}$ Trigger Proposal for DØ", DØ Note 4644 (2004).

[50] A. Bellavance, "DØ Trigger Simulator Manual", http://www-d0.fnal.gov/computing/trigsim/general/docs/manual/index.html.

[51] V. Buescher *et al.*, "The trigger_rate_tool Package: a Tool to Estimate Rates and Overlaps for the Development of Physics Trigger Lists", DØ Note 4640 (2004).

[52] DØ Data Quality Coordination group, "Offline Run Quality Database Queries", http://d0db.fnal.gov/qualitygrabber/qualQueries.html.

[53] F. Villeneuve-Séguier & M. Petteni, "RASTA: a ROOT-files Analysis and STreaming Algorithm", http://www.hep.ph.ic.ac.uk/∼villeneu/analysis/rasta.html.

[54] A. Haas, "The higgs_multijet Package", http://www-d0.fnal.gov/d0dist/dist/packages/higgs_multijet.

[55] L. Feligioni *et al.*, "The Secondary Vertex b-Tagger User Guide", http://www-d0.fnal.gov/phys_id/bid/d0_private/certification/p14/secvertex/UserGuideSecVertexTagger.txt.

[56] J. Heinmiller *et al.*, "Jet Reconstruction Efficiency", DØ Note 4837, version 1.2 (2005), http://dzero.phy.uic.edu/james/higgs/index.html.

[57] L. Feligioni *et al.*, "Update on b-quark Jet Identification With Secondary Vertex Reconstruction Using DØreco Version p14", DØ Note 4414 (2004).

[58] T. Dorigo, "Observation of Z Decays to b Quark Pairs at the Tevatron Collider", arXiv:hep-ex/9806022 (1998).

[59] A. Haas *et al.*, "DØ Search For Neutral Higgs Bosons at High tanβ in Multi-jet Events Using p14 Data", DØ Note 4671 (2004).

[60] A. Jenkins & A. Goussiou, "An Investigation of b-jet Energy Resolution and $b\overline{b}$ Mass Resolution in $ZH \to e^+e^-b\overline{b}$ and $Z \to b\overline{b}$", DØ Note 4136 (2003).

[61] A. Jenkins *et al.*, "Evidence for $Z \to b\overline{b}$ Decays at DØ", DØ Note 4988 (2006).

[62] T. Scanlon & M. Anastasoaie, "Performance of the NN b-tagging Tool on Pass 2 p14 Data", DØ Note 4890 (2006).